NAVAL POSTGRADUATE SCHOOL
Monterey, California

THESIS

THE PHYSICAL CHARACTERISTICS OF BOTTOM SEDIMENT NEAR SUR RIDGE, CALIFORNIA

by

Christopher L. Gabriel

March 2001

Thesis Co-advisors: H. Gary Greene
Ching-Sang Chiu
Curtis A. Collins

Approved for public release; distribution is unlimited.

20010627 068

REPORT DOCUMENTATION PAGE	Form Approved OMB No. 0704-0188

Public reporting burden for this collection of information is estimated to average 1 hour per response, including the time for reviewing instruction, searching existing data sources, gathering and maintaining the data needed, and completing and reviewing the collection of information. Send comments regarding this burden estimate or any other aspect of this collection of information, including suggestions for reducing this burden, to Washington headquarters Services, Directorate for Information Operations and Reports, 1215 Jefferson Davis Highway, Suite 1204, Arlington, VA 22202-4302, and to the Office of Management and Budget, Paperwork Reduction Project (0704-0188) Washington DC 20503.

1. AGENCY USE ONLY *(Leave blank)*	2. REPORT DATE March 2001	3. REPORT TYPE AND DATES COVERED Master's Thesis

4. TITLE AND SUBTITLE: Title (Mix case letters) The Physical Characteristics of Bottom Sediment Near Sur Ridge, California	**5. FUNDING NUMBERS**
6. AUTHOR(S) Christopher L. Gabriel, Lieutenant, United States Navy	
7. PERFORMING ORGANIZATION NAME(S) AND ADDRESS(ES) Naval Postgraduate School Monterey, CA 93943-5000	**8. PERFORMING ORGANIZATION REPORT NUMBER**
9. SPONSORING / MONITORING AGENCY NAME(S) AND ADDRESS(ES) Naval Oceanographic Office 1002 Balch Boulevard Stennis Space Center, MS 39522	**10. SPONSORING / MONITORING AGENCY REPORT NUMBER**

11. SUPPLEMENTARY NOTES The views expressed in this thesis are those of the author and do not reflect the official policy or position of the Department of Defense or the U.S. Government.

12a. DISTRIBUTION / AVAILABILITY STATEMENT Approved for public release; distribution is unlimited.	**12b. DISTRIBUTION CODE** A

13. ABSTRACT ***(maximum 200 words)***

A study was conducted to determine the relationships between the geomorphology, sedimentology, and acoustic properties surrounding Sur Ridge, California, in an effort to determine their effects on acoustic tomography. Eleven gravity cores were taken in the vicinity of Sur Ridge. Detailed acoustic and sedimentologial analyses were conducted on the sediment within each core. The acoustic characteristics of the sediment and the geomorphology of Sur slope were examined to determine their impact on the arrival times and structures of acoustic tomography signals sent from a source on Davidson Seamount to a receiver on Sur Ridge. Based on analyses of cores collected for this study, it was found that sediment along the western slope of Sur Ridge are composed primarily of hemipelagic silty clays. Sediment within the trough to the east of Sur Ridge are fine sands composed primarily of relict glauconite grains that appear to be a lag deposit created by a relatively strong bottom current. The in-situ compressional wave velocities and wet bulk densities from the cores taken along the lower part of Sur slope were then assimilated into an existing acoustic model in an attempt to improve the accuracy of the model. Results indicated that due to the presence of a sound channel in the surficial sediment, the cores taken did not penetrate deep enough into the sediment in order to obtain an accurate profile of the compressional wave velocity gradient within the sediment.

14. SUBJECT TERMS Sur Ridge, sediment characteristics, acoustic tomography, glauconite.	**15. NUMBER OF PAGES** 192
	16. PRICE CODE

17. SECURITY CLASSIFICATION OF REPORT	18. SECURITY CLASSIFICATION OF THIS PAGE	19. SECURITY CLASSIFICATION OF ABSTRACT	20. LIMITATION OF ABSTRACT
Unclassified	Unclassified	Unclassified	UL

NSN 7540-01-280-5500

Standard Form 298 (Rev. 2-89)
Prescribed by ANSI Std. 239-18

THIS PAGE INTENTIONALLY LEFT BLANK

Approved for public release; distribution is unlimited.

THE PHYSICAL CHARACTERISTICS OF BOTTOM SEDIMENT NEAR SUR RIDGE, CALIFORNIA

Christopher L. Gabriel
Lieutenant, United States Navy
B.S., Washington State University, 1994

Submitted in partial fulfillment of the
requirements for the degree of

MASTER OF SCIENCE IN METEOROLOGY AND PHYSICAL OCEANOGRAPHY

from the

NAVAL POSTGRADUATE SCHOOL
March 2001

Author: _____
Christopher L. Gabriel

Approved by: _____
H. Gary Greene, Thesis Co-Advisor

_____
Ching-Sang Chiu, Thesis Co-Advisor

_____
Curtis A. Collins, Thesis Co-Advisor

_____
Roland W. Garwood, Chairman
Department of Oceanography

THIS PAGE INTENTIONALLY LEFT BLANK

ABSTRACT

A study was conducted to determine the relationships between the geomorphology, sedimentology, and acoustic properties surrounding Sur Ridge, California, in an effort to determine their effects on acoustic tomography. Eleven gravity cores were taken in the vicinity of Sur Ridge. Detailed acoustic and sedimentologial analyses were conducted on the sediment within each core. The acoustic characteristics of the sediment and the geomorphology of Sur slope were examined to determine their impact on the arrival times and structures of acoustic tomography signals sent from a source on Davidson Seamount to a receiver on Sur Ridge. Based on analyses of cores collected for this study, it was found that sediment along the western slope of Sur Ridge are composed primarily of hemipelagic silty clays. Sediment within the trough to the east of Sur Ridge are fine sands composed primarily of relict glauconite grains that appear to be a lag deposit created by a relatively strong bottom current. The in-situ compressional wave velocities and wet bulk densities from the cores taken along the lower part of Sur slope were then assimilated into an existing acoustic model in an attempt to improve the accuracy of the model. Results indicated that due to the presence of a sound channel in the surficial sediment, the cores taken did not penetrate deep enough into the sediment in order to obtain an accurate profile of the compressional wave velocity gradient within the sediment.

THIS PAGE INTENTIONALLY LEFT BLANK

TABLE OF CONTENTS

I. INTRODUCTION 1
- A. OBJECTIVES 1
- B. BACKGROUND 1
  - 1. Coastal Tectonics of Central California 4
  - 2. Geomorphologic description of Sur slope and Sur Ridge 4
  - 3. Geomorphological Analysis of Sur slope and Sur Ridge 8
  - 4. Coastal Oceanography Of Central California 10
- C. ACOUSTIC ENERGY AND BOTTOM INTERACTION 12
  - 1. The Interaction of Sediment with Acoustic Waves 12
  - 2. Sound Channels in Surficial Marine Sediments 14
  - 3. Previous work 15

II. METHODOLOGY 17
- A. CORE SAMPLING 17
- B. ACOUSTIC SEDIMENT ANALYSIS 19
  - 1. Compressional Wave Velocity 21
  - 2. Wet Bulk Density 22
  - 3. Magnetic Susceptibility 23
  - 4. Discussion 23
- C. PHYSICAL DESCRIPTION OF THE CORES 25
- D. GRAIN-SIZE ANALYSIS 25
  - 1. The Dry-Sieve Process 27
  - 2. The Pipette Process 28

III. RESULTS 31
- A. ACOUSTIC ANALYSIS DATA 31
  - 1. Correcting Laboratory Values to *In-situ* Values 31
  - 2. Review of the Acoustic Properties of Sediment 31
- B. SUMMARY OF ACOUSTIC PROPERTIES BY CORE 33
  - 1. Core A 33
  - 2. Core B 35
  - 3. Core C 35
  - 4. Core D 36
  - 5. Core E 38
  - 6. Core F 38
  - 7. Core G 40
  - 8. Core H 40
  - 9. Core I 41
- C. SUMMARY OF PHYSICAL PROPERTIES 42
  - 1. Cores A-E and Core H: The Fine-grained Cores 42
  - 2. Core G and Cores I-K: The Coarse-grained Cores 42
  - 3. Core F: The Transition Core 46
  - 4. Other Testing 46

5. Mineralogy 46
6. Paleontology 48
D. SUMMARY OF GRAIN-SIZE ANALYSIS 48
1. Core A 49
2. Core B 49
3. Core C 52
4. Core D 52
5. Core E 55
6. Core F 58
7. Core G 58
8. Core H 61
9. Core I 64
10. Core J 64
11. Core K 65

IV. DISCUSSION 67
A. RELATIONSHIP OF SEDIMENT AND GEOMORPHOLOGY 67
B. RELATIONSHIP OF SEDIMENT AND ACOUSTICS 73
C. RELATIONSHIP OF ACOUSTIC PROPERTIES OF SEDIMENT WITH RESPECT TO LOCATION 77
D. *IN-SITU* SEDIMENT VALUES IN THE MODELING OF ACOUSTIC TOMOGRAPHY SIGNALS 79

V. CONCLUSIONS 81
A. GEOMORPHOLOGY AND SEDIMENTATION REGIMES 81
B. SEDIMENTARY EFFECTS ON ACOUSTIC PROPERTIES 83
C. ACOUSTIC TOMOGRAPHY MODIFICATIONS 83

APPENDIX A –ACOUSTIC ANALYSIS DATA 85
CORE A 85
CORE B 89
CORE C 93
CORE D 97
CORE E 101
CORE F (TOP SECTION) 105
CORE F (BOTTOM SECTION) 108
CORE G 111
CORE H (TOP SECTION) 113
CORE H (BOTTOM SECTION) 116
CORE I 119

APPENDIX B – DETAILED ACOUSTIC DESCRIPTION OF CORES 121
CORE A 121
CORE B 123
CORE C 123
CORE D 124
CORE E 125
CORE F 128

CORE G 130
CORE H 130
CORE I 133
CORE J 134
CORE K 134

APPENDIX C – CONVERSION OF ACOUSTIC PARAMETERS OF SEDIMENT FROM LABORATORY VALUES TO *IN-SITU* VALUES 135
A. COMPRESSIONAL WAVE VELOCITY 135
B. WET BULK DENSITY 135

APPENDIX D – DETAILED PHYSICAL DESCRIPTION OF CORES 137
CORE A 137
CORE B 137
CORE C 140
CORE D 140
CORE E 144
CORE F 146
CORE G 146
CORE H 149
CORE I 151
CORE J 153
CORE K 153

APPENDIX E - SUBSAMPLING DATA FOR EACH CORE 155

APPENDIX F - DRY-SIEVE RESULTS BY WEIGHT (GRAMS) 157

APPENDIX G - PIPETTE RESULTS BY WEIGHT (GRAMS) 161

LIST OF REFERENCES 165

INITIAL DISTRIBUTION LIST 169

THIS PAGE INTENTIONALLY LEFT BLANK

LIST OF FIGURES

Figure 1.1. The coastline and bathymetry of central California, showing prominent offshore features. 2

Figure 1.2. Detailed bathymetry of the study area. Depth is in meters. 2

Figure 1.3. Tectonic map, showing relationships between the Salinan Block and Franciscan Complex, as well as the prominent fault zones affecting the study area. From Greene, 1977, and Clark, et al., 1994. 3

Figure 1.4. The regional geomorphology of central California, showing Sur Ridge in relation to Monterey Bay and Davidson Seamount. From Monterey Bay Aquarium Research Institute Multibeam Survey, 1998. 5

Figure 1.5. The detailed geomorphology of the study area, showing Sur slope, Sur Ridge, and other prominent features. The cross-section from A to A' is seen in Figure 1.6. From Monterey Bay Aquarium Research Institute Multibeam Survey, 1998. 7

Figure 1.6. Cross section along Sur Slope, looking north. Transect from point A to A' is shown on Figure 1.5. 8

Figure 1.7. Plan view of California Current System, showing the direction of the California Current (CC), California Undercurrent (CU), and Inshore Countercurrent (IC). 11

Figure 1.8. Plan view of Sur slope and Sur Ridge, showing placement and direction of the trough jet. Depth is in meters. 12

Figure 1.9. Plan view of acoustic energy path from Davidson Seamount to the listening array on Sur Ridge. From Onofre, 1999. 14

Figure 1.10. Cross-section view from Davidson Seamount to listening array on Sur Ridge, showing the interaction of eigenrays with bottom topography. DS = Davidson Seamount, SS = Sur slope. The white letters A-E indicate where Cores A-E were taken. From Onofre, 1999. 16

Figure 2.1. Plan view showing the locations of the gravity cores taken in relation to Sur Ridge. Bathymetry is in meters. 18

Figure 2.2. Plan view of the multi-sensor core sediment logging device. From Kayen, et al., 1999. 20

Figure 3.1. Graph showing the difference between the laboratory and *in-situ* mean values for compressional wave velocity and wet bulk density for Cores A-I. 32

Figure 3.2. *In-situ* compressional wave velocity, wet bulk density, magnetic susceptibility, glauconite percentage, and median grain size profiles for Cores A-C. Gaps at the top of the profiles are due to the endcaps. 34

Figure 3.3. *In-situ* compressional wave velocity, wet bulk density, magnetic susceptibility, glauconite percentage, and median grain size profiles for Cores D-F. Gaps at the top of the profiles are due to the endcaps. Due to the length of Core F, it was necessary to split it in half to fit in the acoustic analysis equipment and thus has missing data in the middle. 37

Figure 3.4. *In-situ* compressional wave velocity, wet bulk density, magnetic susceptibility, glauconite percentage, and median grain size profiles for Cores G-I. Gaps at the top of the profiles are due to the endcaps. Due to the length of Core H, it was necessary to split it in half to fit in the acoustic analysis equipment and thus has missing data in the middle. 39
Figure 3.5. Picture of Core B, 0-60 cm, as an example of a fine-grained sediment core.. 43
Figure 3.6. Picture of Core I, 0-45 cm, as an example of a coarse-grained sediment core. 44
Figure 3.7. Picture of Core F, 0-33 cm, showing the transitional nature of the sediment. Note localized concentrations of glauconite. 45
Figure 3.8. Graph showing Carbon-14 data for Cores A, B, and G, as well as linear interpolation of approximate sedimentation rates. 47
Figure 3.9. Grain size distribution, cumulative percentage curves, median grain size profile, and glauconite percentage profile for Core A, collected at 2553 m... 50
Figure 3.10. Grain size distribution, cumulative percentage curves, median grain size profile, and glauconite percentage profile for Core B, collected at 2285 m. 51
Figure 3.11. Grain size distribution, cumulative percentage curves, median grain size profile, and glauconite percentage profile for Core C, collected at a depth of 1948 m. 53
Figure 3.12. Grain size distribution, cumulative percentage curves, median grain size profile, and glauconite percentage profile for Core D, collected at a depth of 1672 m. 54
Figure 3.13. Grain size distribution, cumulative percentage curves, median grain size profile, and glauconite percentage profile for Core E, collected at a depth of 1435 m. 56
Figure 3.14. Grain size distribution, cumulative percentage curves, median grain size profile, and glauconite percentage profile for Core F, collected at a depth of 1232 m. 57
Figure 3.15. Grain size distribution, cumulative percentage curves, median grain size profile, and glauconite percentage profile for Core G, collected at a depth of 1341 m. 59
Figure 3.16. Grain size distribution, cumulative percentage curves, median grain size profile, and glauconite percentage profile for Core H, collected at a depth of 851.3 m. 60
Figure 3.17. Grain size distribution, cumulative percentage curves, median grain size profile, and glauconite percentage profile for Core I, collected at a depth of 1128 m. 62
Figure 3.18. Grain size distribution, cumulative percentage curves, median grain size profile, and glauconite percentage profile for Core J, collected at a depth of 1157 m. 63
Figure 3.19. Grain size distribution, cumulative percentage curves, median grain size profile, and glauconite percentage profile for Core K, collected at a depth of 855 m. 66
Figure 4.1. Composite grain-size distribution graphs for Cores A-C (2553-1948 m), D-F (1672-1232 m) and H (851.3 m), and G (1341 m) and I-K (1128 m, 1157 m, and 855 m, respectively). 67

Figure 4.2. Graph showing the percentage of sediment composed of glauconite per core. 69
Figure 4.3. Composite profiles of compressional wave velocity, wet bulk density, magnetic susceptibility, glauconite percentage, and median grain size for Cores A-C, D-F and H, and G-I. 75
Figure 4.4. Mean values of compressional wave velocity, wet bulk density, porosity, and glauconite percentages for cores A-I. 78
Figure B.1. Laboratory profiles of compressional wave velocity, wet bulk density, and magnetic susceptibility for Cores A-C. 122
Figure B.2. Laboratory profiles of compressional wave velocity, wet bulk density, and magnetic susceptibility for Cores D-F. 126
Figure B.3. Laboratory profiles of compressional wave velocity, wet bulk density, and magnetic susceptibility for Cores G-I. 131
Figure D.1. Core A, 0-60 cm. 138
Figure D.2. Core A, 60-116 cm. 138
Figure D.3. Core B, 0-60 cm. 138
Figure D.4. Core B, 60-120 cm. 139
Figure D.5. Core B, 110-141 cm. 139
Figure D.6. Core C, 0-60 cm. 139
Figure D.7. Core C, 60-120 cm. 141
Figure D.8. Core C, 110-148 cm. 141
Figure D.9. Core D, 0-60 cm. 141
Figure D.10. Core D, 60-120 cm. 142
Figure D.11. Core D, 110-128 cm. 142
Figure D.12. Core E, 0-37 cm. 142
Figure D.13. Core E, 35-73 cm. 143
Figure D.14. Core E, 62-100 cm. 143
Figure D.15. Core E, 100-138 cm. 143
Figure D.16. Core F, 0-33 cm. 145
Figure D.17. Core F, 40-76 cm. 145
Figure D.18. Core F, 58-86 cm. 145
Figure D.19. Core F, 86-146 cm. 147
Figure D.20. Core F, 145-184 cm. 147
Figure D.21. Core G, 0-46 cm. 147
Figure D.22. Core G, 10-36 cm, showing sediment texture primarily composed of heavy concentrations of glauconite sands and foraminifera. 148
Figure D.23. Core G, 14-31 cm, showing sediment texture primarily composed of heavy concentrations of glauconite sands and foraminifera. 148
Figure D.24. Core H, 0-61 cm. 150
Figure D.25. Core H, 45-81 cm. 150
Figure D.26. Core H, 81-140 cm. 150
Figure D.27. Core H, 128-160 cm. 152
Figure D.28. Core I, 0-45 cm. 152
Figure D.29. Core J, 0-30 cm. 152

LIST OF TABLES

Table 2.1. Table showing the location, depth, and overall length of each core, as well as the date taken and vessel used for sampling. NH = R/V New Horizon, PS = R/V Point Sur. 18

Table 2.2. Conversion of phi scale to millimeters, U.S. Standard sieve mesh, and Wentworth Size Class. Modified from Boggs, S. Jr., 1987. 26

Table 2.3. Calculated times and depths for pipette analysis. From Folk, 1980. 29

Table 3.1. Table showing Carbon-14 samples, ages, and error. 47

ACKNOWLEDGMENTS

As are most other theses, this work is more of a collaboration than anything else; while it was I that put the words on paper, many other people played significant roles in this study. While it is important to me to recognize them for their assistance and advice, it would be impossible to to thank them fully for all they have done for me.

Firstly, I would like to thank Professor Curt Collins for accepting me as his thesis student, and for indulging my desires when choosing a thesis topic. His assistance and support have made this entire project possible. Tarry Rago also provided support and advice, and answered many questions of mine, and I thank him for his support as well.

I want to thank Professor Gary Greene for taking time out of his unbelievably busy schedule to guide me and provide insight into my study. His comprehensive knowledge of all things geologic involving the central California Coast helped focus me on my tasks. Patrick Mitts provided invaluable assistance to me every step of the way during the grain-size analysis section of my thesis. I thank him for his time and friendship, and for keeping me fed with excellent food during some very late nights in Moss Landing.

Professor Ching-Sang Chiu also took time out of his very busy schedule to help me with some of the finer acoustic aspects in this study. Chris Miller also helped with the acoustics section and provided me with bathymetric data for many of my diagrams. I also want to thank Professor Bob Bourke for talking with me about my project, and for providing me with an extensive file of papers dealing with acoustic properties of sediment.

I want to thank Steve Bliss and the mighty crew of the R/V Point Sur for their excellence at putting the gravity core right where I wanted it. Special thanks go to Rich Muller (Moss Landing Marine Labs), for spending his time to help me bring my cores up from the bottom of the ocean. Likewise, thanks go to Dave Murline and the intrepid crew of the R/V New Horizon, who were also adept at putting the gravity core where I wanted it. Special thanks go to Steve Rusk for his late-night work in getting my cores to the surface.

I want to thank Homa Lee (USGS, Menlo Park), for making the time for me to use their acoustic analysis equipment. I also want to thank Brad Carkin for his skilled assistance in analyzing the cores for me, and for making sure the data I received was as accurate as possible.

I want to thank Mary Jordan and Mike Cook for their timely assistance with all things MATLAB, and also Reggie Durazo for helping me construct my poster. Likewise, I want to thank John Dumas for helping me gain a deeper understanding and appreciation for MATLAB code. The camraderie of my classmates has certainly helped buoy me through the process of writing this thesis. I will miss them.

Finally, I want to thank the people most important to me in this endeavor. There are some people that have been companions to me over the years, and I want to thank them: DMcC, DJJ, JH, HM, JES, WES, PIT, SVR, GF, JM, OH, RWS, and above all else, TGM. I want to thank my mentor, guide, and good friend Larry Davis for his long-distance support and understanding, and for his friendship. Without his encouragement I am not sure if I would even be at the Naval Postgraduate School. Likewise, I want to thank my parents for their continual support, encouragement, and interest. Most

importantly, I want to thank my wife Kim for putting up with me, answering a myriad of questions regarding Word and Excel, and for listening to me and helping me through my confusion. It is because of her love and devotion that I dedicate this work to her.

Cut loose from the shores of confidence and complacency
Adrift in an sea of acoustic confusion
in a fragile liferaft of consciousness
that is folded and faulted by past experience
Uncertainty drifts down as a fine sediment
forming a layer of questions over everything I see
To drink of the ocean would create only a greater thirst
much as the thirst for truth and wisdom only creates a greater thirst for the same.
The winds, ever flowing across the waters
bring me answers I thought I sought;
yet the wind stirs the waters to greater waves of doubt.
My very soul, an ocean of delicate concepts, ideals, impressions
Is constantly threatened by the geostrophic balance of life.
Struggling to keep my head above the water
pulled down by the unrelenting force of acadamia
reaching to grasp for truths and ideas
that lay just beyond my horizons
How many times must I reach for them, before they are mine?
How long do I struggle in the surf, before I stop
And with a smile, slowly sink below the surface
spiraling deeper, until, touching bottom, I smile once again
knowing
that I am where I belong;
knowing
I have come home.

THIS PAGE INTENTIONALLY LEFT BLANK

I. INTRODUCTION

A. OBJECTIVES

The purpose of this study is to examine the relationships between the geomorphology, sedimentology, and acoustic properties surrounding Sur Ridge, California (Figure 1.1). The preliminary goal for this investigation was to obtain gravity cores of sufficient length to determine Holocene stratigraphy in the vicinity of Sur Ridge and Sur slope, and to compare the acoustic properties and sedimentology of the sediment within each core (Figure 1.2). These analyses were then related to the structural geology, sedimentology, geomorphology, and oceanographic conditions surrounding Sur Ridge. Finally, the *in-situ* acoustic characteristics of the sediment from this study were implemented into an acoustic model to determine the alteration of the arrival times of acoustic tomography signals transmitted from Davidson Seamount and recorded at Sur Ridge.

B. BACKGROUND

Extensive amounts of information exist for the geology, tectonics, and sedimentology of central California's margin, particularly in the Monterey Bay region. However, the margin near Point Sur, California, has received less attention, and thus warrants additional investigation. Analysis of offshore structure, geology, and sediment characteristics can lead to a more comprehensive geologic and tectonic picture of Central California as a whole. In addition, the interaction of offshore geologic features such as ridges and mounds with the bottom or near-bottom currents play a major role in sediment distribution and transport.

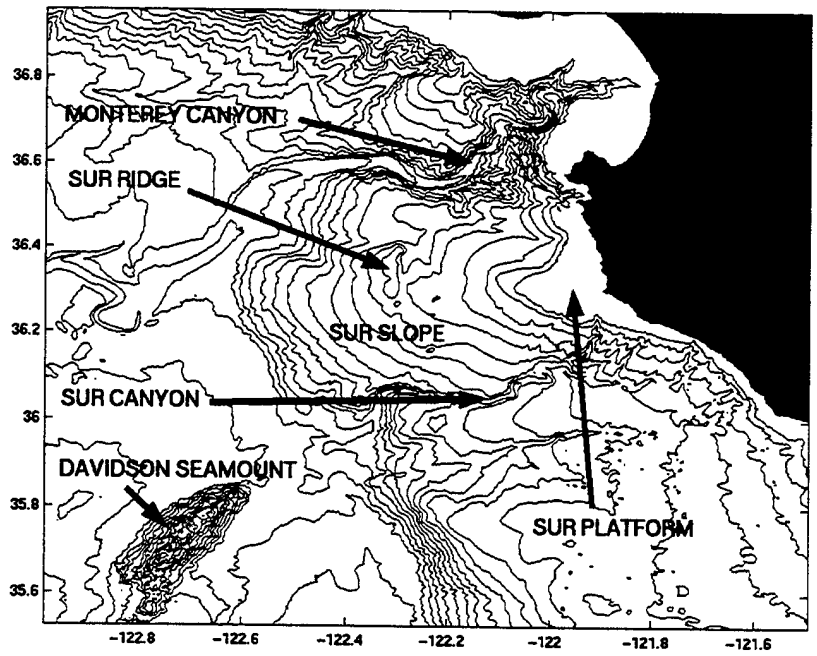

Figure 1.1. The coastline and bathymetry of central California, showing prominent offshore features.

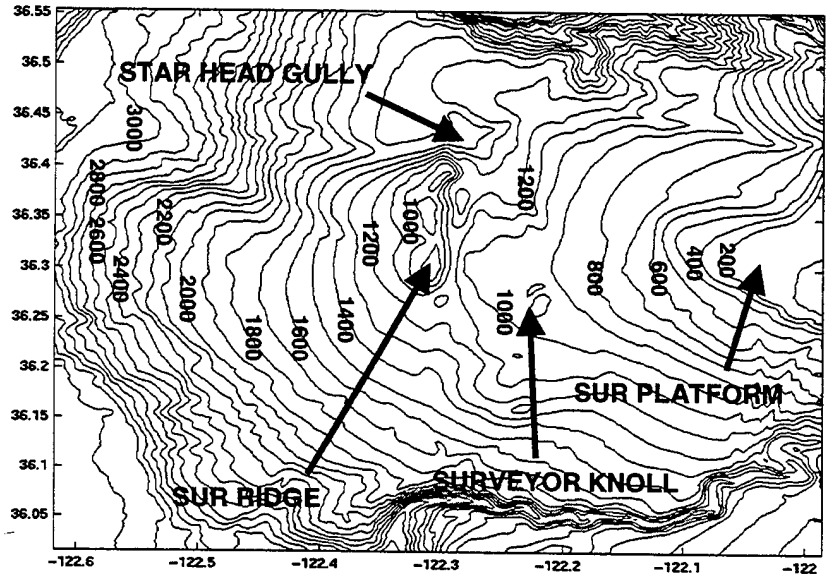

Figure 1.2. Detailed bathymetry of the study area. Depth is in meters.

Likewise, a greater understanding of acoustic interaction with bottom sediments can help to further refine existing acoustic models that include bottom attenuation. Acoustic energy transmitted from Davidson Seamount interacts with the sediment along Sur slope and Sur Ridge. Thus a detailed description of the acoustic properties of the sediment in this study area would result in improved accuracy for acoustic ray models.

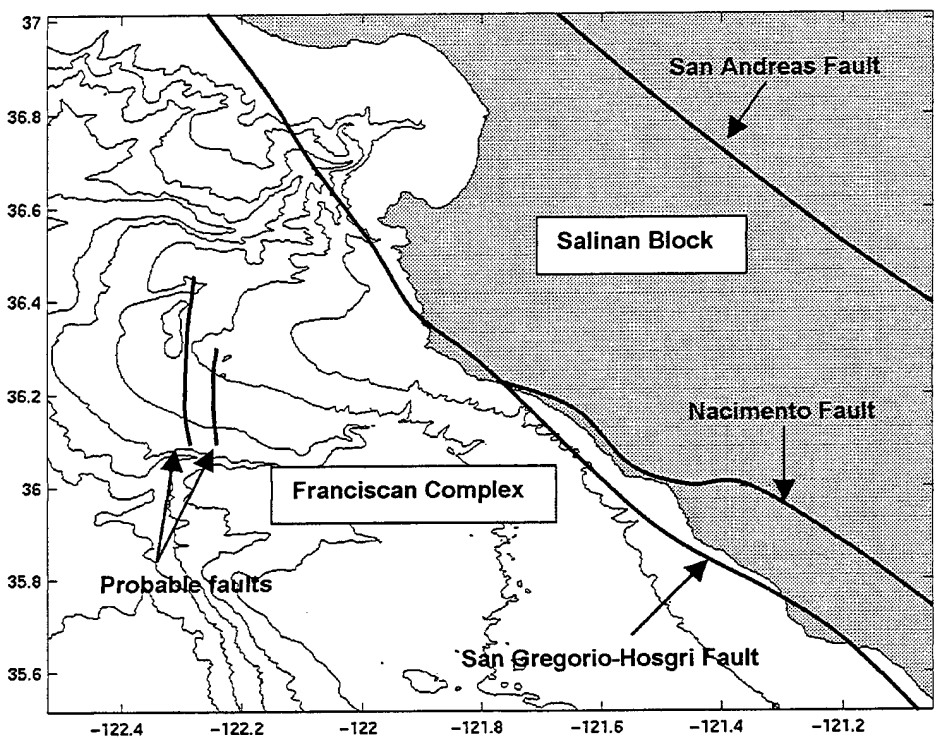

Figure 1.3. Tectonic map, showing relationships between the Salinan Block and Franciscan Complex, as well as the prominent fault zones affecting the study area. From Greene, 1977, and Clark, et al., 1994.

1. Coastal Tectonics of Central California

The topography and geology of the central California margin results from the transpressive plate motion between the Pacific Plate and the North American Plate

(Atwater, 1970). This tectonic activity has given rise to the San Andreas transform fault system (Atwater, 1970). In the vicinity of Sur Ridge, the area is dominated by the Palo Colorado-San Gregorio fault zone, which is a northwest-southeast striking right-lateral fault zone (Figure 1.3) (Greene, 1977). The right-lateral movement along this fault has introduced a sliver of granitic basement rocks, known as the Salinan Block, into an area dominated by the San Simeon Block, which is composed of Franciscan Complex rocks (Figure 1.3) (Greene, 1977, 1990; Clark, et al., 1994). The Franciscan Complex rocks are the basement rocks under Sur slope and Sur Platform, and are composed primarily of graywacke and other metasedimentary and metavolcanic rocks, as well as serpentinites. Thus the Palo Colorado-San Gregorio fault zone represents the boundary between the San Simeon Block and Salinan Block (Figure 1.3) (Greene, 1977, 1990; Clark, et al., 1994). Immediately onshore and east of the Sur slope area are the southern Santa Lucia Mountains, which are part of the Salinan Block and result from uplift during the late Neogene to Quaternary time.

2. Geomorphologic description of Sur slope and Sur Ridge

The Sur Platform, part of the continental shelf, projects seaward approximately 30 km from Point Sur, California (Figure 1.4). Sur Slope extends from the shelf break (~100 m depth) and radiates to the west in a broad, cone shape before intersecting the abyssal plain at a depth of approximately 3300 m (Greene, et al., 1989). Sur Ridge is located approximately 28 km west of the shelf break, approximately halfway down Sur slope towards the abyssal plain. Figure 1.5 shows the detailed geomorphology of Sur slope and

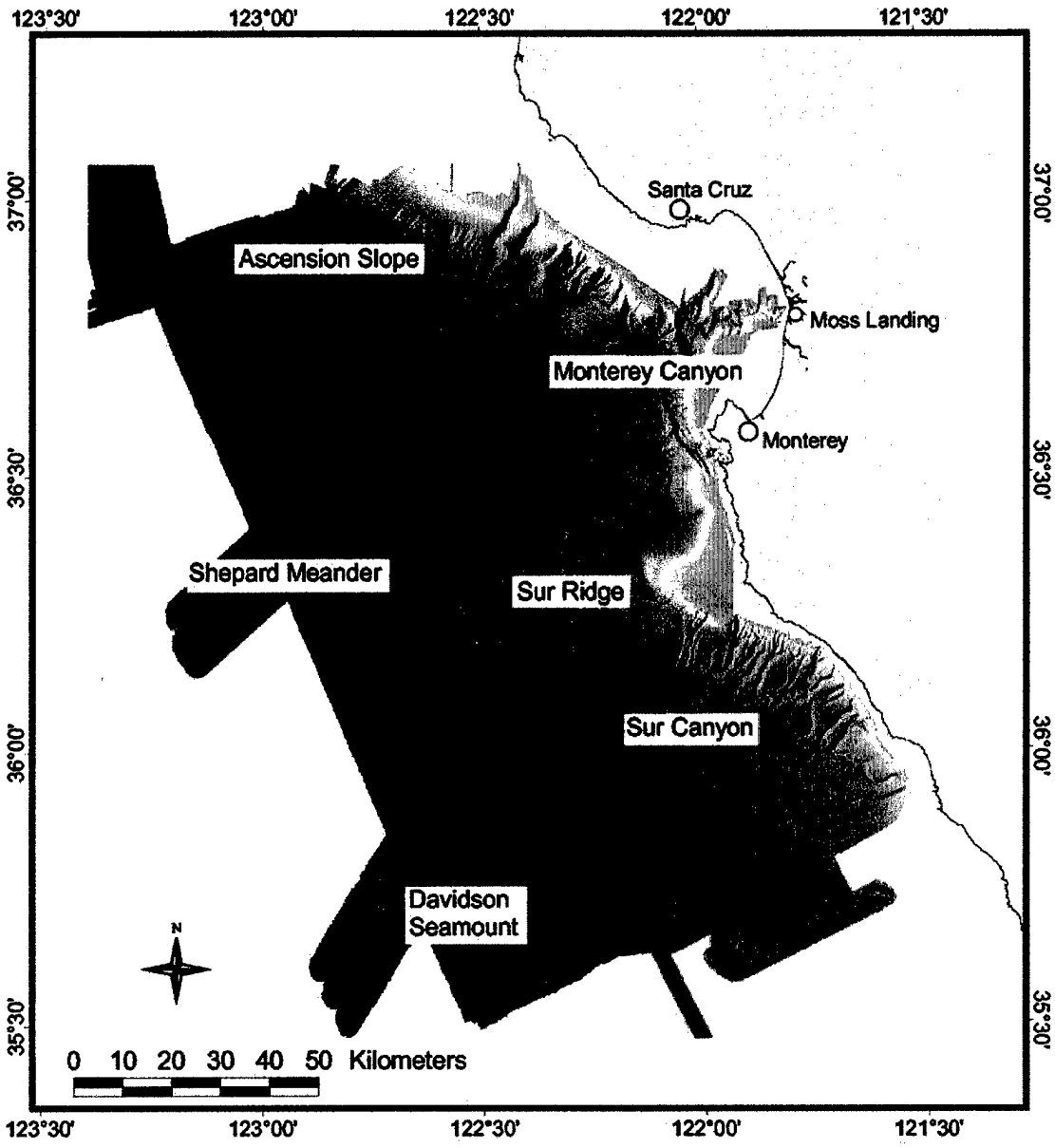

Figure 1.4. The regional geomorphology of central California, showing Sur Ridge in relation to Monterey Bay and Davidson Seamount. From Monterey Bay Aquarium Research Institute Multibeam Survey, 1998.

Sur Ridge. The slope is bounded on the south by Sur Canyon, on the north by Monterey Canyon, on the west by the continental rise or abyssal plain, and on the east by the continental shelf break (Figure 1.5). The upper northern and western sections of the slope are relatively smooth and unaltered by erosion, compared to the southern part of the upper slope, which shows numerous erosional notches (Greene, in press). Additionally, the upper half of the cone is relatively smooth and undisturbed, while the lower half shows numerous landslides. The prominent feature of Sur slope is Sur Ridge. Sur Ridge is 18 km long and extends from N36°16', W122°18' to N36°25', W122°18', trending almost exactly north-south. The ridge consists of three peaks, the southern peak being the highest and standing 280 m above the surrounding continental slope, at a depth of approximately 840 m below the ocean surface. The ridge has an average width of 4.8 km and is asymmetrical in shape in the east-west direction (Figure 1.6). The western slope of the ridge has a gradient of 4°, blending in with the continental slope, whereas the eastern slope has a much higher gradient of 9.9° to 10.8°, ending in a trough that runs parallel to the ridge, between the ridge and the continental slope.

While the tectonic deformation is largely responsible for forming the sea floor geomorphology, sediment deposition also is effective in shaping the bottom. The continental shelf and slope of central California derive sediment from two main sources. The first source is hemipelagic sediment, which is composed of 25% or more ferruginous, volcanic, or neritic sediment, and 75% or less of pelagic sediment. Typically this type of sediment is composed of the finer material not deposited in nearshore environments.

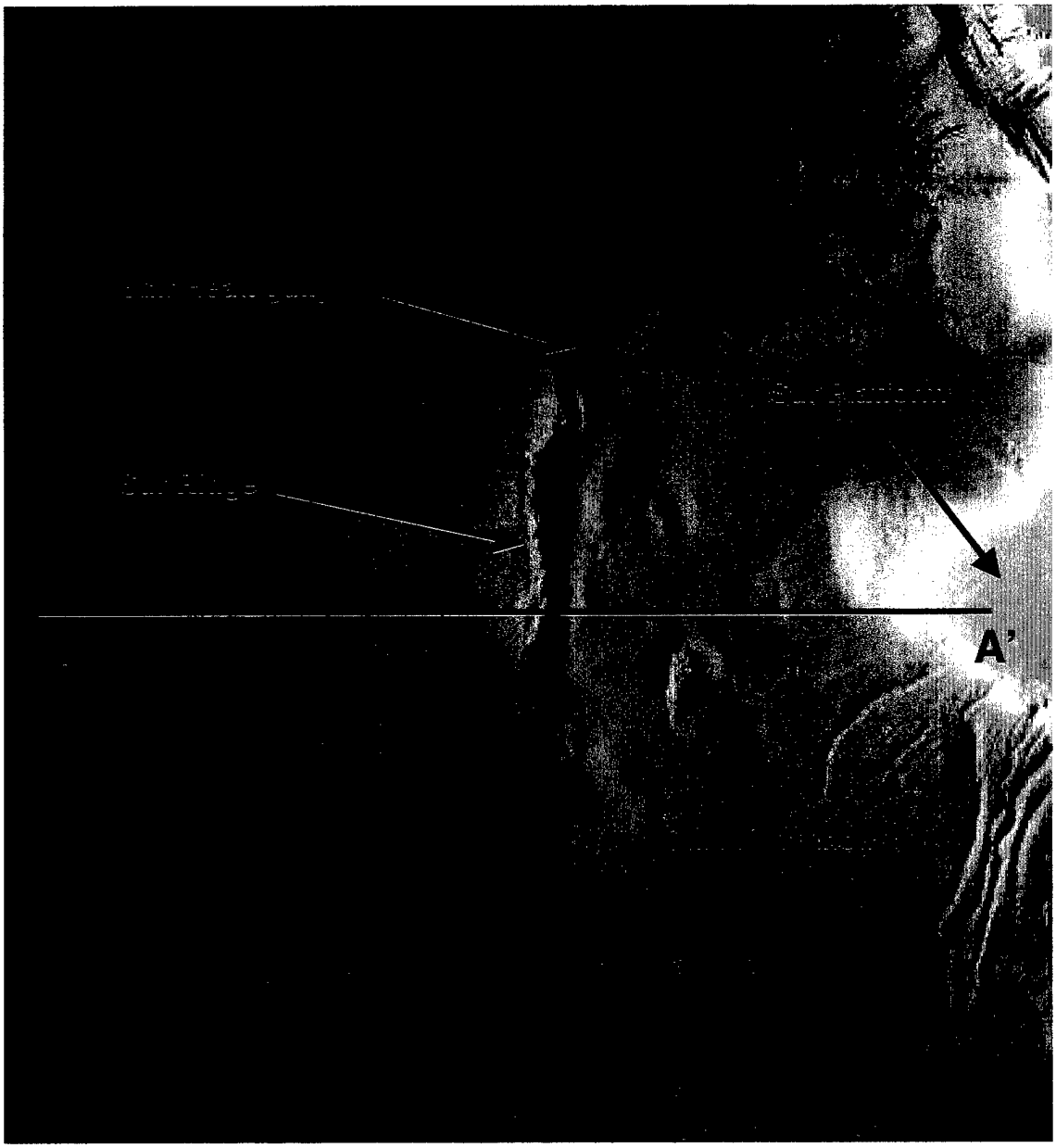

Figure 1.5. The detailed geomorphology of the study area, showing Sur slope, Sur Ridge, and other prominent features. The cross-section from A to A' is seen in Figure 1.6. From Monterey Bay Aquarium Research Institute Multibeam Survey, 1998.

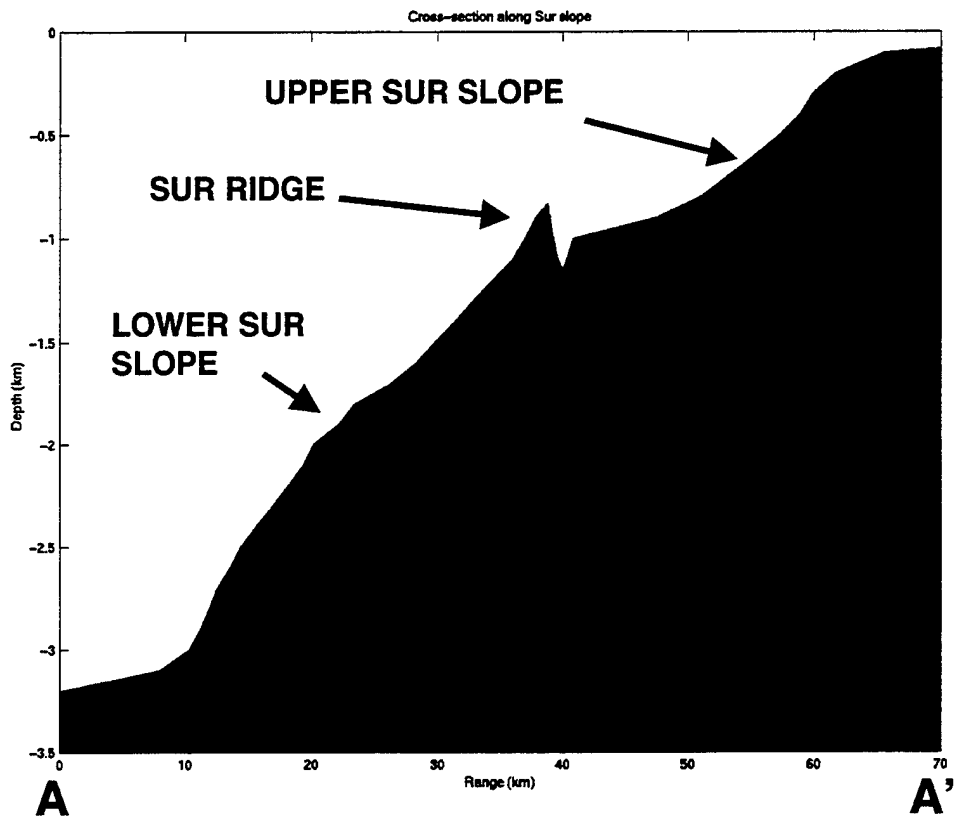

Figure 1.6. Cross section along Sur Slope, looking north. Transect from point A to A' is shown on Figure 1.5.

Once this suspended sediment enters a relatively calm depositional environment like a continental shelf or slope, it settles out of the water column. Authigenic sedimentation is the second source. Authigenic sediment forms in place; there is no transportation involved with the deposition. Typically authigenic sediment is a chemical precipitate, such as glauconite, a mineral sediment that plays a significant role in this study.

3. Geomorphological Analysis of Sur slope and Sur Ridge

The geomorphological features of Sur slope, Sur Ridge, and Sur Platform have recently been described in detail (Greene, et al, in press). It was determined that two

major forces shaped the geomorphology: tectonics and mass wasting. A brief summary of the findings will be included here to help with the understanding of the acoustic and sedimentological analyses in Chapter III and discussions in Chapter IV. In addition, it is important to remember that the seafloor along the margin of central California changes constantly by the alteration of seafloor elevations, initiation of mass wasting events, and alteration of sedimentary processes. The geologic history of the Point Sur area, and how continuous change affects the margin, plays a vital role in the understanding of the sediment types and compositions found in this study.

As previously discussed, Sur slope and its associated features are impacted by the tectonics occurring along the coast of central California. In the case of Sur slope, these features are manifested as two linear ridges that generally trend north to south. The primary feature, containing Sur Ridge, extends for over 50 km across the lower part of Sur slope (Greene, et al, in press), and represents uplift along a probable fault, forming a horst or half-horst (Figures 1.3, 1.5). The second feature, Surveyor Knoll, was also produced by uplift along a probable fault that trends NE-SW extending south to Sur Canyon, and forms the western face of Surveyor Knoll (Figures 1.3, 1.5).

Numerous indications of mass wasting can be seen on and around Sur slope (Figure 1.5). For example, Star Head gully shows slumping in each of its arms, and older slides extend southward up Sur slope from the head of the southeastern trending arm (Greene, et al, in press). The lower western half of Sur slope itself also shows numerous prominent landslide scars, most notably Sur Slide (Figure 1.5). These mass wasting events show a broad range of geomorphic ages. Younger slumps show well-defined slump heads, whereas older slumps appear to have "healed" over time, with their

morphological definition becoming less visible as sedimentary processes (erosion or deposition of sediment) rounded their edges. In several locations, retrogressive erosion has occurred where slumps along the lower part of Sur slope have reduced the stability of the sediment on the upper part, causing that sediment to slump in turn. In other places, landslides appear to have occurred higher up on the slope; the resultant debris flowed straight down to the base of the slope. Once this occurs, upslope propagation of mass wasting begins at the head of the newly formed landslide.

4. Coastal Oceanography Of Central California

The coastal waters along central California are dominated by the California Current System (CCS), which consists of two flow regimes. The first runs closely along the coastline, where two poleward flowing currents are found. These currents are the Inshore Countercurrent (IC), or Davidson Current, and the California Undercurrent (CU) (Figure 1.7) (Collins, et al., 2000). Seaward of these two currents is the second flow regime, the California Current (CC), which flows equatorward (Figure 1.7). The CU transports warm, saline equatorial waters, with the maximum transport at a depth of 350 m below the surface, at an average magnitude of 7.6 cm/s, and flows along the continental slope (Collins, et al., 2000). The CU can be seen year round. The IC is more of a seasonal flow, appearing in fall and winter. The IC is found both over the continental shelf and slope, and transports shallow, upper ocean waters, which are derived from CC waters that have been modified by coastal processes.

A recent study analyzing the mean structure of the undercurrent off Point Sur (Collins, et al., 2000) revealed a complicated structure of the flow in the trough along the

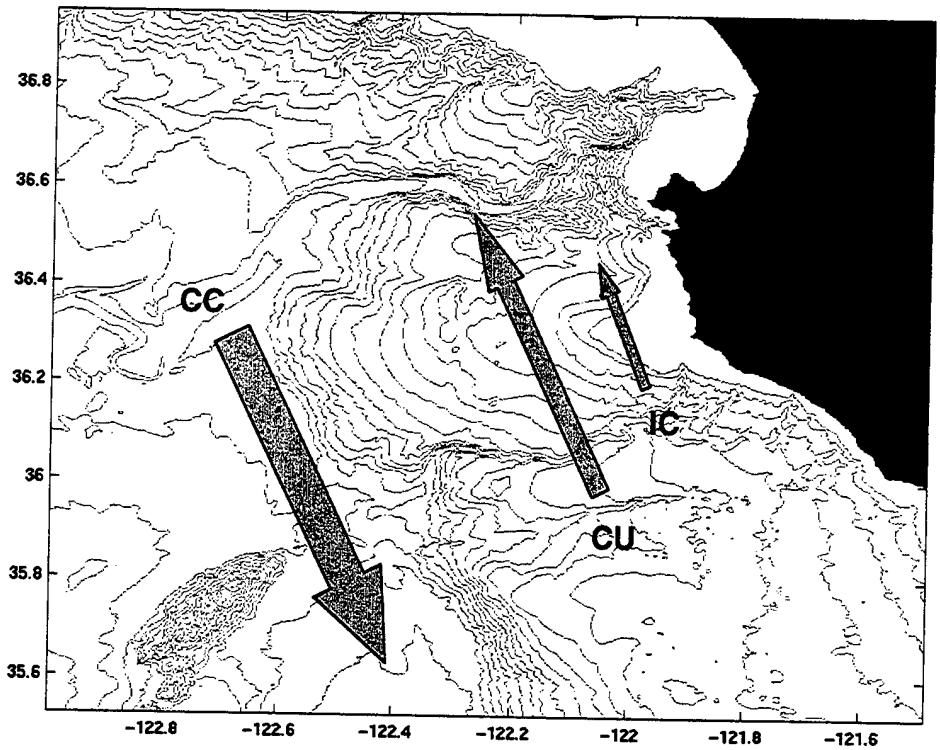

Figure 1.7. Plan view of California Current System, showing the direction of the California Current (CC), California Undercurrent (CU), and Inshore Countercurrent (IC).

eastern side of Sur Ridge. At the level of the top of the ridge, the poleward flow reverses and becomes equatorward, with a mean velocity of 2 cm/s. Approximately 50 m above the bottom, the flow reverses again to poleward, and intensifies to 8 cm/s at the bottom (Figure 1.8) (Collins, et al., 2000). This intensification, or "trough jet", is a unique feature. The jet is strong enough to affect sediment transport and create a different depositional environment than that found elsewhere along Sur slope. The trough jet shows much more vertical shearing than the poleward flow immediately to the west of Sur Ridge (Figure 1.5) (Collins, et al., 2000).

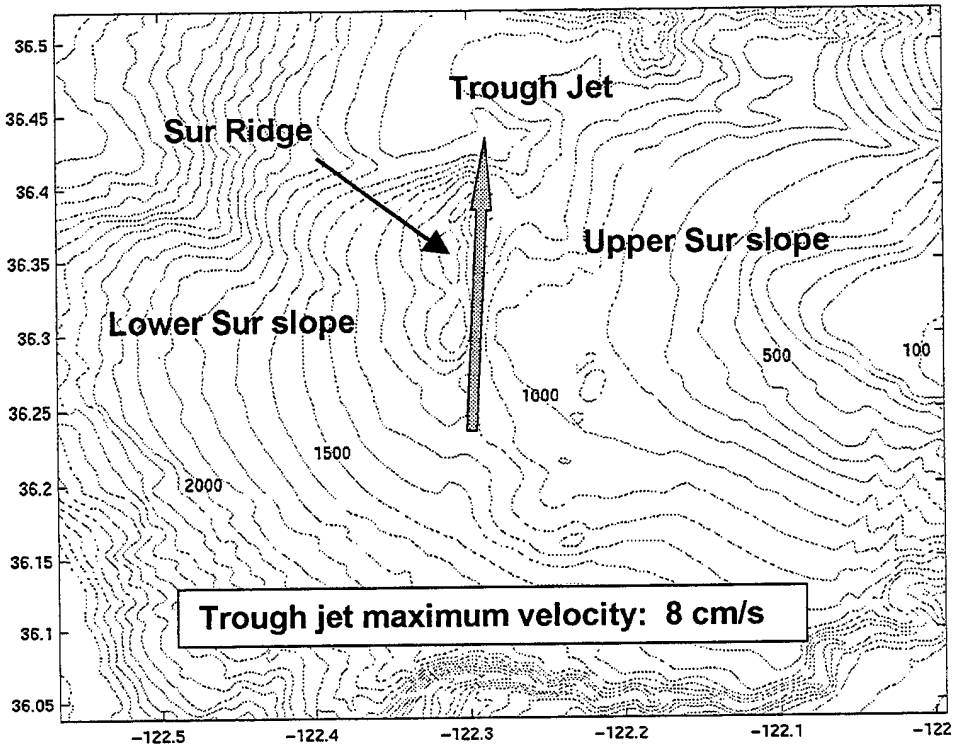

Figure 1.8. Plan view of Sur slope and Sur Ridge, showing placement and direction of the trough jet. Depth is in meters.

C. ACOUSTIC ENERGY AND BOTTOM INTERACTION

Hamilton (1970a-c, 1971, 1972, 1974, 1976, 1978), among others, has conducted extensive research regarding acoustic properties of sediment, and the interaction of acoustic energy with ocean bottoms. A brief discussion regarding this interaction will help to clarify and explain the acoustic tomography aspects of this study.

1. The Interaction of Sediment with Acoustic Waves

Hamilton (1970b, 1972) provides an in-depth discussion on the interaction of acoustic waves with bottom sediment. Acoustic waves are compressional waves; when

these waves propagate in relatively shallow regions that have varied topography, such as the area of this study, the waves impinge on the surface of the sediment. When this compressional energy propagates into the sediment, it experiences frictional effects that will attenuate the energy of the wave, as well as change the phase of the wave. The energy will continue to propagate as a compressional wave, but will also create a shear wave due to the rigidity of the sediment. Depending on the difference of the compressional wave velocities of the water and sediment at the water-sediment interface, the wave will be refracted or reflected. If the sediment compressional wave velocity is faster than the water compressional wave velocity, the wave will be reflected. If the sediment compressional wave velocity is slower than the water compressional wave velocity, the wave will be refracted deeper into the sediment. The focus of this study is the reflection of the waves from the bottom, and how the magnitude and phase of the wave changes due to the attenuation experienced from the interaction with the sediment.

As compressional waves propagate into fine-grained sediment (clays and silts), the pore water within the sediment compresses and then expands. When this happens, it causes the particles of sediment to move as well. The movement of the sediment particles creates inter-grain friction between the particles of sediment. This inter-grain friction is the main source of attenuation in fine-grained sediments (Hamilton, 1972). Attenuation of the wave within the sediment results in a weaker wave propagating out of

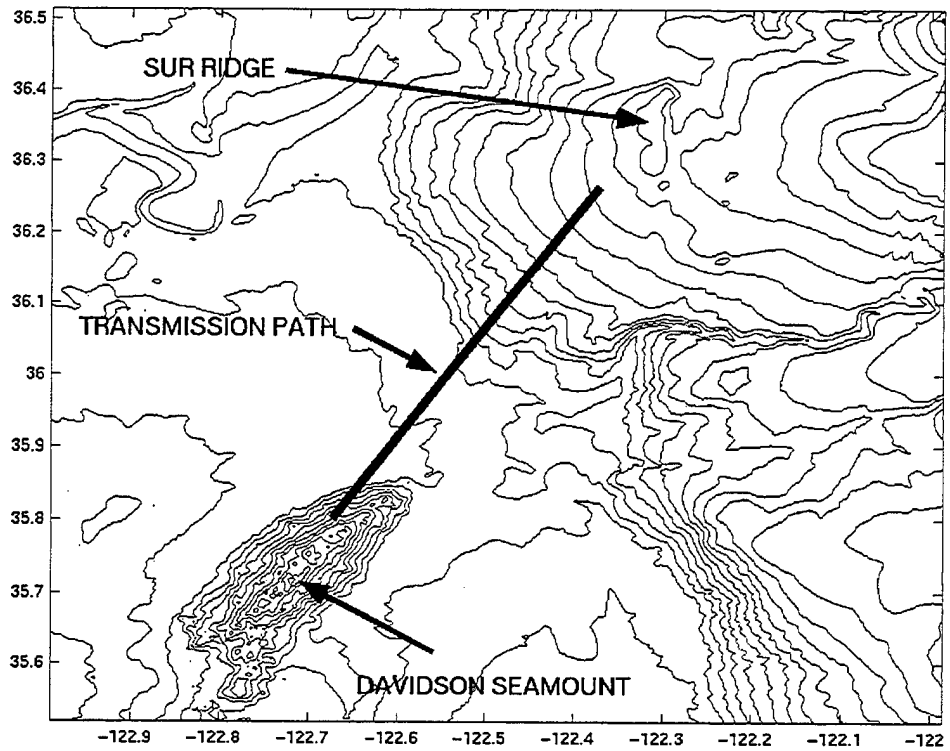

Figure 1.9. Plan view of acoustic energy path from Davidson Seamount to the listening array on Sur Ridge. From Onofre, 1999.

the sediment once the wave is reflected. In addition, Hamilton (1972) has also demonstrated that coarser grained sediments (i.e. fine sands) will attenuate acoustic energy at a much greater rate than finer grained sediments.

2. Sound Channels in Surficial Marine Sediments

When the compressional wave velocity of the sediment is slower than the compressional wave velocity of the bottom waters, the acoustic wave will be refracted deeper into the sediment. Hamilton (1970b) describes this process as the formation of a surficial sound channel in the upper 5-95 m of sediment. This type of sound channel

most commonly occurs in fine-grained sediment, due to the high level of inter-grain friction. Deeper in the sediment, the wet bulk density of the sediment will increase due to loss of pore water. This will decrease the compressional wave velocity. However, once the consolidation of the sediment begins to increase (due to overlying pressure), the increase in density will begin to increase the compressional wave velocity. This leads to the formation of a positive sound speed gradient within the sediment and will cause the acoustic energy to be reflected back into the ocean.

3. Previous work

Onofre (1999) studied the propagation of acoustic energy from Davidson Seamount to the Sound Surveillance System (SOSUS) array on Sur Ridge (Figure 1.9). The array is located on the upper southwestern flank of Sur slope, approximately 6 km to the west of the southern most peak of Sur Ridge. It is at an approximate depth of 1380 m. The majority of acoustic rays transmitted from Davidson Seamount interact with the bottom sediment along the slope of Sur slope (Figure 1.10). In particular, rays interact with two distinct regions of local morphology: the smooth, unbroken middle part of Sur slope, and the uneven, hummocky lower part of Sur slope. The sediment cores obtained for this study were taken from the regions where the acoustic rays interact (Figure 1.10). To complete his study, Onofre (1999) used accepted standards for compressional-wave velocity (1600 m/s) and wet bulk density (1650 kg/m^3) of sediment to model the arrival times and acoustic structures of the acoustic arrays. The actual *in-situ* compressional wave velocity and density of the sediment from the cores collected for this study should provide a more accurate input into the model, and could possibly provide some discernable relationships between the sediment types, geomorphology, and arrival times of the acoustic rays.

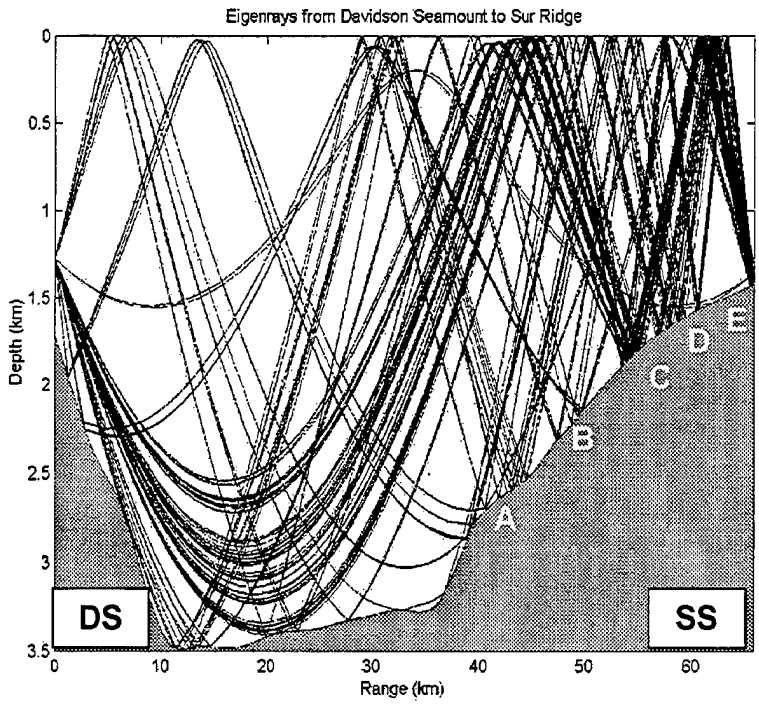

Figure 1.10. Cross-section view from Davidson Seamount to listening array on Sur Ridge, showing the interaction of eigenrays with bottom topography. DS = Davidson Seamount, SS = Sur slope. The white letters A-E indicate where Cores A-E were taken. From Onofre, 1999.

II. METHODOLOGY

A. CORE SAMPLING

Two research vessels were used to collect the sediment cores; the R/V Point Sur (Moss Landing Marine Laboratories, or MLML), and the R/V New Horizon (Scripps Institute of Oceanography). The cores taken on R/V Point Sur had liners that were 7.62 cm in diameter, with liners made of polycarbonate. Those taken on R/V New Horizon had liners that were 5.08 cm in diameter, and were also made of polycarbonate. Core diameter and material can alter measurements of the physical properties of core sediment and need to be known to correct for discrepancies when conducting acoustic analyses of the sediment.

Table 2.1 shows the latitude, longitude, depth, and overall length of the cores used in this investigation, as well as the date of sampling and the vessel from which the cores were collected. Figure 2.1 illustrates the bathymetry around Sur Ridge and the location of each core. Once the cores were removed from the sampling tube, end caps were placed on the liners and then tightly sealed with electrical tape. Cores taken on R/V Point Sur had to be laid on their side to be removed from the barrel; this caused the upper and lower parts of the cores to be slightly deformed due to the pull of gravity acting on their horizontal orientation. This deformation of the upper and lower parts of the cores impacts the accuracy of the acoustic analysis in those parts deformed and distorts the physical appearance of the sediment. The cores taken on R/V New Horizon were removed vertically. All gravity cores were stored upright after being trimmed and sealed.

CORE	LATITUDE	LONGITUDE	DEPTH (m)	CORE LENGTH (cm)	DATE TAKEN	VESSEL
A	N36°07.20'	W122°30.43'	2553.0	116	10 Sep 00	NH
B	N36°09.59'	W122°29.00'	2285.0	141	10 Sep 00	NH
C	N36°11.94'	W122°27.51'	1948.0	148	10 Sep 00	NH
D	N36°14.86'	W122°26.42'	1672.0	120	10 Sep 00	NH
E	N36°17.95'	W122°24.03'	1435.0	146	30 Jul 00	PS
F	N36°21.29'	W122°22.18'	1232.0	187	30 Jul 00	PS
G	N36°22.38'	W122°17.26'	1341.0	46	30 Jul 00	PS
H	N36°22.46'	W122°11.09'	851.3	160	30 Jul 00	PS
I	N36°18.39'	W122°17.69'	1128.0	45	30 Jul 00	PS
J	N36°18.45'	W122°21.14'	1157.0	30	12 Sep 00	NH
K	N36°16.49'	W122°13.35'	855.0	8	12 Sep 00	NH

Table 2.1. Table showing the location, depth, and overall length of each core, as well as the date taken and vessel used for sampling. NH = R/V New Horizon, PS = R/V Point Sur.

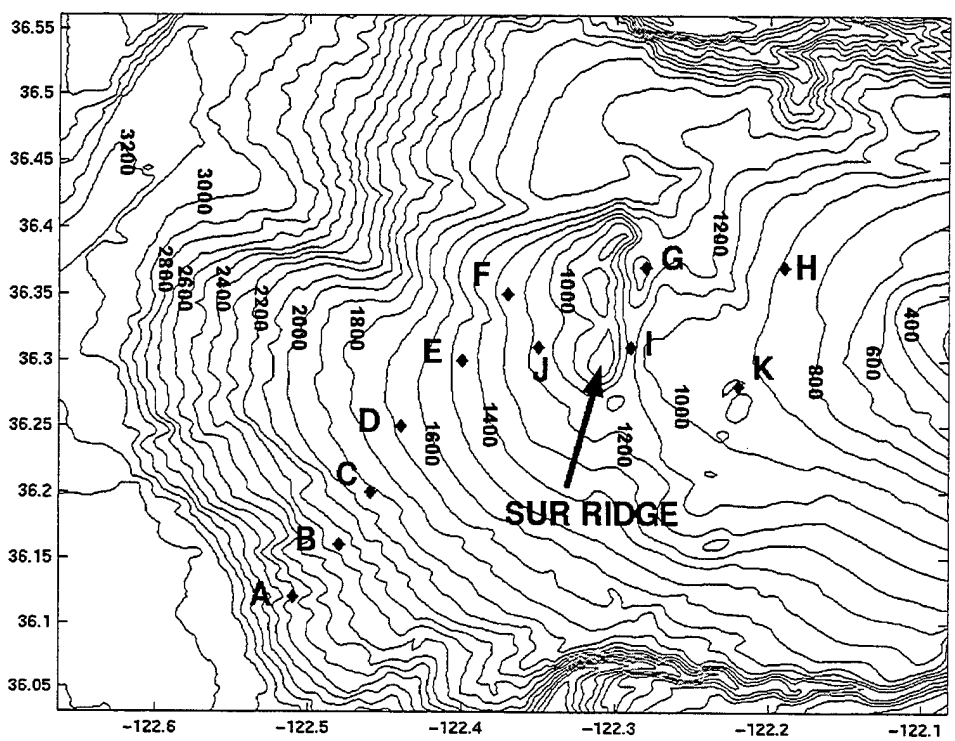

Figure 2.1. Plan view showing the locations of the gravity cores taken in relation to Sur Ridge. Bathymetry is in meters.

R/V New Horizon also was able to provide cold storage (~3°C) for the cores; R/V Point Sur was not. The sediment cores were kept in refrigeration to help maintain their *in-situ* environmental temperatures, as well as retard any biologic growth that may disrupt the sediment structure. Upon the ship's arrival at Moss Landing, the cores were temporarily stored in the refrigerator at Monterey Bay Aquarium Research Institute (MBARI), and then transported at a later date to the U.S. Geological Survey Laboratory in Menlo Park for nondestructive testing. Upon the completion of the nondestructive testing, the cores were transported back to the MBARI refrigerator, where they were kept refrigerated until they were split in half, analyzed for sedimentological features, photographed, and then sub-sampled. Both the archive half and sub-sampled half were wrapped in plastic wrap for storage at MBARI. Subsamples were placed in whorl-packs, labeled, and then transported to MLML for grain-size analysis.

B. ACOUSTIC SEDIMENT ANALYSIS

The first tests that were conducted consisted of nondestructive laboratory testing; nondestructive meaning the sediment cores remained undisturbed during the testing. Acoustic sediment analysis is becoming increasingly useful in sedimentology, as the measurements it provides can show characteristics about the sediment that otherwise would not be seen with other analyses.

Geotechnical analyses were conducted at the U.S. Geological Survey geotechnical laboratory in Menlo Park, California. The multi-sensor whole-core sediment-logging device was built in Great Britain by Geoteck, Ltd (Figure 2.2). Three properties were

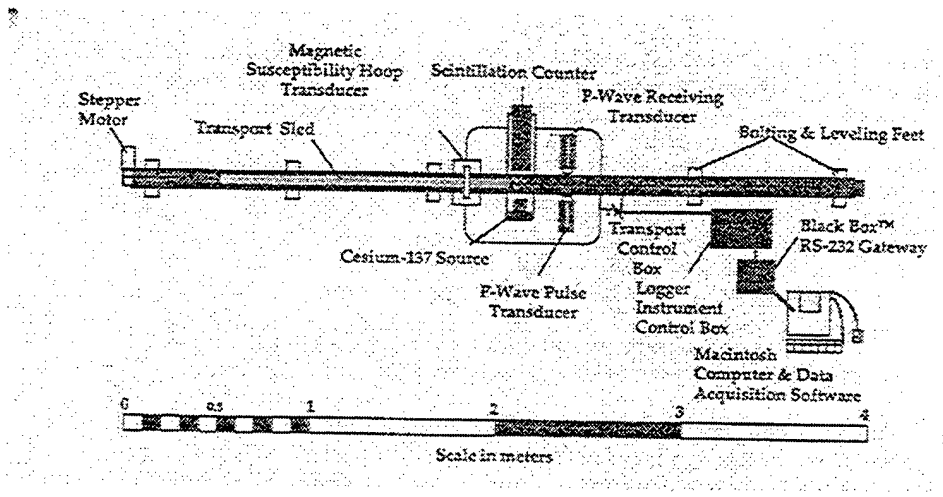

Figure 2.2. Plan view of the multi-sensor core sediment logging device. From Kayen, et al., 1999.

measured: (1) soil compressional wave velocity, (2) Lambert soil wet bulk density, and (3) magnetic susceptibility. Cores E-I were analyzed on 10 October 2000, and Cores A-D were analyzed on 13 October 2000. Cores J and K were not analyzed due to extensive deformation during the core retrieval process.

While undergoing the acoustic analysis procedure, the sealed sediment cores are placed horizontally upon a transport sled and moved by a computer-controlled stepper motor through a frame supporting three sensors (Figure 2.2) (Kayen, et al., 1999). The first sensor measures core diameter and the travel time of the pulse to compute p-wave velocity. The next sensor measures attenuation of gamma rays from a Cesium-137 source to compute soil wet bulk density. The final sensor measures magnetic susceptibility of soil particles via a magnetic field hoop. Measurements are typically taken at 1-centimeter increments. The transport sled is capable of carrying individual core sections up to 1.5 meters in length. A 1.5-meter length of core typically takes 35 minutes to analyze. A software program has been developed to automate the acoustic

analysis system and support a number of user and system tailored scanning options. Data retrieved from the core was placed in an Excel spreadsheet for further use, and can be found in Appendix A.

To ensure proper functioning of the equipment, a calibration core is constructed and used to calibrate the sensors. Calibrations are conducted prior to the analysis of the first core, and then after every 3-4 cores to ensure proper functioning of the sensors. The calibration core is constructed using the same core liners and endcaps as those used in the sediment cores. Approximately half of the core (50 cm) is filled with aluminum that has been shaped to completely fill the inside diameter of the core. The other half (50 cm) is filled with distilled water. The densities and velocities of both the aluminum and distilled water are known, and are then used to adjust the settings as needed.

The data that was retrieved from the sediment cores for this study was transferred from the Excel spreadsheet format to that of a data matrix for use in MATLAB 5.3. Using MATLAB 5.3, the compressional wave velocity, wet bulk density, and magnetic susceptibility profiles from each core were plotted alongside glauconite percentage and median grain size profiles (from the grain-size analysis). The profiles from each core were analyzed, and then compared and contrasted to surrounding profiles to determine spatial variability and look for any physical trends or sedimentary layers. Detailed acoustic descriptions for each core are contained in Appendix B.

1. Compressional Wave Velocity

Compressional wave velocity of sediment is calculated from the measured core diameter and wave-travel time. Corrections are made for the liner thickness, electronic signal delays associated with the travel time within the transducer head, and core liner

travel time. The transmitter and receiver transducer sit opposite to one another and orthogonal to the direction of core motion (Figure 2.2). The transmission frequency used is 500 kHz, with a repetition rate of 100 kHz. The accuracy of the travel time measurement is within 15 nanoseconds. The compressional wave velocity of the soil is also affected by pore-water salinity, temperature, total confining pressure, and soil bulk density. The velocity measurements must be corrected to a standardized, common reference state (23°C, 1 atmosphere). The mean-measured sound speed for distilled water at 23°C is within 0.05% of the known value; the standard deviation for sound speed is +/- 0.16% of the mean measured value.

2. Wet Bulk Density

Wet bulk density is the ratio of total soil weight to soil volume, taking into acount pore water density. To measure bulk density, the core passes through a one-centimeter columnated beam of gamma rays from a radioisotope Cesium-137 source. A scintillation counter sits opposite of the beam, orthogonal to the direction of core motion (Figure 2.2). Using Lambert's law and the gamma ray attenuation characteristics, as well as accounting for the influence of the core liner, the sediment bulk density (ρ_b) can be calculated using equation (1):

$$\rho_b = \frac{\ln(I_o/I) - \mu_1 \rho_1 2l}{\mu_s (D-21)} \qquad (1)$$

Where I_o is the unattenuated gamma count, I is the attenuated gamma count, μ_1 is the Compton scattering coefficient for the core liner, ρ_1 is the core liner wall density, l is the core liner wall thickness, μ_s is the soil Compton scattering coefficient, and D is the outer diameter of the core (Kayen, et al., 1999). The mean value of the calculated and

measured density of distilled water was within 0.4% of the known value, and the mean value for aluminum was exactly the known value. Standard deviation for density measurements is on the order of 0.6-1.0% of the measured value.

3. Magnetic Susceptibility

Magnetic susceptibility determines the magnetic qualities of the sediment within the core. The core passes through a magnetic field hoop as it is scanned. Changes in the magnetic field due to the magnetic properties of sediment are recorded along with the compressional wave velocity and wet bulk density.

4. Discussion

Although it is currently impossible to obtain detailed *in-situ* information about sediment composition, structure, and acoustic properties without disturbing the sediment, it is possible to correct laboratory values to *in-situ* values via regression equations and relationships. Appendix C contains a discussion of the methods used to correct laboratory values to *in-situ* values, as well as to determine other acoustic properties of the sediment. The acoustic relationships of the various sediment properties will be discussed in Chapter III.

The chosen method of sampling the sediment for this study was via gravity coring. In the process of obtaining the sediment core, the sediment experienced slight deformation along the boundaries of the core liner due to drag of the sediment along the liner walls. In the smaller diameter cores this deformation is more significant. This deformation could cause slight differences in density and velocity measurements, depending on the composition of the sediment. In addition, when the core barrel impacted the uppermost layer of the sediment, it disturbed the top layer of poorly

consolidated sediment. This disturbance was further exacerbated during the process of trimming the liner so that it would fit into the acoustic analysis equipment. Thus the uppermost sediment layer displayed a slightly distorted picture of the *in-situ* acoustic characteristics of the sediment. However, the layer was very poorly consolidated, containing a very large percentage of seawater, so the disturbances caused by the impact of the gravity core and subsequent trimming were minimal.

Three cores displayed small cracks within the sediment running lengthwise along the core, which led to further displacement of the sediment. The liners themselves did not crack. This localized cracking was caused by a combination of factors, most notably the motion during transport of the cores, and the lack of support at the bottom of the liner. However, the cracking and displacement was localized in most cases, and the effects were minimized by positioning the core in the sled of the acoustic analysis equipment such that the sensors avoided the areas that were cracked or displaced. In addition, small amounts of seawater contained in cores E-I leaked out, exposing some of the upper and lower surfaces to air, drying out parts of the upper and lower layers of the sediment and interfering with the acoustic sensors. However, the effect of the dry sediment was mitigated by the presence of the plastic end caps. The plastic endcaps affected the ability of the sensors to properly measure the acoustic characteristics of the upper and lower sediment layers in the cores and thus created a gap of information at the top and bottom of each core. Also, Cores F and H had to be cut in half to process them through the acoustic analysis equipment, so both cores also have a gap of acoustic information at their midpoints, as well as at the top and bottom of the core. Temperature of the

sediment is not a factor, as the software for the acoustic analysis equipment contains an algorithm that accounts for temperature differentials and corrects the measurements.

Overall, while the data obtained from the acoustic analysis experienced some degradation and loss of information due to the above-mentioned factors, extremely accurate profiles of the various properties of the sediment were still determined. Numerous steps were taken to ensure minimization of error within the data set; the majority of cores were analyzed twice to ensure the accuracy of the data.

C. PHYSICAL DESCRIPTION OF THE CORES

Upon splitting each core in half, a detailed analysis was conducted and all cores were photographed in detail. The sediment were examined for visible features such as signs of bioturbation, fossil content, mineral content, consolidation of the sediment, sorting of the sediment, color and texture, and any layering or stratigraphy present, as well as sediment structures. Appendix D contains a detailed physical description of each core, as well as images of the split cores.

D. GRAIN-SIZE ANALYSIS

Using the acoustic profiles and the results of the general physical description, subsamples of sediment were taken from the cores, both to compare with the acoustic profiles and to obtain an overall composition and grain-size distribution for the sediment. A total of 74 subsamples were taken for grain-size analysis. Appendix E shows the subsamples taken for each core.

Subsamples were taken out of the whorl-pakcs and were placed in pre-weighed 100-ml beakers, weighed, and then placed in a drying oven at 60°C for 48 hours. The beakers were then removed from the oven, allowed to equilibrate with the ambient room

temperature (22°C) for over an hour, and re-weighed. The beakers were then filled with distilled water and 15 ml of Calgon dispersant, so that each beaker had a total of 100 ml of solution. The dispersant was added to prevent flocculation of the finer material. The beakers were then placed on an oscillating table for 48 hours to enhance the separation of all grains.

Table 2.2 shows the conversion from phi scale (φ) to millimeters. The phi scale is a logarithmic measurement of grain size and the preferred method of describing grain size. Upon completion of the oscillating table, each beaker was then wet-sieved using distilled water through a combination of 4φ and 6φ mesh sieves. A glass bowl was placed under the sieves to catch the water and fine-grained material. Sediment retrieved in the 4φ and 6φ sieves were placed in pre-weighed aluminum tins and dried in the oven at 60°C for 48 hours in preparation for dry-sieve analysis. The water and sediment in the glass bowl was placed in a 1000 ml-graduated cylinder in preparation for pipette analysis.

U.S. STANDARD SIEVE MESH	METRIC (mm)	PHI (φ) UNITS	WENTWORTH SIZE CLASS
10	2.00	-1.0	Granule
18	1.00	0.0	Very coarse sand
35	0.50	1.0	Coarse sand
60	0.25	2.0	Medium sand
120	0.125	3.0	Fine sand
230	0.0625	4.0	Very fine sand
400	0.0156	6.0	Medium silt
---	0.0078	7.0	Fine silt
---	0.0039	8.0	Very fine silt
---	0.0020	9.0	Clay
---	0.00098	10.0	Clay

Table 2.2. Conversion of phi scale to millimeters, U.S. Standard sieve mesh, and Wentworth Size Class. Modified from Boggs, S. Jr., 1987.

1. The Dry-Sieve Process

Once the 4φ and 6φ sediment subsamples were dried, they were allowed to equilibrate with the ambient room temperature (22°C) for over an hour before weighing. After weighing, the 4φ and 6φ tins for each subsample were re-combined and dry-sieved through a series of sieves. The series of sieves used in the dry-sieve method was -1φ, 0φ, 1φ, 2φ, 3φ, 4φ, and 6φ. A catch pan was placed at the bottom of the sieves to collect any material finer than 6φ. The series of sieves was placed on the Ro-Tap machine for 15 minutes at a medium intensity setting. The Ro-Tap machine is a mechanical device that horizontally oscillates the stack of sieves while simultaneously striking the top of the sieve stack. This assists in sorting out the sediment. After going through the Ro-Tap machine, each sieve was placed upside-down on a large, pre-weighed coffee filter, and gently tapped to dislodge any sediment stuck in the sieve. Wax paper was laid under the filter to minimize the amount of lost sediment. Each coffee filter was then folded and re-weighed. The weights of the sediment from each sieve were divided by the total weight of the sample to calculate the percentage of sediment that represented that grain size. Appendix F contains the dry-sieve weights and percentages for each grain size for all samples.

While every effort was made during the wet-sieve process to separate the coarse sediment (intended for dry-sieve) from the fine sediment (intended for pipette), it is almost impossible and certainly time-prohibitive to accomplish this fully. All subsamples had sediment finer than 6φ in the catch pan, indicating that not all of the fine material was filtered out during the wet-sieve. The proportion of sediment finer than 6φ was not significant; the average percentage of the total sample that was contained in the catch pan

was less than 3%. To account for this sediment, the distribution of percentages of sediment from 7φ to >10φ obtained from the pipette analysis was assumed to be accurate. The weight of the sediment from the catch pan was distributed from 7φ to >10φ based on this assumption.

2. The Pipette Process

The finer material retrieved from the glass bowl during the wet-sieve process was analyzed using pipette analysis (Folk, 1980). The theory of pipette analysis is based on the settling velocity of sediment particles, computed using Stokes' law. This is usually conducted for grain sizes up to 10φ. At present, there is no preferred settling method for particles finer than 11φ or 12φ, where Brownian motion interferes with settling.

In conducting the pipette analysis, the distilled water and sediment retrieved from the wet-sieve process was placed in a 1000 ml-graduated cylinder. Distilled water was added until the amount of water in the cylinder was exactly 1000 ml. The sampling times were determined by using the following equation:

$$T_{min} = \frac{Z}{1500 \cdot A \cdot d^2} \qquad (2)$$

Where T_{min} is time in minutes, Z is the depth in cm to which the pipette is placed in the cylinder, A is a viscosity constant that is based on the ambient air temperature of the laboratory and the composition of the sediment (based on the results of the physical description of the cores), and d^2 is the square of the particle diameter to be measured in mm. For this analysis, the ambient air temperature was 20°C, so A = 3.57 (Folk, 1980). Table 2.3 shows the following times and depths that were calculated for the pipette analysis.

TIME	GRAIN SIZE (mm)	PHI (φ)	DEPTH (cm)
0:00:20	Total amount	---	20
0:30:42	0.0078	7.0	10
2:02:47	0.0039	8.0	10
7:46:51	0.0020	9.0	10
16:12:12	0.00098	10.0	5

Table 2.3. Calculated times and depths for pipette analysis. From Folk, 1980.

To initiate a pipette analysis, the cylinder is first vigorously stirred, starting at the bottom and working up. This is to ensure a homogenous mixture of the sediment. The instant that the stirring rod is removed from the cylinder, the timer starts. Exactly 20 seconds after the start time, a 20 ml sample is taken from the cylinder at a depth of 20 cm. The sample is expelled into a pre-weighed aluminum tin, and 10 ml of distilled water is sucked into the pipette to rinse any remaining sediment in the pipette. This water is added to the sample as well. Samples are then taken at the specified time intervals and depths and placed in an oven set at 100°C for 24 hours to evaporate the water. Once the samples are removed from the oven, they are allowed to equilibrate with the ambient air temperature (22°C) for over an hour, and are then weighed.

Prior to calculating the percentages of sediment for each grain size sample, the weight of the dispersant is removed from each sample. Once this has been accomplished, the data is analyzed to determine the total mass per grain size of the sediment in the cylinder. The theory behind the set of calculations is that the sediment is uniformly distributed throughout the entire 1000-ml column by stirring. If exactly 20 ml is drawn off at specified times, then the amount of mud in each withdrawal is equal to 1/50 of the total amount of mud remaining suspended in the column at that given time and at that

given depth. All particles coarser than the given diameter will have settled past the point of withdrawal. The first withdrawal is made so quickly after stirring (20 seconds) and at such a depth (20 cm) that particles of all sizes are present in suspension; therefore if the weight of the first withdrawal is multiplied by 50, the weight of the entire amount of mud in the cylinder will be obtained. Then, if each 20 ml sample taken at the specified times and depths is multiplied by 50 (for example, the 7φ sample), the product represents the number of grams of mud still in suspension at this new time, therefore the grams of mud finer than 7φ. The difference between the 20-second sample and the sample taken at the 7φ time is the weight of sediment that is 7φ. Calculations for the other grain sizes were made in similar fashion. Appendix G contains the data showing the weights and percentages of sediment obtained from the pipette analysis. The combined data from the dry-sieve and pipette analyses produces a complete grain-size distribution for each subsample.

Sediment will invariably be lost during the procedures used in grain-size analysis. Sediment is lost any time it is transferred from one container to another, i.e. from a beaker to a wet-sieve. Sediment can also be lost by becoming embedded in the mesh of the sieves, during both wet and dry-sieving. All feasible efforts were undertaken to reduce the amount of lost sediment. The final cumulative percentages of each subsample were averaged to determine the amount of sediment recovered per subsample. The average amount of sediment recovered for each subsample was 97.4%.

III. RESULTS

A. ACOUSTIC ANALYSIS DATA

1. Correcting Laboratory Values to *In-situ* Values

The removal from *in-situ* conditions to those in the laboratory affected the profiles of compressional wave velocity and wet bulk density. All cores were taken at a depth of 850 m or greater, at temperatures ranging from 1.8-4°C and pressures ranging from 850-2500+ decibars, and then brought to the surface. To reproduce *in-situ* values, the data from the acoustic analysis was corrected. A discussion of the procedures used to correct the velocity and density profiles are contained in Appendix C. The corrections for the velocities and densities play a significant role in understanding acoustic tomography, to be discussed in Chapter IV. Figure 3.1 shows the magnitude of change for both compressional wave velocities and wet bulk densities for each core after being corrected to *in-situ* values. The overall mean compressional wave velocity from laboratory to *in-situ* values increased by 40.4733 m/s, with a mean standard deviation of 0.3127. The overall mean wet bulk density from laboratory to *in-situ* values decreased by –0.007827 kg/m^3, with a mean standard deviation of 0.0003792. From the graph it can be seen that, while density corrections are near negligible, velocity corrections are significant for all cores, and particularly for the cores taken at more shallow depths.

2. Review of the Acoustic Properties of Sediment

Hamilton (1970a, 1970c, 1971, 1972, 1974, 1976, 1978) and others have derived numerous important relationships concerning the acoustic properties of sediment. The composition and size of the grains control sediment density. In most cases, denser

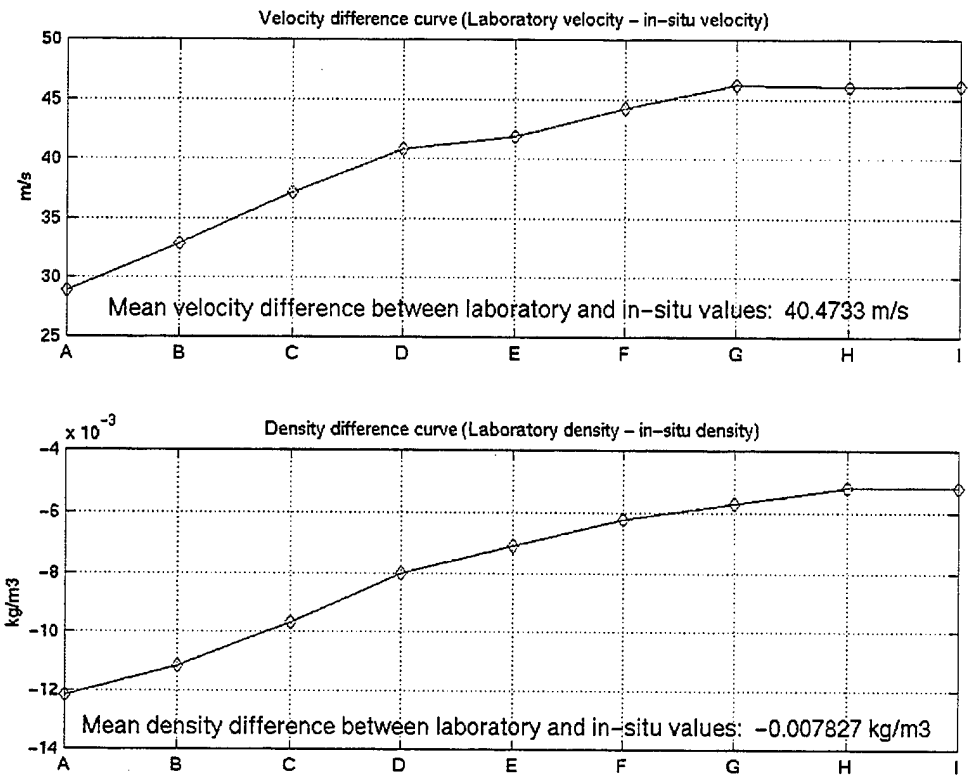

Figure 3.1. Graph showing the difference between the laboratory and *in-situ* mean values for compressional wave velocity and wet bulk density for Cores A-I.

sediment will have a larger median grain size. Density also can increase due to the consolidation and dewatering of sediment due to overlying pressure. This increase in density due to consolidation also greatly affects the porosity of sediment; the more consolidated the sediment, the less space is available for pore water, and so the porosity decreases. Furthermore, the density, and thus the porosity, of the sediment plays a large role in affecting the compressional wave velocity. Since it is the pore water that plays a significant role in propagating the compressional wave (Hamilton, 1970a), the loss of pore water has a serious impact on the compressional wave velocity. Thus a decrease in pore water will increase density but will cause a decrease in compressional wave

velocity. However, at some point in the sediment column, the density of the sediment overshadows the loss of pore water, and will begin to increase the compressional wave velocity. The presence of glauconite also has a significant impact on median grain size, density, and magnetic anomaly values. As glauconite is an iron rich mineral, an increase in glauconite in the sediment will cause the magnetic anomaly to become very strongly positive. In addition, since glauconite grains are typically larger and denser than their surrounding sediment, an increase in the percentage of glauconite will result in an increase in the density. Finally, the increase the coarseness of the sediment due to a high percentage of glauconite will lead to an increase the compressional wave velocity.

B. SUMMARY OF ACOUSTIC PROPERTIES BY CORE

1. Core A

Appendix C contains detailed descriptions of the acoustic profiles for each core. Figure 3.2 shows *in-situ* compressional wave velocity, wet bulk density, magnetic susceptibility, glauconite percentage (percentage of sediment that is composed of glauconite), and median grain-size profiles for Core A. The upper 60 cm of Core A shows a steady increase in density with depth, with a corresponding steady decrease in the velocity with depth. This is most likely due to the fact that the upper 20 cm of the sediment is poorly to moderately consolidated; deeper than 20 cm the sediment becomes well consolidated. As the sediment becomes more consolidated, porosity decreases and the velocity decreases, due to loss of pore water. In addition, the magnetic anomaly shows a positive trend in the upper 45 cm of the core, and the median grain size shows a coarsening at ~45 cm, which compliments the density and velocity profiles. Between 60-80 cm the density decreases, and the magnetic anomaly goes from being weakly positive to weakly negative, while the median grain size decreases as well. Below 80 cm, the

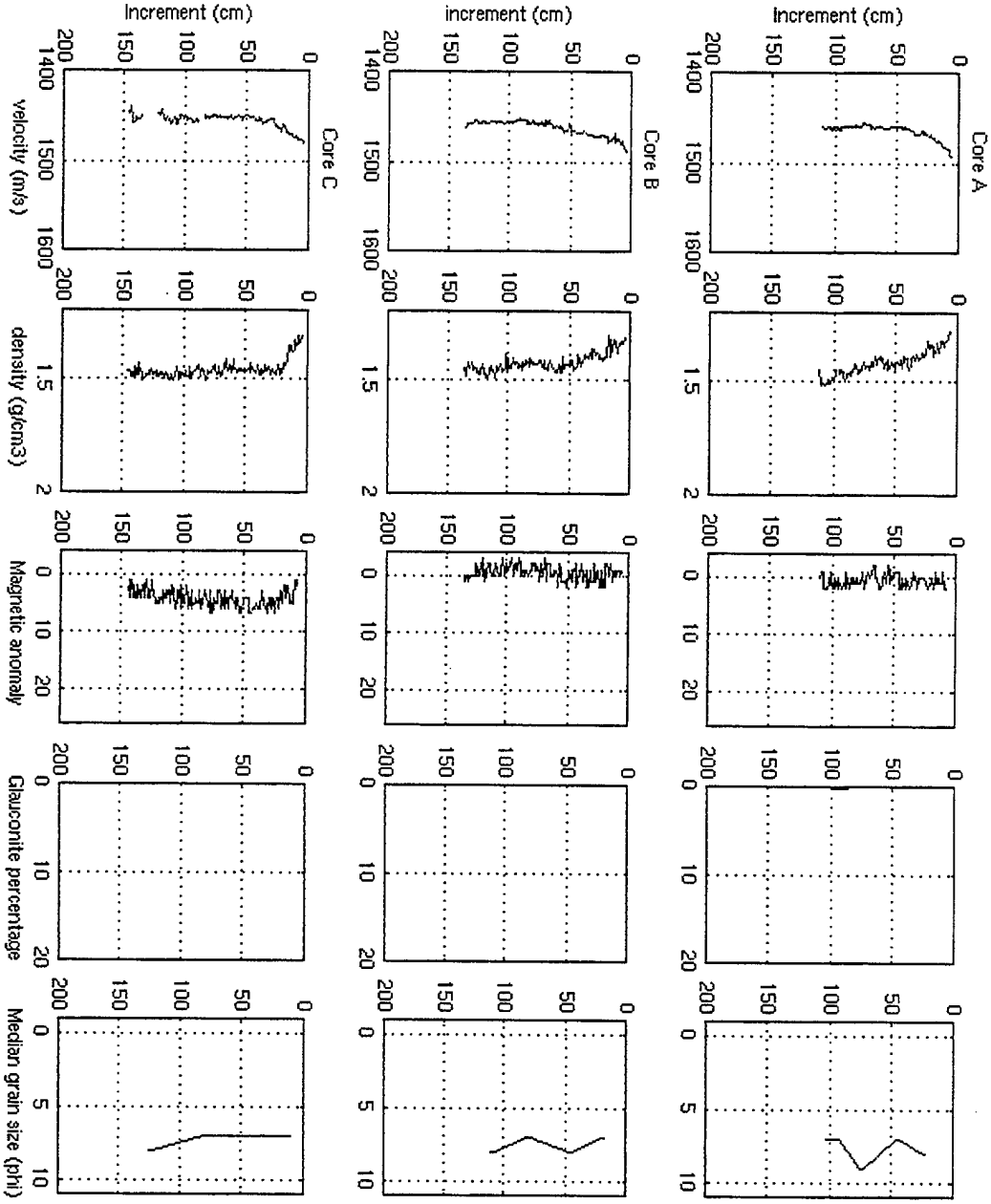

Figure 3.2. *In-situ* compressional wave velocity, wet bulk density, magnetic susceptibility, glauconite percentage, and median grain size profiles for Cores A-C. Gaps at the top of the profiles are due to the endcaps.

density increases, with a corresponding increase in the magnetic anomaly and a coarsening in the median grain size. This lower section could indicate a fining-upwards sequence in the sediment. Only trace amounts of glauconite were found in Core A.

2. Core B

Figure 3.2 shows *in-situ* compressional wave velocity, wet bulk density, magnetic susceptibility, glauconite percentage, and median grain size profiles for Core B. The upper ~60 cm of Core B shows a steady increase in the density with depth, with a steady decrease in the velocity with depth, much like Core A. Like Core A, the upper 10 cm of Core B is composed of poorly to moderately consolidated sediment, which agrees with the density and velocity profiles. The magnetic anomaly profile also supports the density and velocity profiles, becoming weakly positive where density increases. However, the median grain size profile does not correspond to the density and magnetic anomaly profiles. From 60-80 cm the density decreases, with the magnetic anomaly corresponding by becoming weakly negative, but a coarsening of the sediment is also seen. From 80-120 cm the density begins in increase, and again the magnetic anomaly profile increases as well, yet the median grain size profile shows a fining of sediment. Only trace amounts of glauconite were found in Core B.

3. Core C

Figure 3.2 shows *in-situ* compressional wave velocity, wet bulk density, magnetic susceptibility, glauconite percentage, and median grain size profiles for Core C. The upper 25 cm of Core C shows a steady increase in density as velocity steadily decreases with depth. The upper 10 cm of the core is composed of poorly to moderately consolidated sediment, much like Cores A and B, so this agrees well. In addition, the magnetic anomaly shows a positive increase as density increases. Below 25 cm the

density remains uniform, but the velocity continues to steadily decline until 40 cm, where it levels out. Likewise the magnetic anomaly also appears to be constant below 25 cm and from 60 cm gradually decreases to the bottom of the core. Density begins to slightly increase starting at 70 cm, with a corresponding decrease in median grain size. Overall magnetic susceptibility shows a slightly stronger positive anomaly data than seen in Cores A and B, due to a slightly higher increase in the percentage of glauconite within the sediment.

4. Core D

Figure 3.3 shows *in-situ* compressional wave velocity, wet bulk density, magnetic susceptibility, glauconite percentage, and median grain size profiles for Core D. The upper 35 cm of Core D show a steady increase in density with depth, with a corresponding decrease in velocity with depth. This is most likely attributed to the consolidation of the sediment, although Core D does not have the poorly to moderately consolidated layers that Cores A-C have. The change in magnetic anomaly corresponds with the increase in density as well. From 35-80 cm the density decreases, and then slowly begins to increase; in this instance, the velocity increases with the density, while the magnetic anomaly slowly decreases. From 85-95 cm the density decreases rapidly, then increases from 95-115 cm. The velocity appears to mirror this sequence, increasing where the density increases, and decreasing where the density decreases. The magnetic anomaly continues to slowly decrease through this sequence. Median grain size throughout Core D remains constant. Overall magnetic susceptibility shows a stronger positive anomaly data than seen in Cores A and B, due to an increase in the presence of glauconite.

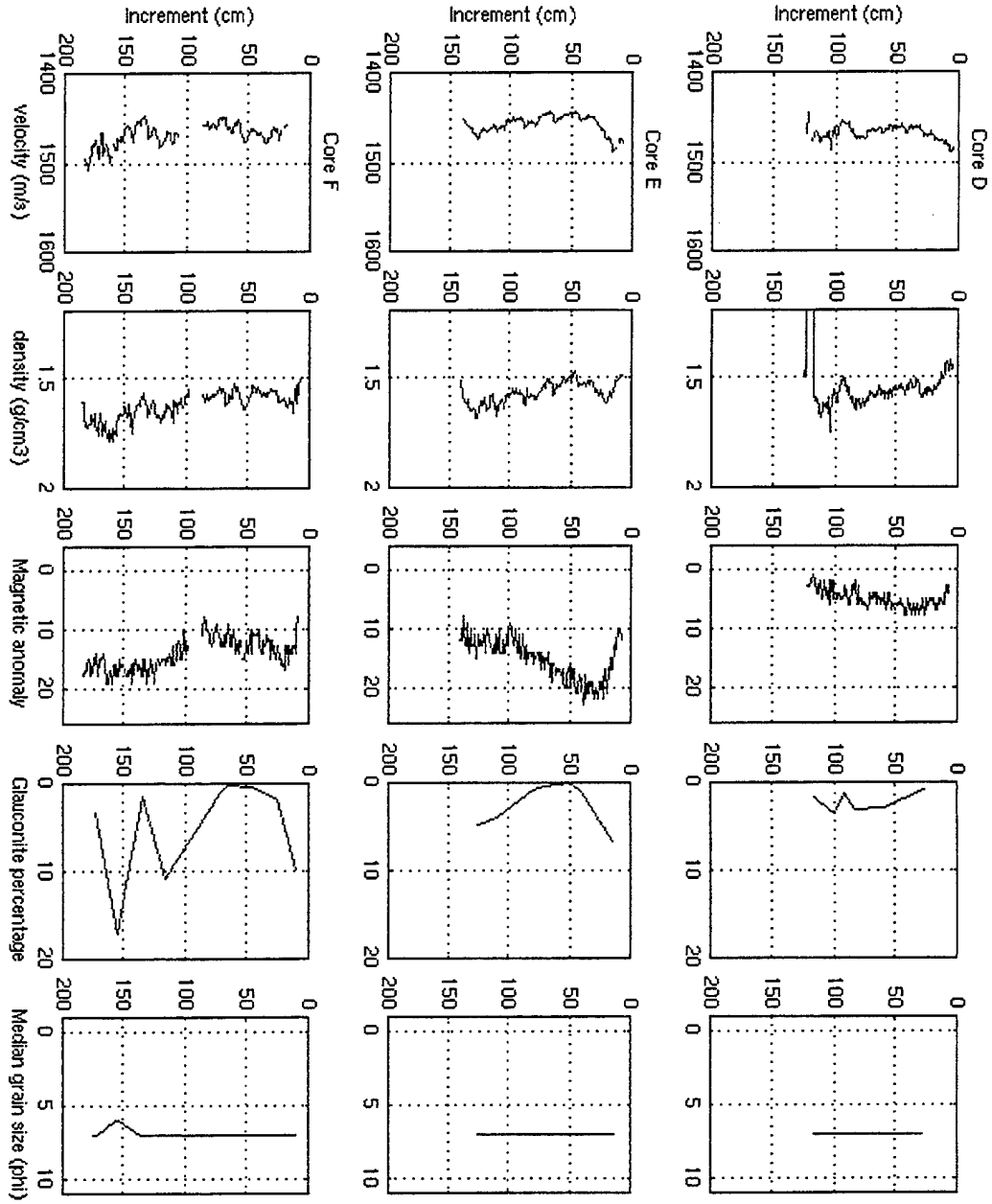

Figure 3.3. *In-situ* compressional wave velocity, wet bulk density, magnetic susceptibility, glauconite percentage, and median grain size profiles for Cores D-F. Gaps at the top of the profiles are due to the endcaps. Due to the length of Core F, it was necessary to split it in half to fit in the acoustic analysis equipment and thus has missing data in the middle.

5. Core E

Figure 3.3 shows *in-situ* compressional wave velocity, wet bulk density, magnetic susceptibility, glauconite percentage, and median grain size profiles for Core E. The upper 20 cm of Core E shows a steady increase in density with depth, with a corresponding increase in the magnetic anomaly profile with depth. Below 20 cm the density shows a complex set of increases and decreases; what is interesting is that the velocity appears to mirror exactly the density profile. Where density increases, velocity increases likewise. Overall the density shows a strong decrease from 20-35 cm, then slowly increases with depth up to 135 cm, and then decreases below 135 cm. The magnetic anomaly profile shows a steady decrease with depth. Median grain size remains constant throughout the core. Magnetic susceptibility continues to show an overall increase of the positive anomaly; again, this is related to the increase in glauconite percentage in the sediment.

6. Core F

Figure 3.3 shows *in-situ* compressional wave velocity, wet bulk density, magnetic susceptibility, glauconite percentage, and median grain size profiles for Core F. Core F is very similar to Core E, in that the density, velocity, and magnetic anomaly profiles all appear to mirror each other. Where density increases, velocity and magnetic anomaly profiles also increase. Median grain size remains relatively constant throughout the core. In general, the upper half of Core F shows a decrease in density, velocity, and positive magnetic anomaly from the surface to 45 cm, where it begins to fluctuate until ~85 cm. The entire lower half of the core shows an increasing trend in density, velocity, and magnetic anomaly, with the median grain size becoming slightly coarser at the peak of

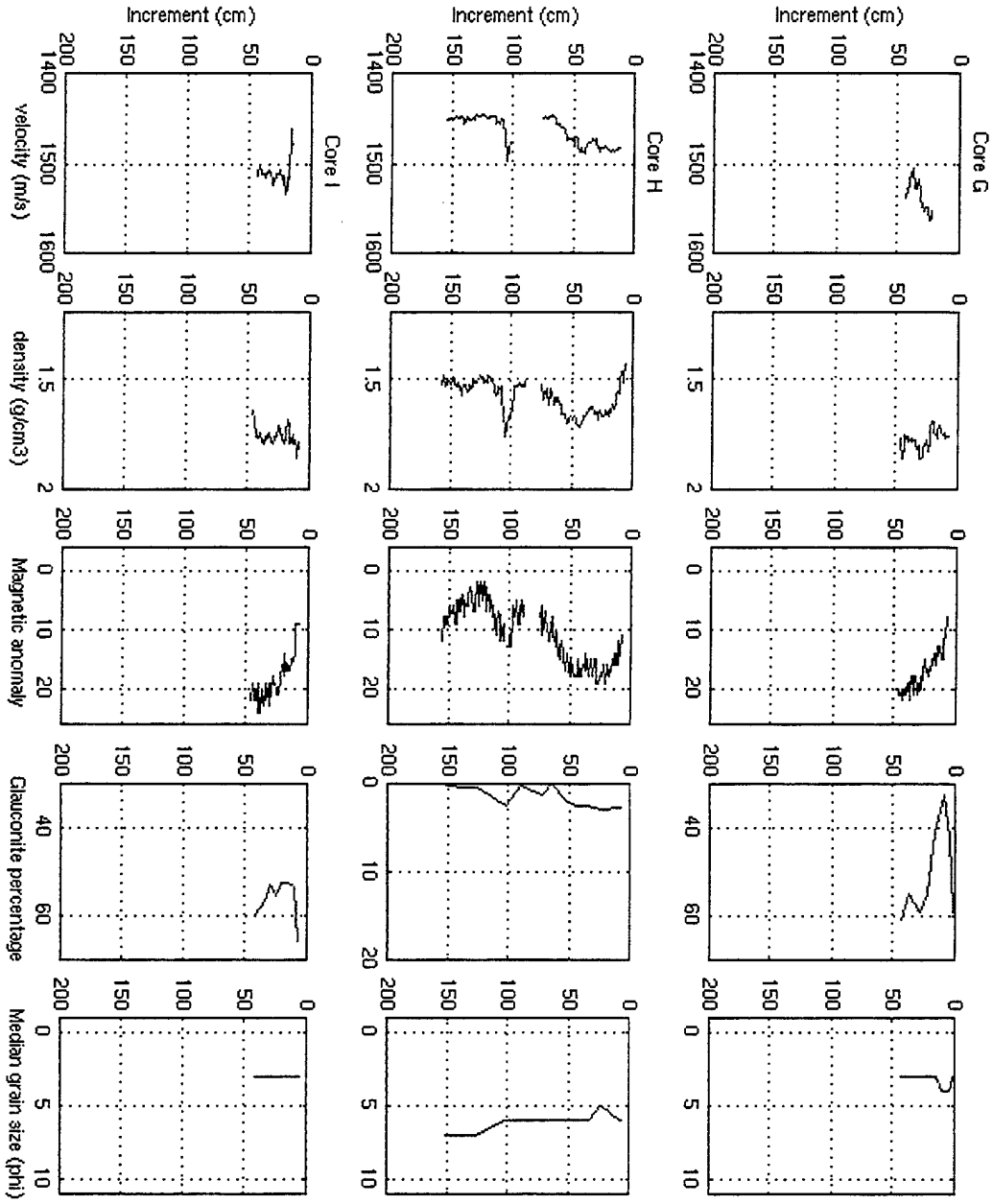

Figure 3.4. *In-situ* compressional wave velocity, wet bulk density, magnetic susceptibility, glauconite percentage, and median grain size profiles for Cores G-I. Gaps at the top of the profiles are due to the endcaps. Due to the length of Core H, it was necessary to split it in half to fit in the acoustic analysis equipment and thus has missing data in the middle.

the curves. Overall magnetic susceptibility data shows a very strong positive anomaly due to the increasing proportion of glauconite in the sediment.

7. Core G

Figure 3.4 shows *in-situ* compressional wave velocity, wet bulk density, magnetic susceptibility, glauconite percentage, and median grain size profiles for Core G. The majority of sediment within Core G is composed of glauconite, which has a tremendous impact on the shape of the profiles. The upper 20 cm of Core G shows a slow decline in density with depth, while the magnetic anomaly continues to be very strongly positive with depth. Median grain size shows a finer layer from 5-10 cm, but then coarsens in correspondence to the increasing magnetic anomaly profile. From 20-30 cm the density shows an increase, with a kink in the profile at 25 cm. This kink in the profile is also seen in the velocity profile, which is decreasing, and the magnetic anomaly profile, which is increasing. From 30-36 cm the density decreases, as does the velocity, while the magnetic anomaly continues to slowly increase. From 36-43 cm the density slowly decreases while the velocity begins to increase, and the magnetic anomaly remains relatively steady. The density profile from 43-47 cm shows a spike in the density, which is not seen in the velocity, median grain size, or magnetic anomaly profiles.

8. Core H

Figure 3.4 shows *in-situ* compressional wave velocity, wet bulk density, magnetic susceptibility, glauconite percentage, and median grain size profiles for Core H. The upper 20 cm of Core H show a steady increase in the density with depth, with a steady increase seen in the strongly positive magnetic anomaly profile with depth. The median grain size also coarsens, while the velocity remains somewhat steady. Below 20 cm the density appears to remain relatively constant until 55 cm, which is also seen in the

magnetic anomaly and velocity profiles. Indeed, the velocity and density profiles for this part of the core appear to mirror one another in their fluctuations. From 55-76 cm the density, velocity, and magnetic anomaly all decrease. Beginning at ~98 cm the density, velocity, and magnetic anomaly, and glauconite percentage profiles all show a significant positive spike, with all three curves rapidly increasing from 98-106 cm, and then rapidly decreasing from 106-115 cm. Associated with this rapid decrease in density, velocity, and magnetic anomaly, the median grain size also shows a slight fining, which continues for the remainder of the core. Below 115 cm the density shows a slight increase with depth to 142 cm, which is also seen from increases in the velocity and magnetic anomaly profiles. Below 142 cm the density and velocity profiles level out, while the magnetic anomaly profile continues to steadily increase. The strong positive magnetic anomalies seen in Core H are due to the strong presence of glauconite within the surrounding matrix of the fine-grained sediment.

9. Core I

Figure 3.4 shows *in-situ* compressional wave velocity, wet bulk density, magnetic susceptibility, glauconite percentage, and median grain size profiles for Core I. The majority of the sediment in Core I is composed of glauconite, which has a tremendous impact on the shape of the profiles, much like Core G. The upper 17 cm of Core I shows a decrease in the density with depth, while the magnetic anomaly profile shows an increase with depth. A sharp decrease, then increase, is seen in the density between 17 and 22 cm, which is also reflected in the magnetic anomaly profile. Below 22 cm the density and velocity profiles appear to mirror each other, with a decrease from 22-26 cm in both profiles, and an increase from 26-32 cm; the magnetic anomaly profile shows a decrease in its strongly positive anomaly during this section. From 32-34 cm the density

and velocity decrease, while the magnetic anomaly increases. From 34-37 cm the velocity and density level out, as does the magnetic anomaly; all three profiles remain relatively steady below 37 cm. Median grain size remains constant for the entire core.

C. SUMMARY OF PHYSICAL PROPERTIES

Appendix D contains detailed physical descriptions and images of each core. From the physical analysis of the split cores, there appear to be two distinct groups of cores, with Core F as a transition between the two groups.

1. Cores A-E and Core H: The Fine-grained Cores

Cores A-E and Core H showed homogeneous, fine-grained olive-green mud throughout the majority of the cores (Figure 3.5). Cores A-C, taken at 2553 m, 2285 m, and 1948 m respectively, had small sections (~10 cm) near the tops of the cores that showed a gradation from poorly to well-consolidated sediment. Cores D and E were taken at 1672 m and 1435 m, and Core H was taken at 851 m. All cores except for Core A displayed dark green patches of the same type of mud, both as bands and as splotches. Many of the darker areas appeared to be caused by bioturbation. Several pieces of organic material (shells, wood, etc.) were also found in the cores. All cores except Core E had small amounts of foraminifera tests throughout the sediment. The upper 60 cm of Core E had a high concentration of foraminifera tests.

2. Core G and Cores I-K: The Coarse-grained Cores

Core G and Cores I-K had a much different composition, being primarily composed of sand and silt-sized particles of glauconite (Figure 3.6). Core G was taken at 1341 m, Core I at 1128 m, Core J at 157 m, and Core K at 855 m. All of these cores displayed thick bands of sediment that were composed mainly of glauconite; in other glauconite bands a definite matrix of olive to dark green fine-grained, homogenous mud

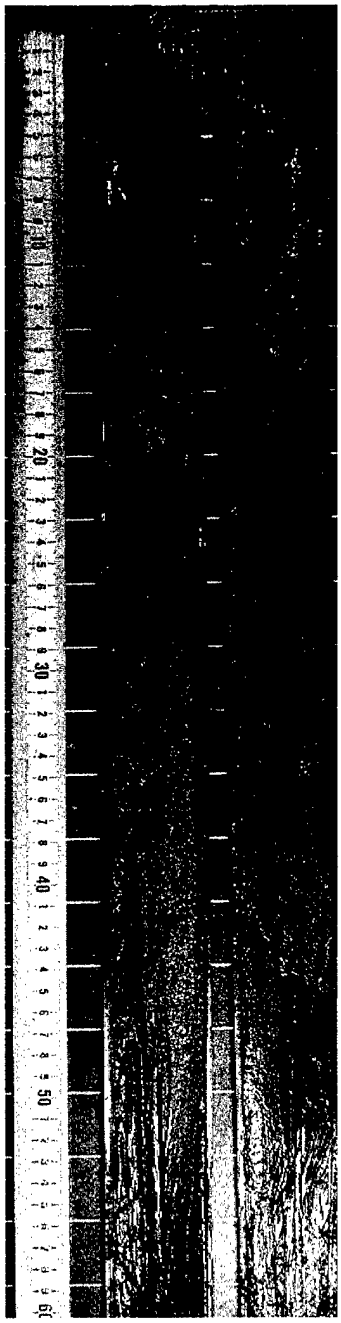

Core B: The upper 20 cm shows gradation from poorly to well-consolidated homogeneous, olive-green mud.

Core B: From 20-60 cm, the sediment is composed of well-consolidated, homogeneous, olive-green mud. Darker colored sediment, indicating possible bioturbation, is found from 25-55 cm.

Figure 3.5. Picture of Core B, 0-60 cm, as an example of a fine-grained sediment core.

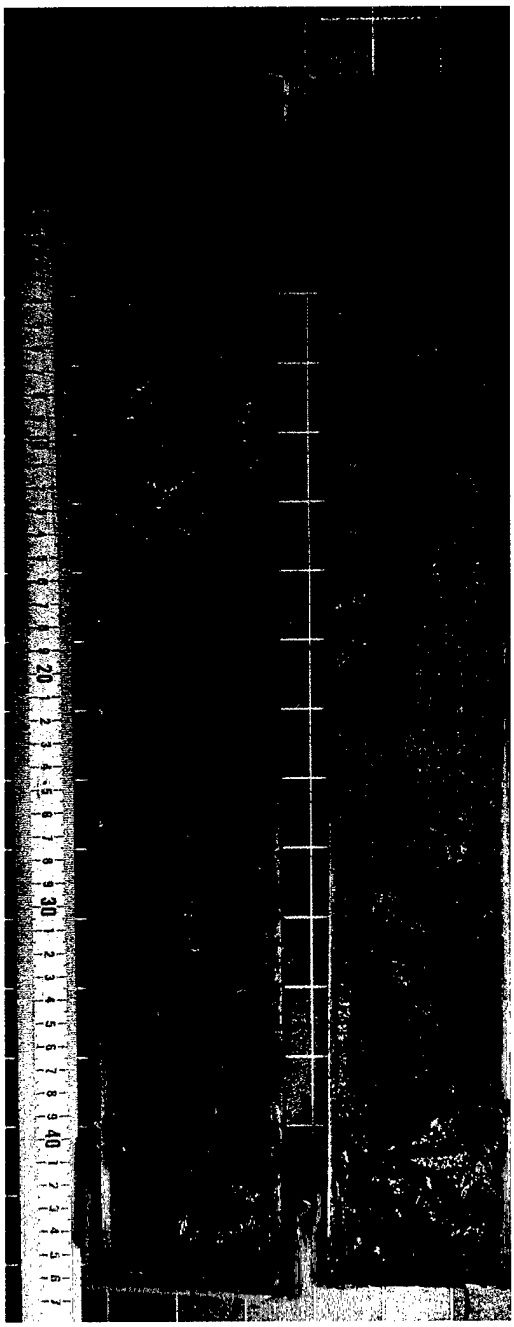

Core I: From 0-5 cm, the sediment is 99% glauconite grains.

Core I: From 5-30 cm, the sediment shows thick band of glauconite with an interstitial matrix of olive-green mud.

Core I: From 30-45 cm, the sediment shows localized patches of concentrated glauconite grains.

Figure 3.6. Picture of Core I, 0-45 cm, as an example of a coarse-grained sediment core.

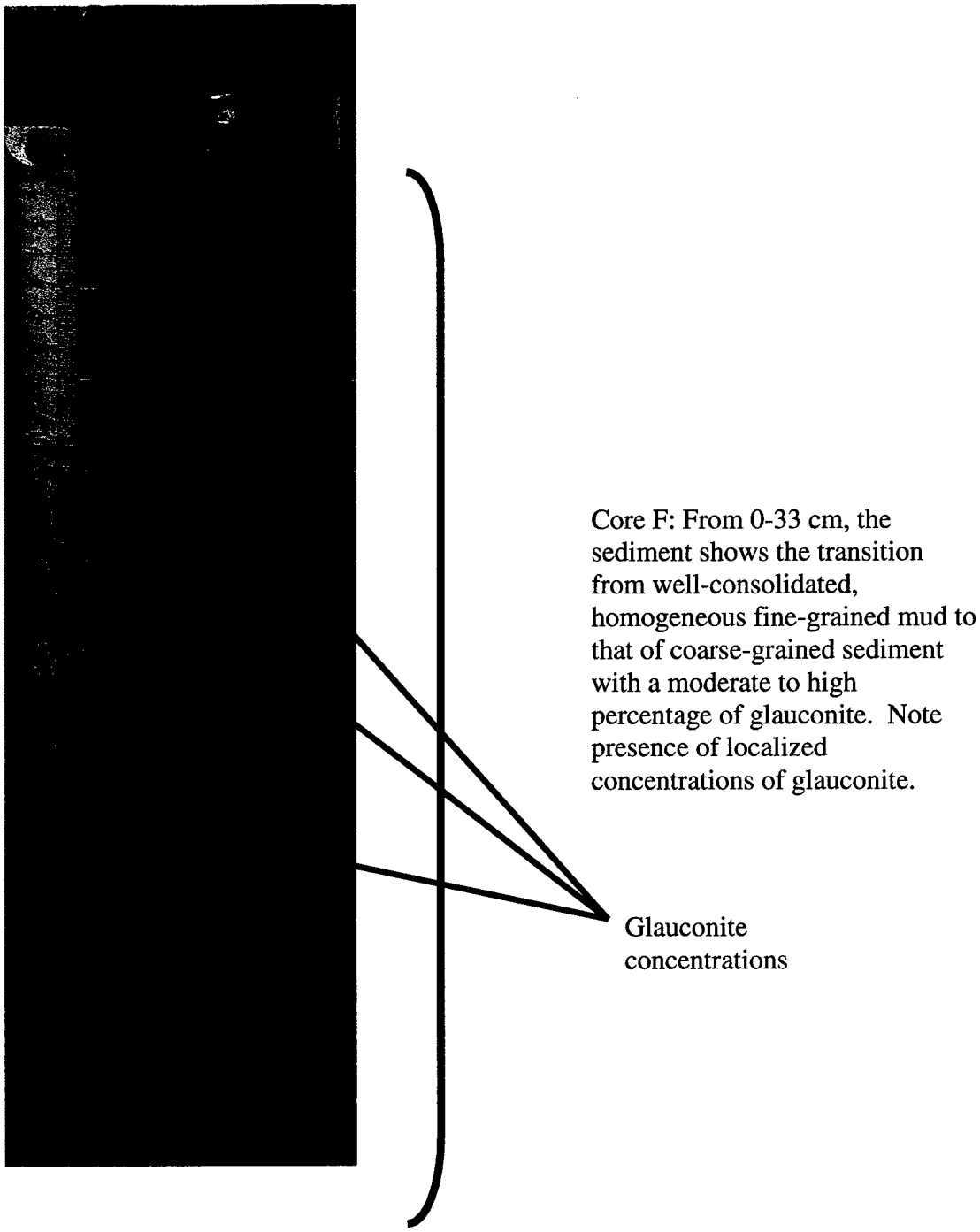

Figure 3.7. Picture of Core F, 0-33 cm, showing the transitional nature of the sediment. Note localized concentrations of glauconite.

was seen. Moderate to high concentrations of foraminifera tests were found within several of the glauconite bands in Cores G and I; occasionally parts of sponges were found as well. Cores J and K had low to moderate concentrations of foraminifera tests.

3. Core F: The Transition Core

Core F, taken at 1232 m, is unique in that it appears to be a transition between the two previously mentioned groups of cores. It is predominantly composed of the same homogeneous, well-consolidated, olive to dark green mud seen in Cores A-E and Core H, but also contains numerous concentrations of glauconite throughout the core, as seen in Core G and Cores I-K (Figure 3.7). Some glauconite concentrations had lens or ovoid shapes to them; others were splotchy. Low to moderate concentrations of foraminifera tests and other organic material was found throughout Core F.

4. Other Testing

Samples for Carbon-14 analysis were taken from Cores A, B, and G. Samples from Cores A-C and E-I were taken for DDT analysis. All DDT analyses were negative. Table 3.1 shows the core depths and ages of sediment. Figure 3.8 shows the data in graph format. From both the table and figure, the sediment near the surface of Cores A, B, and G appear to be from 4930 to 13050 years old, indicating that deposition in this area is either extremely slow.

5. Mineralogy

While conducting the physical description and grain-size analysis, it was noted that glauconite was found throughout all cores, in varying percentages. Indeed the vast majority of the sediment in Core G and Cores I-K is composed of glauconite. Glauconite

SAMPLE	AGE (YEARS BP)	± ERROR
Core A, 15-19 cm	8680.0	40.000
Core A, 80-85 cm	16850.0	60.000
Core B, 27-32 cm	4930.0	40.000
Core B, 110.115 cm	11960.0	40.000
Core G, 8-10 cm	13050.0	50.000

Table 3.1. Table showing Carbon-14 samples, ages, and error.

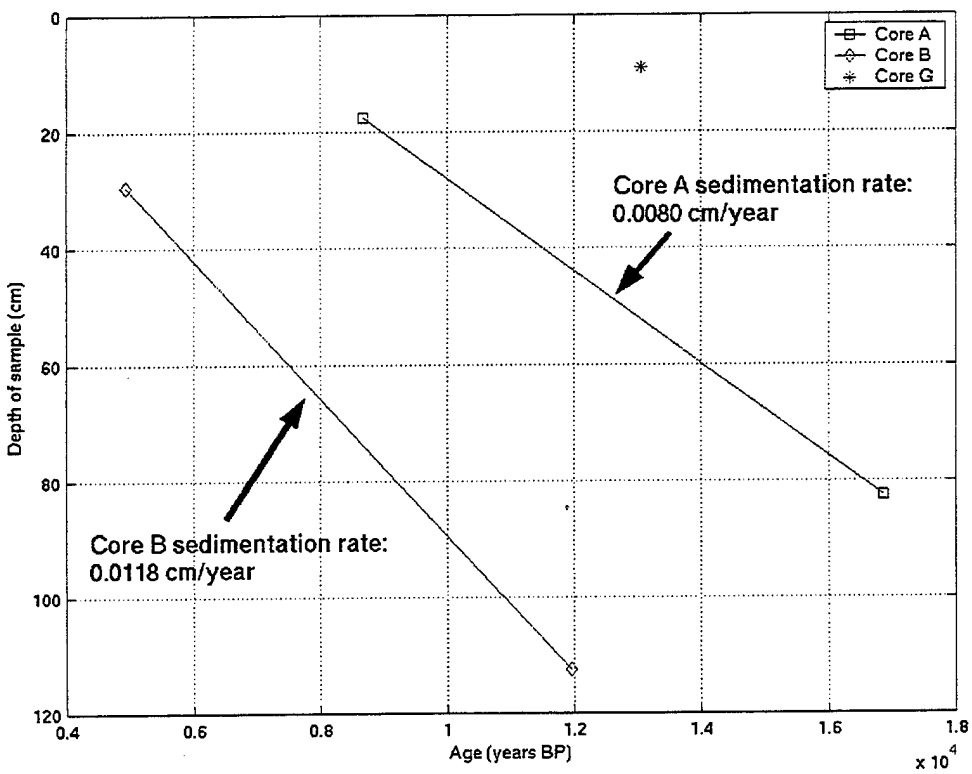

Figure 3.8. Graph showing Carbon-14 data for Cores A, B, and G, as well as linear interpolation of approximate sedimentation rates.

is an iron-rich aluminosilicate mineral that is authigenic in origin (Deer, et al, 1992). It is predominantly formed on shallow (100-300 m) continental shelves (Lim, et al, 2000), but can be formed in deeper waters, up to 600 m. While commonly found in recent sediment,

it is also found in Precambrian to Pleistocene deposits. Glauconite forms in areas with low sedimentation rates, low terrigenous material supply, and relatively flat, quiescent substrates. Requisite physiochemical conditions include low turbulence, low temperature, and an abundant supply of iron and potassium. Most importantly, the chemical properties of the water column need to be in a slightly reducing condition in order to provide the geochemical microenvironment suitable for the formation of glauconite (Lim, et al, 2000). Associated with this slightly reducing geochemical environment is the Oxygen Minimum Zone (OMZ). The reducing environment favorable for the formation of glauconite is typically found just above the OMZ. Finally, the shape of the glauconite grains is a direct result of the type of parent material. Parent materials include fecal pellets, rock fragments, altered mica or feldspar grains, and internal moulds or casts of microfossil tests, such as foraminifera tests. For this study, the vast majority of glauconite seen throughout the sediment was composed of fecal pellets.

6. Paleontology

The vast majority of fossils found throughout the sediment were composed of foraminifera tests. Although identification of genus and species of the tests was not within the context of this study, numerous species were present throughout the sediment. Also present throughout the sediment, although not nearly as frequent, was the presence of sponge spicules.

D. SUMMARY OF GRAIN-SIZE ANALYSIS

In conducting the grain-size analysis, four separate graphical representations of the data were created. These graphs include a histogram showing the distribution of grain sizes for each core, a cumulative percentage curve for each subsample, a median grain size profile, and a glauconite percentage profile for each core.

1. Core A

Core A was collected at a depth of 2553 m. Figure 3.9 contains the grain size distribution, cumulative percentage curves, median grain size profile, and glauconite percentage profile for Core A. From the histogram of grain size distribution for Core A, it can be seen that the dominant grain size for all samples is 7φ, which makes up 30-45% of the total sediment in each sample. The grain size distributions and cumulative percentage curves also show that the majority of the sediment in Core A is 7φ or greater. In addition, a significant percentage (15-20%) of the sediment is finer than 10φ, indicating that clay-size particles have a strong presence in this core. This sediment distribution holds true for the entire length of the core. The median grain size graph for Core A shows a moderate fining upwards of grain size from 93 cm to 73 cm (from 7φ to 9φ). The sediment then coarsens from 73 cm to 43 cm (from 9φ to 7φ) and slightly fines again from 43 cm to 23 cm (from 7φ to 8 φ). Only trace amounts of glauconite were found within the sediment.

2. Core B

Core B was collected at a depth of 2285 m. Figure 3.10 contains the grain size distribution, cumulative percentage curves, median grain size profile, and glauconite percentage profile for Core B. Core B is very similar to Core A in terms of sediment grain size and distribution. The histogram of grain size distribution for Core B shows that the dominant grain size for all samples is 7φ, which makes up 35-45% of the total sediment in each sample. The grain size distributions and cumulative percentage curves also show that the majority of the sediment in Core B is 7φ or greater. In addition, a significant percentage (15-20%) of the sediment is finer than 10φ, indicating that clay-size particles have a strong presence in this core. This sediment distribution holds true

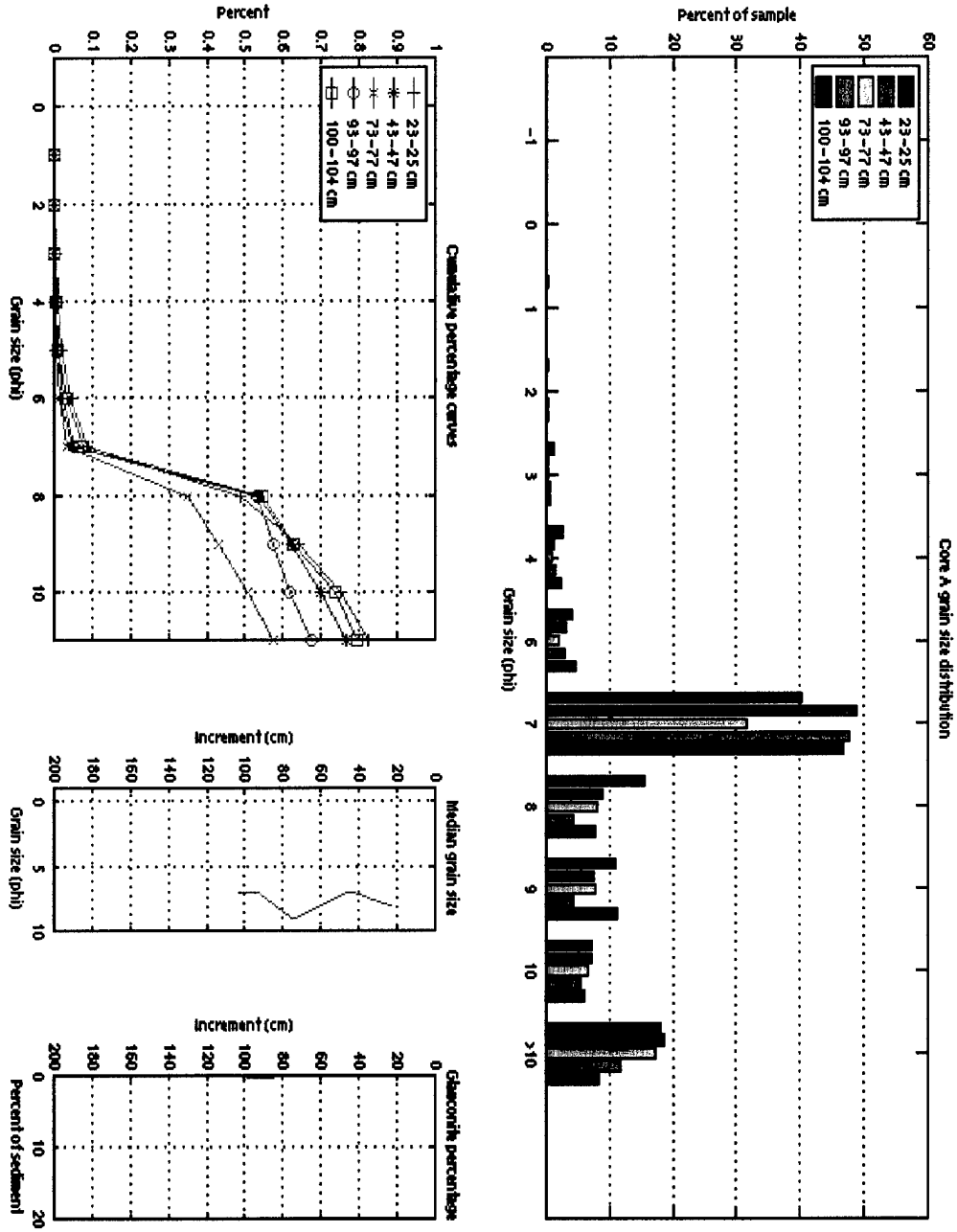

Figure 3.9. Grain size distribution, cumulative percentage curves, median grain size profile, and glauconite percentage profile for Core A, collected at 2553 m.

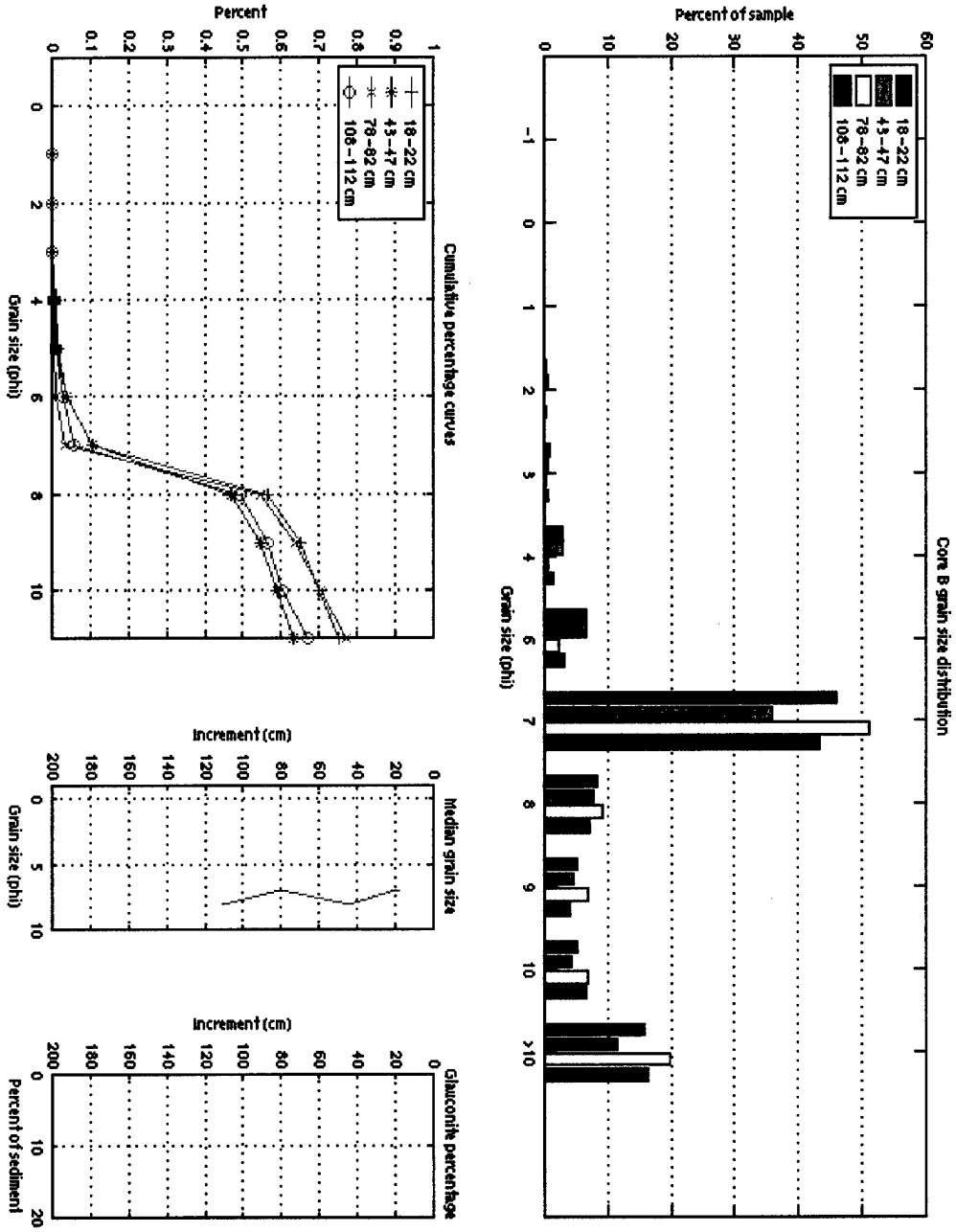

Figure 3.10. Grain size distribution, cumulative percentage curves, median grain size profile, and glauconite percentage profile for Core B, collected at 2285 m.

for the entire length of the core. Core B shows a slight coarsening upwards from 108 cm to 78 cm (from 8φ to 7φ), then fines upwards from 78 cm to 43 cm (from 7φ to 8φ), and coarsens from 43 cm to 18 cm (from 8φ to 7φ). Only trace amounts of glauconite were found within the sediment.

3. Core C

Core C was collected at a depth of 1948 m. Figure 3.11 contains the grain size distribution, cumulative percentage curves, median grain size profile, and glauconite percentage profile for Core C. Core C is very similar to Cores A and B in terms of sediment grain size and distribution. The histogram of grain size distribution for Core C shows that the dominant grain size for all samples is 7φ, which makes up 35-45% of the total sediment in each sample. The grain size distributions and cumulative percentage curves show that the majority of the sediment in Cores A-C is 7φ or greater. In addition, a significant percentage (15-20%) of the sediment is finer than 10φ, indicating that clay-size particles have a strong presence in this core. The uppermost sample of Core C shows a slightly larger percentage of coarser sediment (4φ-6φ) than in the remaining samples from the core, but this is not seen in the median grain size graph due to the high percentage of sediment at 7φ. Core C shows a slight coarsening upwards from 123 cm to 78 cm (from 8φ to 7φ), then maintains the same median grain size (7φ) for the rest of the core. Only trace amounts of glauconite were found within the sediment.

4. Core D

Core D was collected at a depth of 1672 m. Figure 3.12 contains the grain size distribution, cumulative percentage curves, median grain size profile, and glauconite percentage profile for Core D. Core D is similar to Cores A-C, but some distinctive characteristics exist within the sediment that differs from Cores A-C. From the grain size

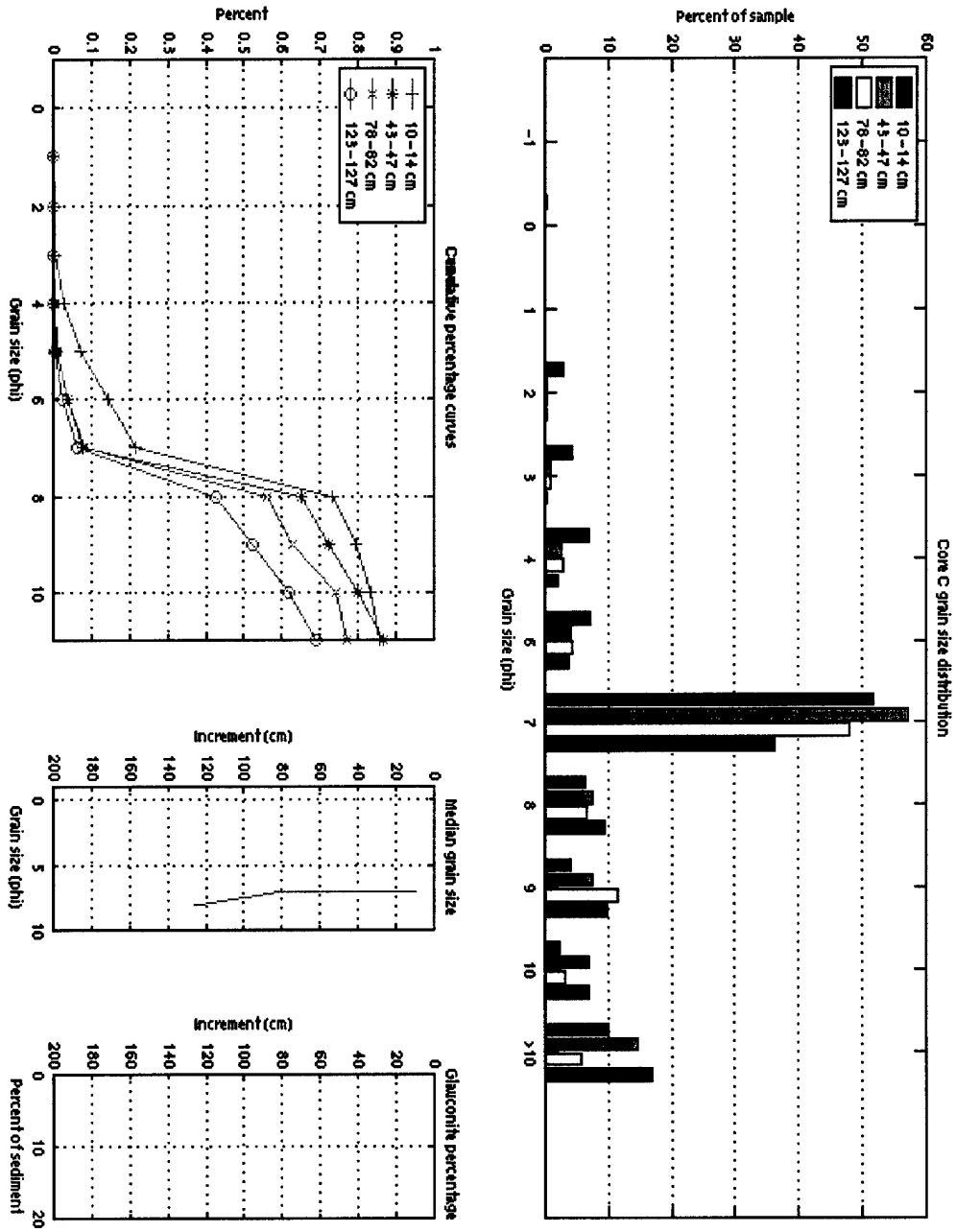

Figure 3.11. Grain size distribution, cumulative percentage curves, median grain size profile, and glauconite percentage profile for Core C, collected at a depth of 1948 m.

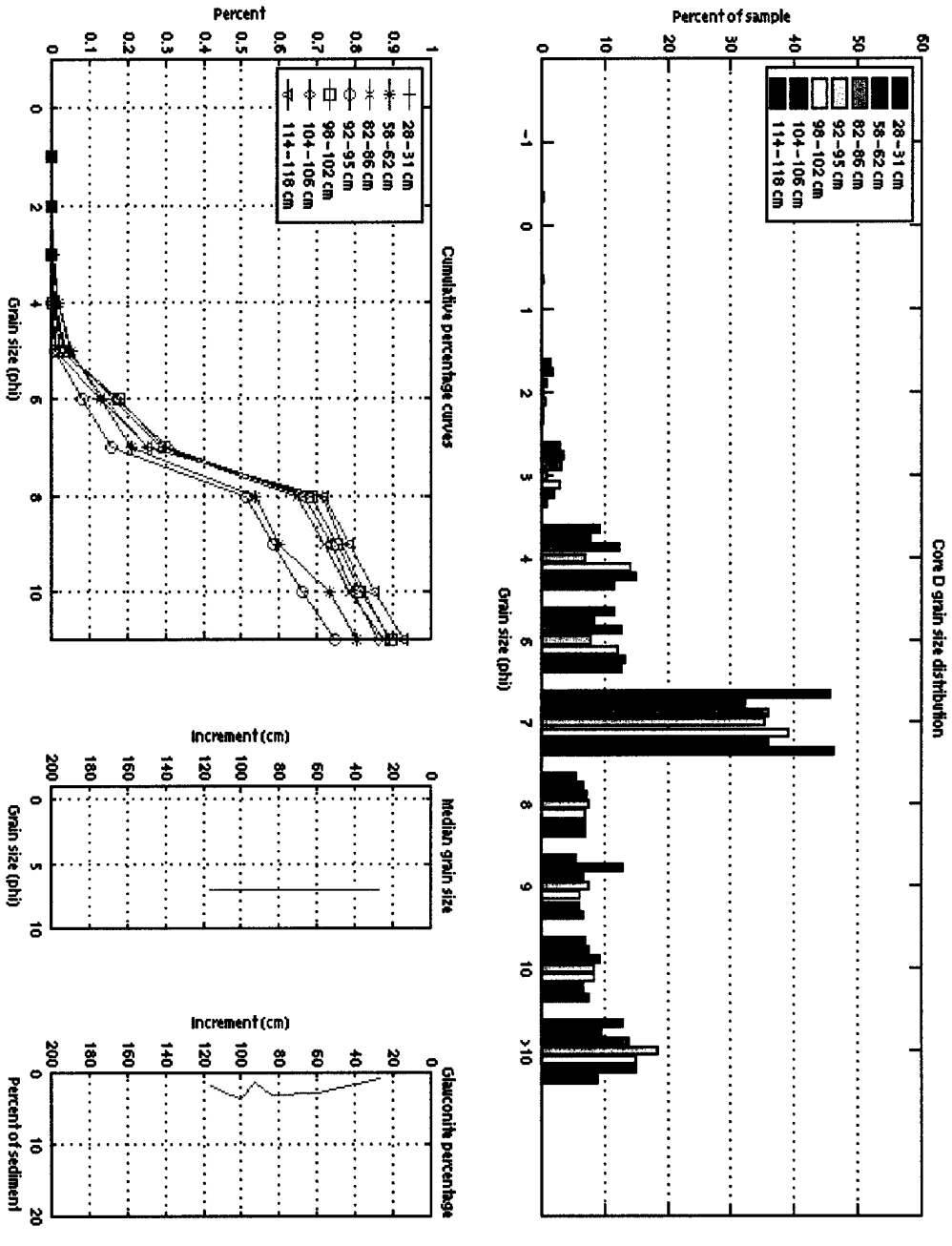

Figure 3.12. Grain size distribution, cumulative percentage curves, median grain size profile, and glauconite percentage profile for Core D, collected at a depth of 1672 m.

distribution graphs, Core D shows that a larger percentage of the sediment (10-15%) for all samples are coarser than the 7φ benchmark found in Cores A-C. The cumulative percentage curves also show this, as the slope of the curves between 3φ and 7φ is not as steep as found in Cores A-C. This increase in coarser sediment is also reflected in the increase in glauconite within the core. The dominant grain size of 7φ still accounts for 35-45% of the total sediment for all samples. Like Cores A-C, a significant percentage of the sediment are finer than 10φ, indicating the strong presence of clay-sized particles intermixed with the coarser silts seen in the distribution. Core D maintains the same median grain size (7φ) throughout the core.

5. Core E

Core E was collected at a depth of 1435 m. Figure 3.13 contains the grain size distribution, cumulative percentage curves, median grain size profile, and glauconite percentage profile for Core E. Core E is very similar to Core D in terms of dominant grain size and sediment distribution. The grain size distribution graph shows that Core E has a significantly larger percentage (10-15%) of sediment coarser than 7φ. The cumulative percentage curves also show this, as the slope of the curve between 3φ and 7φ is not as steep as found in Cores A-C. This increase in coarser sediment is reflected as well in the increase in glauconite within the core. The dominant grain size of 7φ still accounts for 35-50% of the total sediment for all samples. In addition, a significant percentage of the sediment are finer than 10φ, indicating the strong presence of clay-sized particles intermixed with the coarser silts seen in the distribution. Core E maintains the same median grain size (7φ) throughout the core.

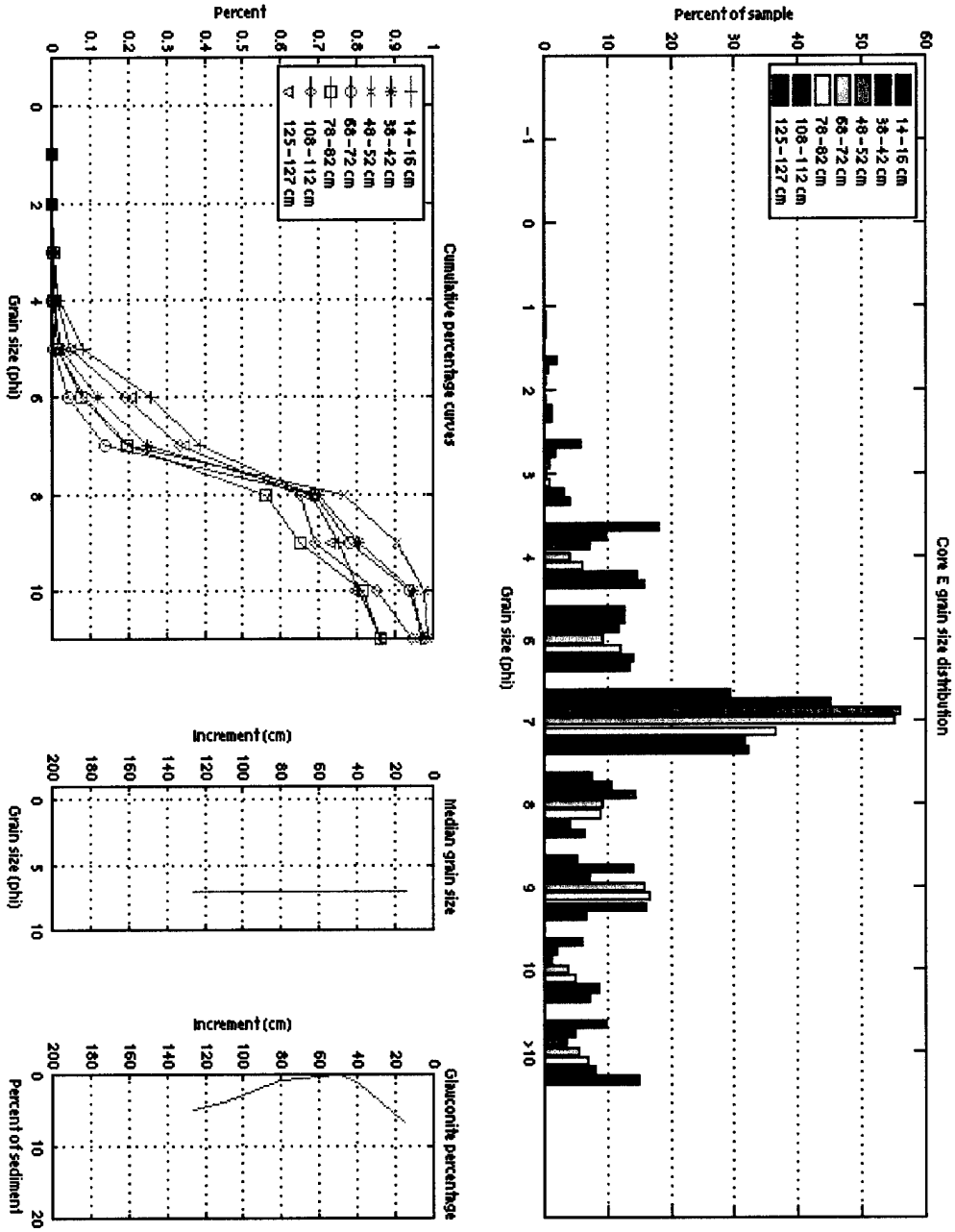

Figure 3.13. Grain size distribution, cumulative percentage curves, median grain size profile, and glauconite percentage profile for Core E, collected at a depth of 1435 m.

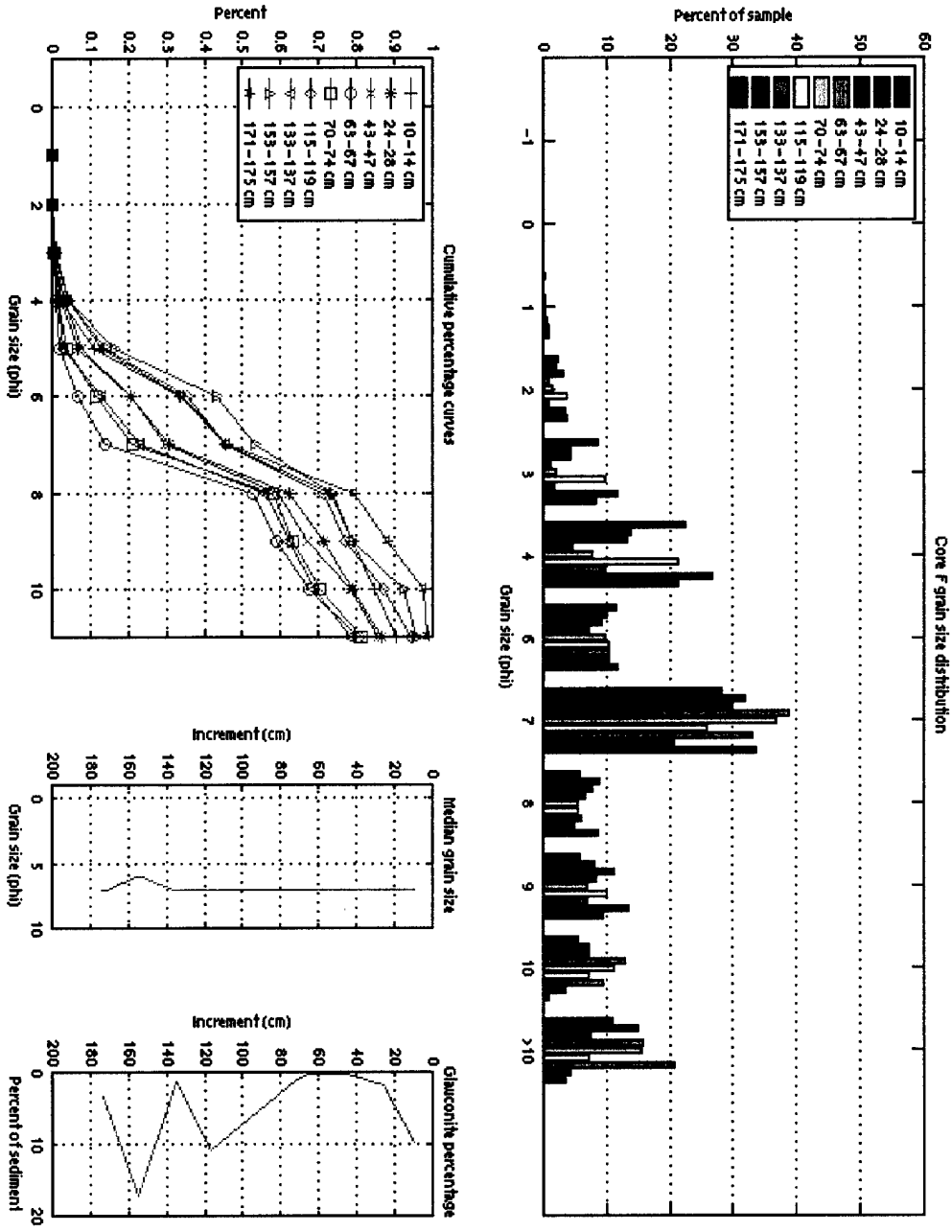

Figure 3.14. Grain size distribution, cumulative percentage curves, median grain size profile, and glauconite percentage profile for Core F, collected at a depth of 1232 m.

6. Core F

Core F was collected at a depth of 1232 m. Figure 3.14 contains the grain size distribution, cumulative percentage curves, median grain size profile, and glauconite percentage profile for Core F. Core F is very similar to Cores D and E in terms of dominant grain size and sediment distribution. From the grain size distribution graph, Core F shows that a larger percentage of the sediment (10-15%) are coarser than 7φ, as seen in Cores A-C. The cumulative percentage curves also show this, as the slope of the curves between 3φ and 7φ is not as steep as found in Cores A-C. The increasing percentage of glauconite within the core is the main cause for the coarsening of the sediment. The dominant grain size of 7φ still accounts for 30-45% of the total sediment for all samples, with the exception of the sample taken at 153 cm, which has a coarser dominant grain size of 6φ (and a high percentage of glauconite). In addition, a significant percentage of the sediment are finer than 10φ, indicating the strong presence of clay-sized particles intermixed with the coarser silts seen in the distribution. Core F shows a slight coarsening upwards from 171 cm to 153 cm (from 7φ to 6φ), but then fines back to the dominant median grain size (7φ) for the rest of the core.

7. Core G

Core G was collected at a depth of 1341 m. Figure 3.15 contains the grain size distribution, cumulative percentage curves, median grain size profile, and glauconite percentage profile for Core G. Core G shows a markedly different picture from the previously discussed cores, exhibiting a much coarser dominant grain size of 3φ. This is a difference of almost 0.25mm in grain size between previously discussed cores and Core G, and is due to the high percentage of glauconite within the sediment. The grain size distribution and cumulative percentage curves show that the majority of sediment for all

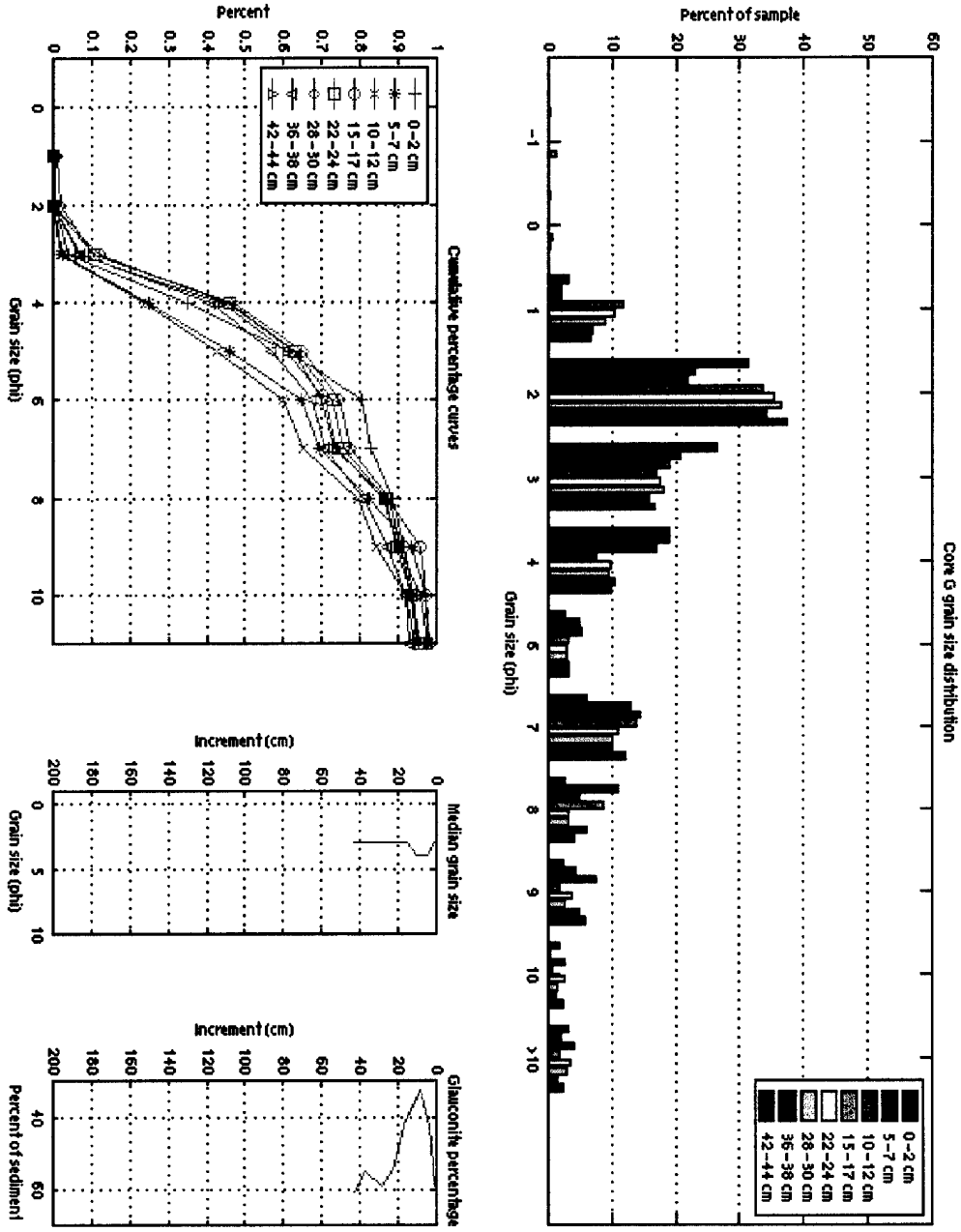

Figure 3.15. Grain size distribution, cumulative percentage curves, median grain size profile, and glauconite percentage profile for Core G, collected at a depth of 1341 m.

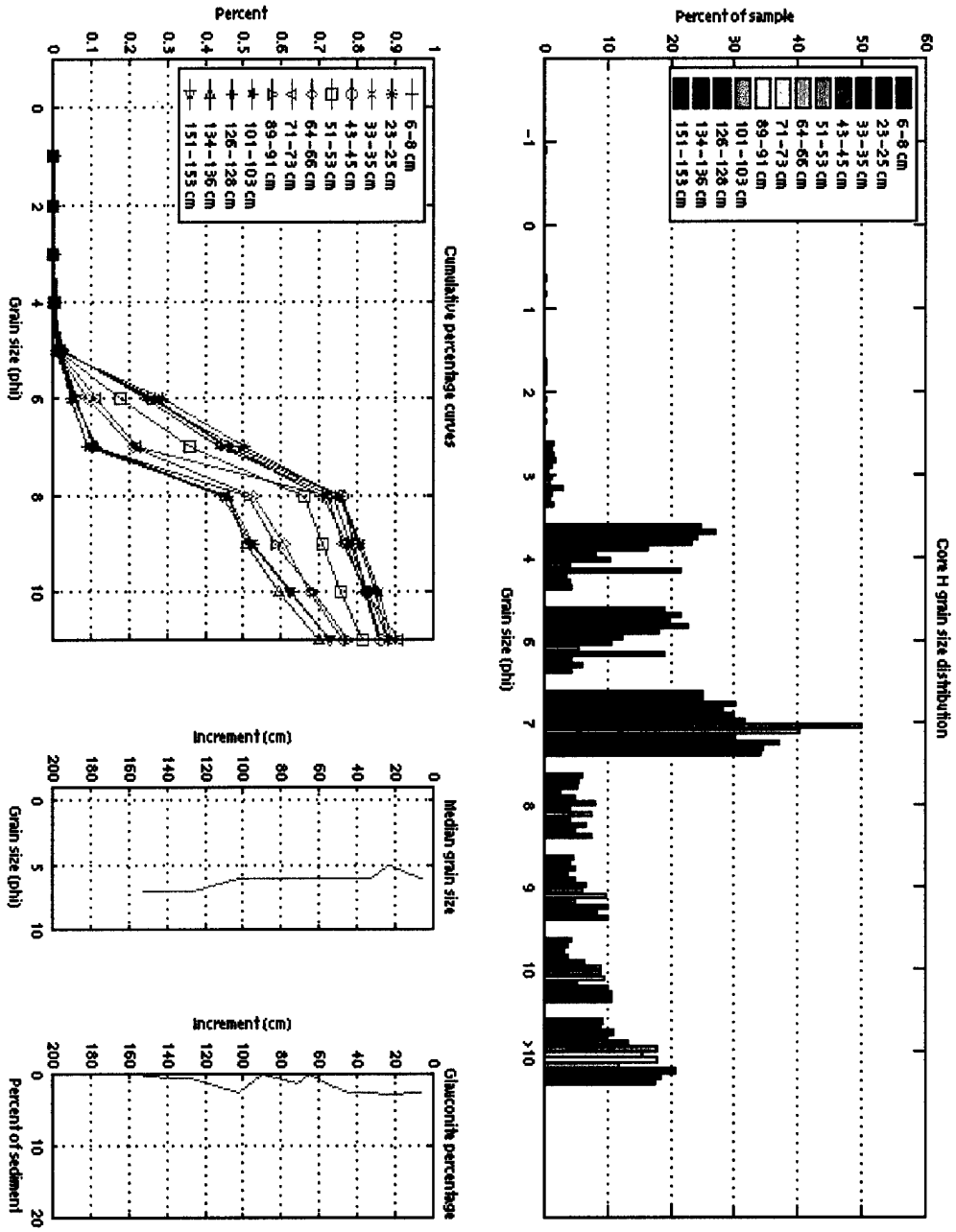

Figure 3.16. Grain size distribution, cumulative percentage curves, median grain size profile, and glauconite percentage profile for Core H, collected at a depth of 851.3 m.

samples is between 2φ and 8φ, indicating that Core G does not contain as large a portion of very fine sediment as do Cores A-F. The upper 15 cm of the core do contain a significant percentage (20-30%) of sediment finer than 3φ, but below 15 cm the majority of the sediment (40-45%) is 3φ. The median grain size graph for Core G shows a slight fining upwards from 15 cm to 10 cm (from 3φ to 4φ), and a slight coarsening upwards from 5 cm to the surface of the core (from 4φ to 3φ).

8. Core H

Core H was collected at a depth of 851.3 m. Figure 3.16 contains the grain size distribution, cumulative percentage curves, median grain size profile, and glauconite percentage profile for Core H. Core H is very similar to Cores D-F in terms of sediment distribution, but has some slight variations in dominant grain size. From the grain size distribution graph, Core H shows a significant percentage of the sediment that is coarser than the 7φ, particularly in the upper half of the core. This coincides with the increase in the percentage of glauconite within the core. The cumulative percentage curves also show this, as the slope of the curves between 3φ and 7φ is not as steep as found in Cores A-C. The dominant grain size in the lower third of the core is 7φ, but as the percentage of sediment coarser than 7φ increases, the median grain size begins to likewise coarsen to 6φ for the rest of the core, due to the presence of glauconite. The exception to this is the sediment near 20 cm, which have a dominant grain size of 5φ. In addition, a significant percentage of the sediment is finer than 10φ, indicating the strong presence of clay-sized particles intermixed with the coarser silts seen in the distribution. Core H shows a slight coarsening from 126 cm to 101 cm (from 7φ to 6φ) and a slight coarsening from 33 cm to 23 cm (from 6φ to 5φ), but then fines slightly upward from 23 cm to 6 cm (from 5φ to 6φ).

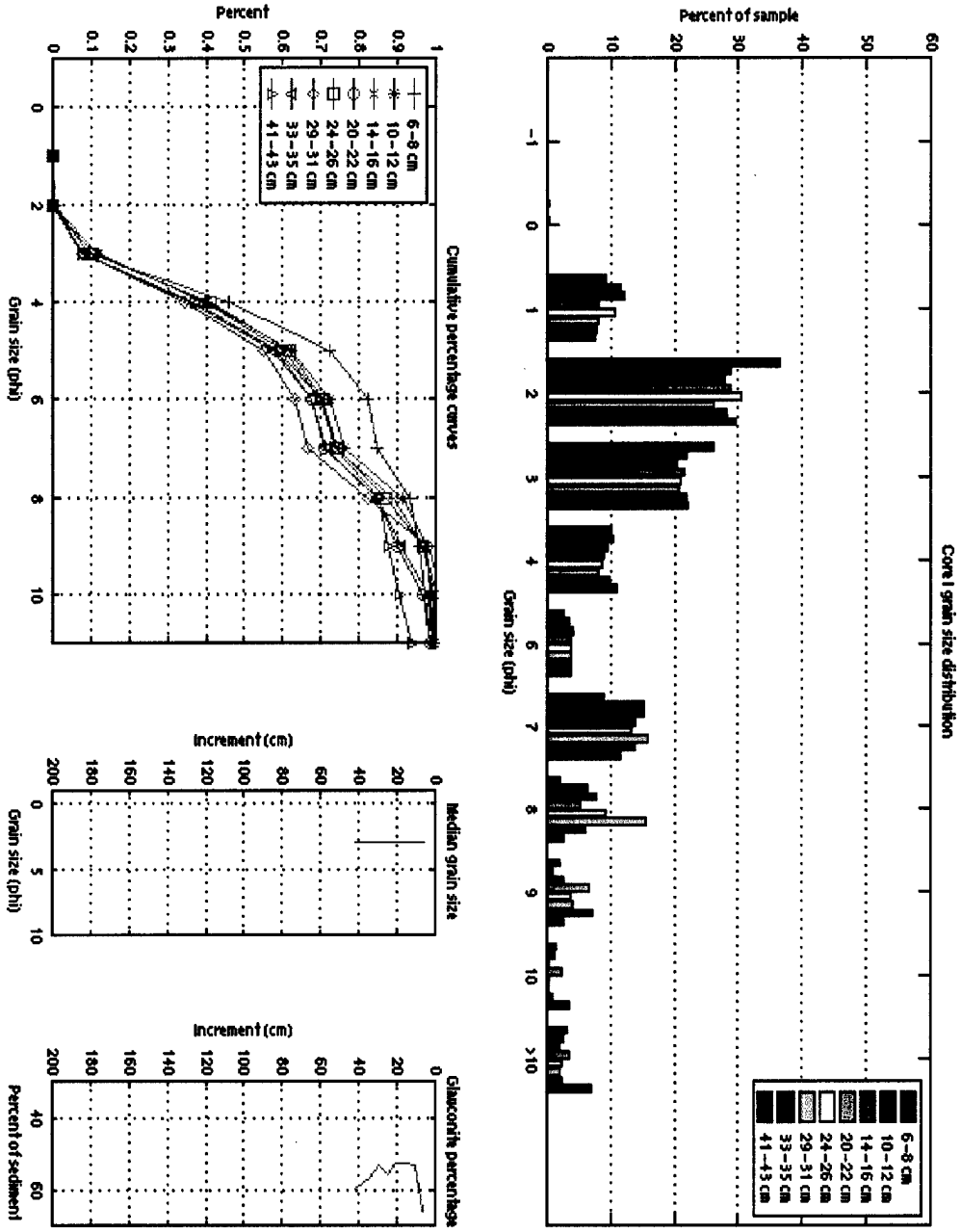

Figure 3.17. Grain size distribution, cumulative percentage curves, median grain size profile, and glauconite percentage profile for Core I, collected at a depth of 1128 m.

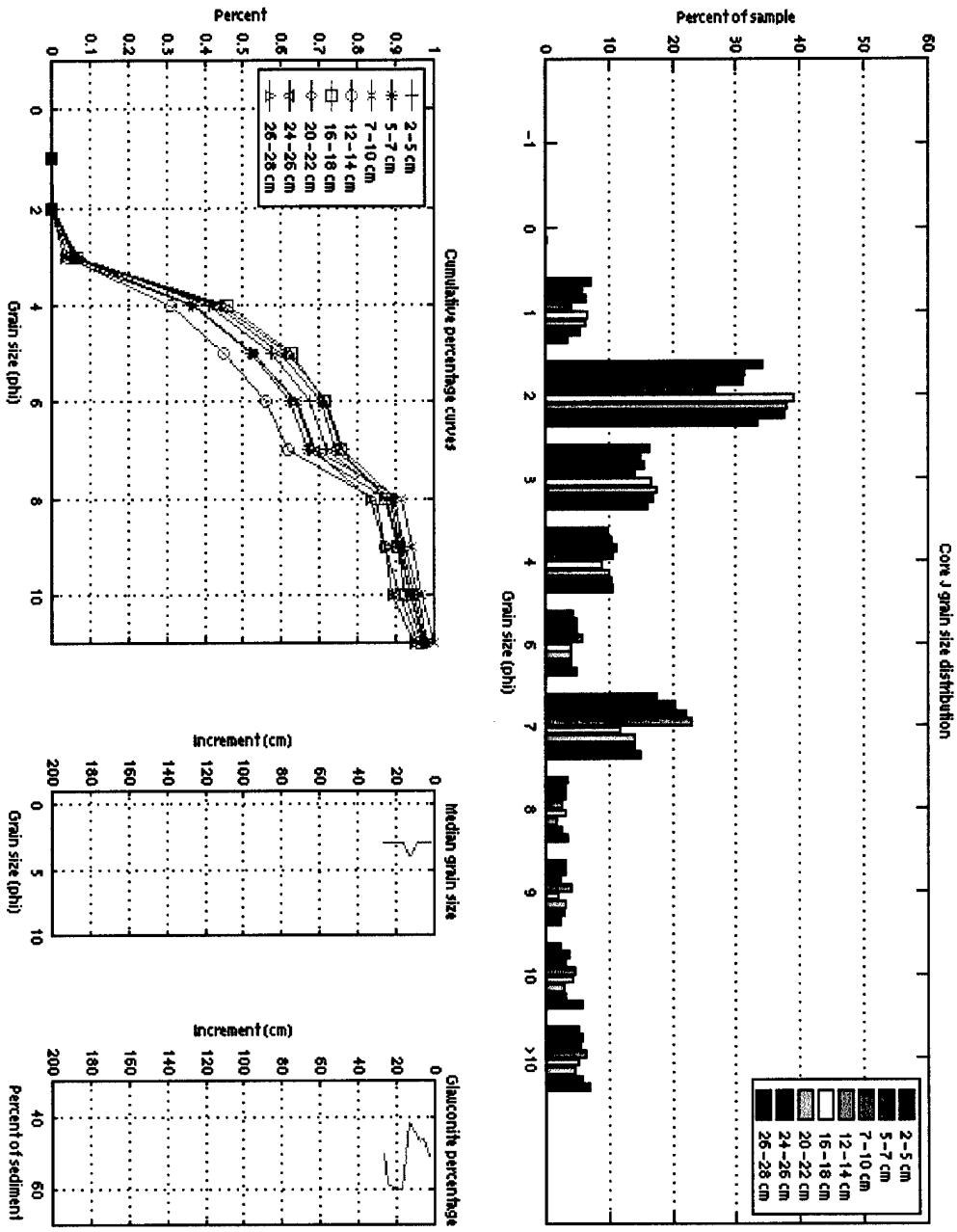

Figure 3.18. Grain size distribution, cumulative percentage curves, median grain size profile, and glauconite percentage profile for Core J, collected at a depth of 1157 m.

9. Core I

Core I was collected at a depth of 1128 m. Figure 3.17 contains the grain size distribution, cumulative percentage curves, median grain size profile, and glauconite percentage profile for Core I. Core I is very similar to Core G in terms of dominant grain size and sediment distribution, and also shows a high percentage of glauconite within the sediment. The grain size distribution and cumulative percentage curves show that the majority of sediment for all samples is between 2φ and 8φ, indicating that Core I does not contain as large a portion of very fine sediment as do Cores A-F and H. Similar to the upper 15 cm of Core G, Core I contains a significant percentage of sediment (20-30%) finer than 3φ, but maintains this percentage throughout the core. Core I maintains a uniform median grain size (3φ) throughout the core.

10. Core J

Core J was collected at a depth of 1157 m. Figure 3.18 contains the grain size distribution, cumulative percentage curves, median grain size profile, and glauconite percentage profile for Core J. Core J is very similar Core I in terms of sediment distribution, dominant grain sizes, and glauconite percentage. The grain size distribution and cumulative percentage curves show that the majority of sediment for all samples is between 2φ and 8φ, indicating that Core J does not contain as large a portion of very fine sediment as do Cores A-F and H. Like Core I, Core J shows throughout the core that a significant percentage (15-20%) of the sediment is finer than the median grain size of 3φ. Core J shows a slight fining upwards from 16 cm to 12 cm (from 3φ to 4φ), but then coarsens slightly from 12 cm to 7 cm (from 4φ to 3φ).

11. Core K

Core K was collected at a depth of 855 m. Figure 3.19 contains the grain size distribution, cumulative percentage curves, median grain size profile, and glauconite percentage profile for Core K. What little information can be derived from Core K shows that the sediment are similar to those seen in Cores G, I, and J, and contain a high percentage of glauconite. The dominant grain size is 3φ, and very little percentage of the sediment is finer than 7φ. The sediment in Core K appears to have a moderate fining upwards sequence from 4 cm to 1 cm (from 2φ to 4φ).

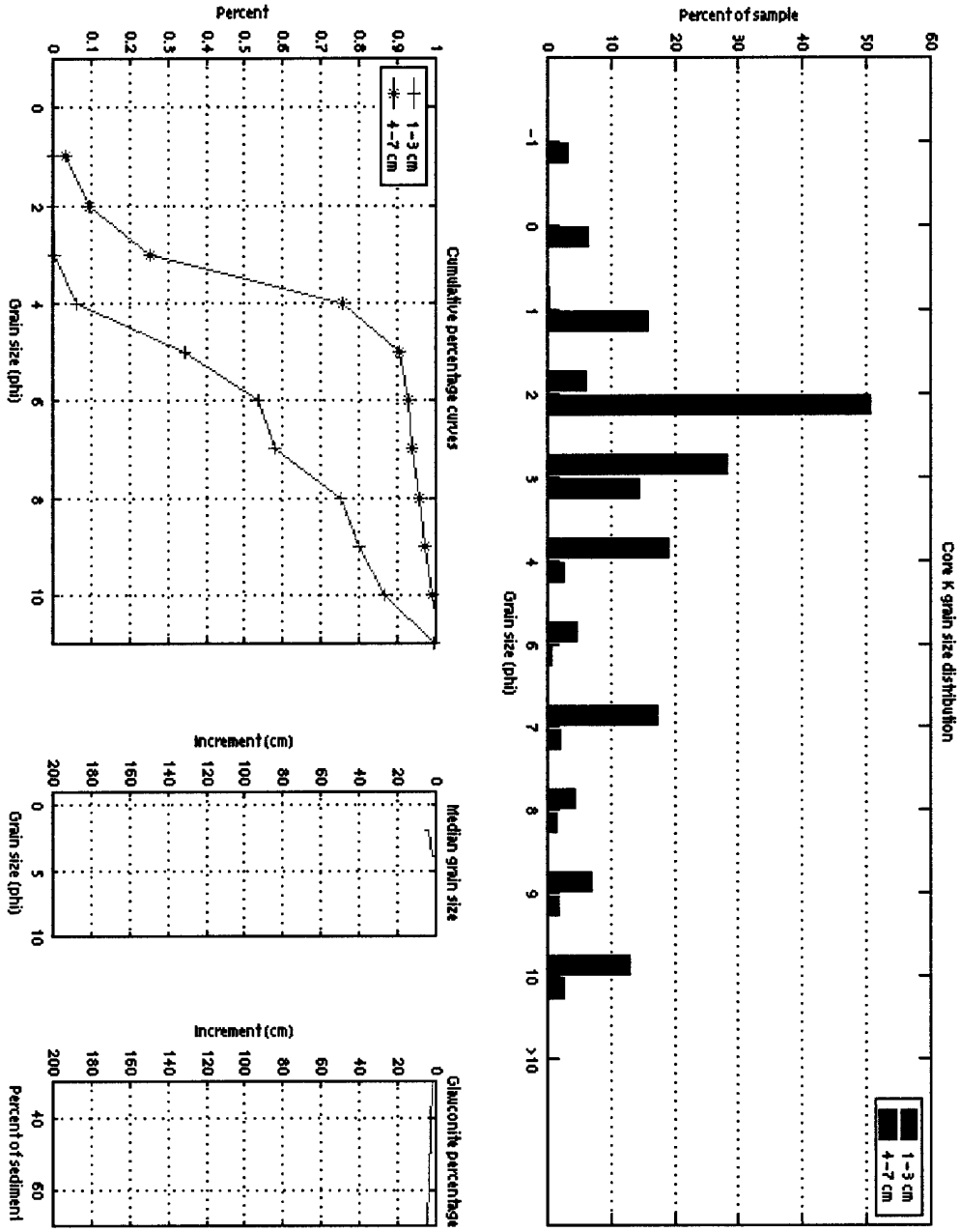

Figure 3.19. Grain size distribution, cumulative percentage curves, median grain size profile, and glauconite percentage profile for Core K, collected at a depth of 855 m.

IV. DISCUSSION

A. RELATIONSHIP OF SEDIMENT AND GEOMORPHOLOGY

From the description of the physical properties of the cores and the grain-size analysis, several relationships can be established with respect to the locations of the cores (Figure 2.1). In addition, the cores can also be placed into three distinct groups (Figure 4.1).

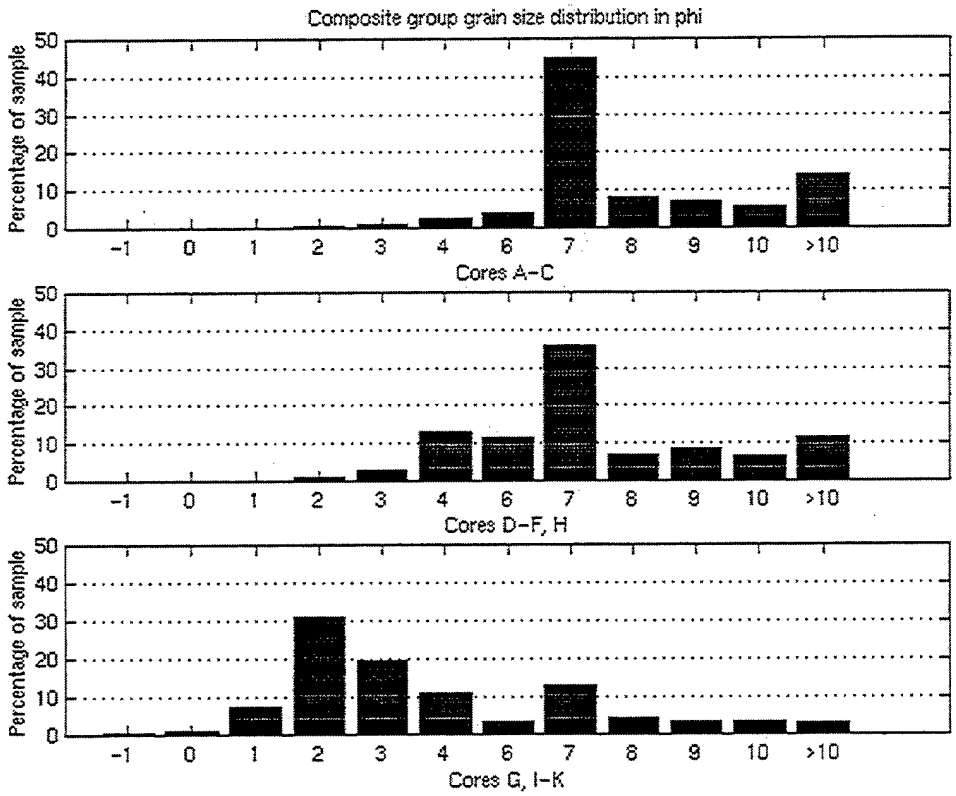

Figure 4.1. Composite grain-size distribution graphs for Cores A-C (2553-1948 m), D-F (1672-1232 m) and H (851.3 m), and G (1341 m) and I-K (1128 m, 1157 m, and 855 m, respectively).

Cores A-C are the deepest cores, taken on the lower western part of Sur slope (2553-1948 m) (Figure 1.5), and exhibit a very distinct median grain size of 7φ, with very little significant changes seen throughout the sediment distribution of each core (Figures 3.9-3.11). The majority of the sediment in Cores A-C is 7φ or greater, with a significant percentage of sediment finer than 10φ (Figure 4.1). In addition, the upper most 10-20 cm of each core is composed of poorly to moderately consolidated sediment, as opposed to the other cores, where the sediment is well consolidated (Figure 3.5). The amount of sediment that is poorly to moderately consolidated also decreases as one moves up the slope of Sur Ridge; Core A has approximately 19 cm of poorly to moderately consolidated sediment, whereas Core C has less than 10 cm. Of significance is the fact that, while these cores were taken from an area exposed to repeated slumps and landslides, no visible scours or layering of different sediment were found. This may indicate that the cores were taken from an area that had no landslides. Another possible explanation is that the cores were taken in an area exposed to landslides, but that a more recent sediment layer has covered the landslides. Thus the landslide surface had "healed" sufficiently such that the gravity cores did not penetrate through the "healed" sediment layer on top of the landslide.

The second group of cores is comprised of Cores D-F and Core H. Cores D-F (1672-1232 m) are from the middle and upper western part of Sur slope, while Core H (851.3 m) is from the upper continental slope to the east of Sur Ridge (Figure 1.5). These cores exhibit characteristics similar to Cores A-C, but also have some major differences. The dominant grain size is 7φ, and there is a significant percentage of the sediment in the

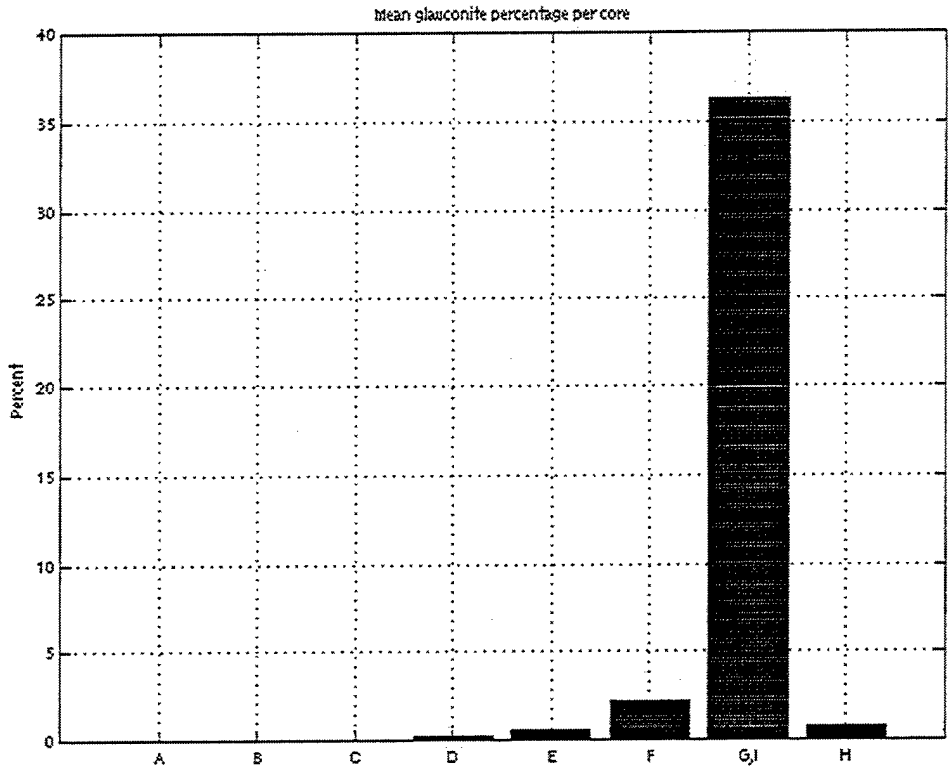

Figure 4.2. Graph showing the percentage of sediment composed of glauconite per core.

cores that is finer than 10φ (Figure 4.1). However, there is a significant coarsening of the sediment between 4 and 6φ that is not seen in Cores A-C, which is most likely due to an increased presence of glauconite in the sediment, as particularly evidenced in Cores F (Figure 3.7) and H, and seen in Figure 4.2.

The third group of cores is comprised of Core G and Cores I-K. Cores G (1341 m) and I (1128 m) are from the trough between Sur Ridge and the upper continental slope, and Core J (1157 m) is from the upper western slope of Sur Ridge, at the same

approximate depth as Core I (Figure 1.5). Core K (855 m) is from the upper slope of Surveyor Knoll, approximately 5 km to the SE of Sur Ridge. These cores are dominated by a very high percentage of glauconite and foraminifera tests (Figure 4.2). Unlike the first two groups, the median grain size for this group of cores is 3φ. In addition, this group lacks a significant percentage of sediment finer than 10φ; the majority of all sediment in these cores is 4φ or less (Figure 4.1). Several bands of intersititial clay matrix were present (Figure 3.6), but were overshadowed by the dense concentrations of glauconite and foraminifera. Also of note is the fact that Cores G and I show bands of moderate to high concentrations of foraminifera and occasional parts of sponges, and Core J, on the western slope of Sur Ridge, shows similar, less concentrated bands.

From this grouping of cores, several relationships can be made. Cores A-C show very little change in grain size distribution, indicating that the lower part of the western slope of Sur Ridge contains mostly homogenous, fine-grained sediment. These cores were taken from sediment deposited in an area where slumps and landslides occurred in the past along the western lower half of Sur slope (Figure 1.5). This is also an area where the slope is steepest and is the furthest away from land compared to the other areas sampled. Moving up the slope to the east, the sediment is still mostly homogeneous and fine-grained, but also shows an increase in coarser sediment, as seen in Cores D-F (Figure 4.1, 4.2). This is in an area where the sea floor is more gentle and lies an intermediate distance from land, compared to other areas sampled (Figure 1.5). Along the upper western slope of Sur Ridge, and within the trough on the eastern slope of Sur Ridge, the sediment is very coarse and shows very little fine-grained material, as seen in Core G and Cores I-K. This is an area of more diverse and higher relief, and is also

closer to land than other areas sampled (Figure 1.5). Of particular interest is the fact that Cores I and J are on opposite sides of Sur Ridge, but are at the same relative depth (1128 m and 1157 m, respectively) and show the same grain size distribution. Moving further east, onto the upper continental slope, the sediment has the same characteristics of the middle western part of Sur slope.

Also noteworthy is the presence of glauconite throughout the cores, particularly in the cores found in the near vicinity of Sur Ridge (Cores F-K). While glauconite is typically formed on shallow continental shelves (100-300 m), the Oxygen Minimum Zone (OMZ) near Point Sur have shown that glauconitic sediment is found in depths of water up to 600 m (Vercoutere, et al., 1987). Yet Cores F-K were taken at depths ranging from 850 m to 1340 m. This depth inconsistency has several possible explanations. The glauconite found in the cores could have formed on the continental shelf, and was then transported to the vicinity of Sur Ridge. Yet the glauconite appears to be of a relatively advanced development, bordering on an evolved texture, indicating it has been in an environment favorable to glauconization for a lengthy period of time. A possible explanation for the presence of the glauconite is vertical movement of the central California margin due to tectonic activity. This explanation for the location of the glauconite seems the most plausible, based on the abundant evidence of tectonic activity in the area. At some point in geologic history, due to tectonism, the sea level along the central California margin was 200-300 m lower than the present sea level (i.e. along the upper continental slope, instead of the continental shelf). This lower sea level would equate to a lower OMZ, and thus would provide the geochemical microenvironment needed to form the glauconite seen within the cores of this study. More recent tectonic

activity and sea level rise have caused the region to subside to its present depth, and changed the depositional environment, bringing in fine-grained clays and silts and creating the type of sediment found in cores F and H.

As mentioned before, the presence of the poleward flowing trough jet along the eastern side of Sur Ridge most likely plays a significant role in the sedimentation and geomorphology of the surrounding area. Prior to the formation of Sur Ridge, the sediment distribution along the middle and upper part of Sur slope (from Core F to Core H) was probably uniform. The formation of Sur Ridge due to faulting would certainly effect the flow of bottom waters along Sur slope. The projection of the ridge above the slope could have served to trap the waters flowing down the slope, causing an increase in alongshore pressure gradients and stronger flow. In addition, the fault would also have formed an associated zone of preferential erosion directly to the east of the ridge, which would be more susceptible to erosion. As the finer-grained sediment was winnowed, the trough could become deeper, and thus help to intensify the bottom currents further. This type of erosion would lead to the formation of a lag deposit, with a layer of coarse-grained, concentrated glauconite at the top of the sediment layer. Cores G and I both had such layers. Eventually, the intensity of the trough jet would come to an equilibrium with the sediment within the trough, since there would be no more fine-grained material to be winnowed. Erosion would then stop.

Also of note is that a corresponding current was not seen on the western side of Sur Ridge, indicating that this intensified bottom current is unique to the trough. However, the grain-size analysis from Core J is very similar to the grain-size analyses of Cores G and I, indicating that the depositional environment for the sediment found in

Core J is very similar to the depositional environment for the sediment found in Cores G and I. This would indicate that a stronger current might also exist along the upper western slope of Sur Ridge, or that a similar current existed in the past.

From the sediment characteristics and from the results of the Carbon-14 dating (Figure 3.8), several ideas can be obtained regarding the sedimentation regimes of the three groups of cores. The sediment along the lower part of Sur slope has an extremely low sedimentation rate based on the age of the sediments analyzed near the tops of Cores A and B. This would indicate that the lower part of Sur slope is not currently experiencing deposition of sediment, or quite possibly is undergoing a very slow rate of erosion. The same type of depositional environment likely exists for the middle and upper parts of Sur slope, as well as the upper slope to the east of Sur Ridge. It is very clear, however, that the sedimentation regime that created the sediment within the trough is erosional in nature, most likely due to strong currents. Likewise the sedimentation regime along the upper western face of Sur Ridge and the north face of Surveyor Knoll indicate an erosional sedimentation regime that is currently in place but not observed, or that existed in the past.

B. RELATIONSHIP OF SEDIMENT AND ACOUSTICS

From the analysis of the acoustic properties of each core in Chapter III, the cores can be grouped into the same three groups as discussed earlier in this chapter. Figure 4.3 shows composite profiles of compressional wave velocity, wet bulk density, magnetic susceptibility, glauconite percentage, and median grain size for the three groups of cores.

Cores A-C all show very similar characteristics in terms of velocity, density, glauconite percentage, and magnetic susceptibility profiles (Figure 4.3). The upper parts

of all three cores are composed of poorly to moderately consolidated sediment; but deeper into the core the sediment became well-consolidated. This is seen in the relatively fast velocities at the surface of the cores, which then steadily decrease as the density increases due to consolidation and dewatering. Once into the consolidated part of the cores, the density and velocity profiles level out. The magnetic anomalies are almost negligible for Cores A and B, and is only very slightly positive for Core C, indicating a relative lack of glauconite within the sediment.

Cores D-F and Core H may also be grouped together, based on velocity, density, glauconite percentage, and magnetic susceptibility profiles (Figure 4.3). From Core D to Core F, a steady overall increase in density is seen, with a corresponding increase in the positive magnetic anomaly, most likely due to the steady increase in the percentage of glauconite in the sediment. Cores D and E also show a slightly less consolidated upper layer not seen in the physical analysis, but seen in the form of a relatively fast velocity at the surface, which then declines rapidly in the first 40 cm of sediment. A corresponding density increase likely means a consolidation of the sediment with resulting dewatering. What becomes interesting to note is that for Cores D-F and Core H, below the upper part of the cores, the density and velocity profiles begin to mirror one another. This means that, when density increases, velocity increases as well. This would indicate a high enough degree of consolidation within the sediment such that the density of the sediment, not the pore water, would control the compressional wave velocity. In the case of Cores F and H, the magnetic susceptibility profiles also tend to mirror the density and velocity profiles. A possible explanation for this is that the fluctuating magnetic anomaly could

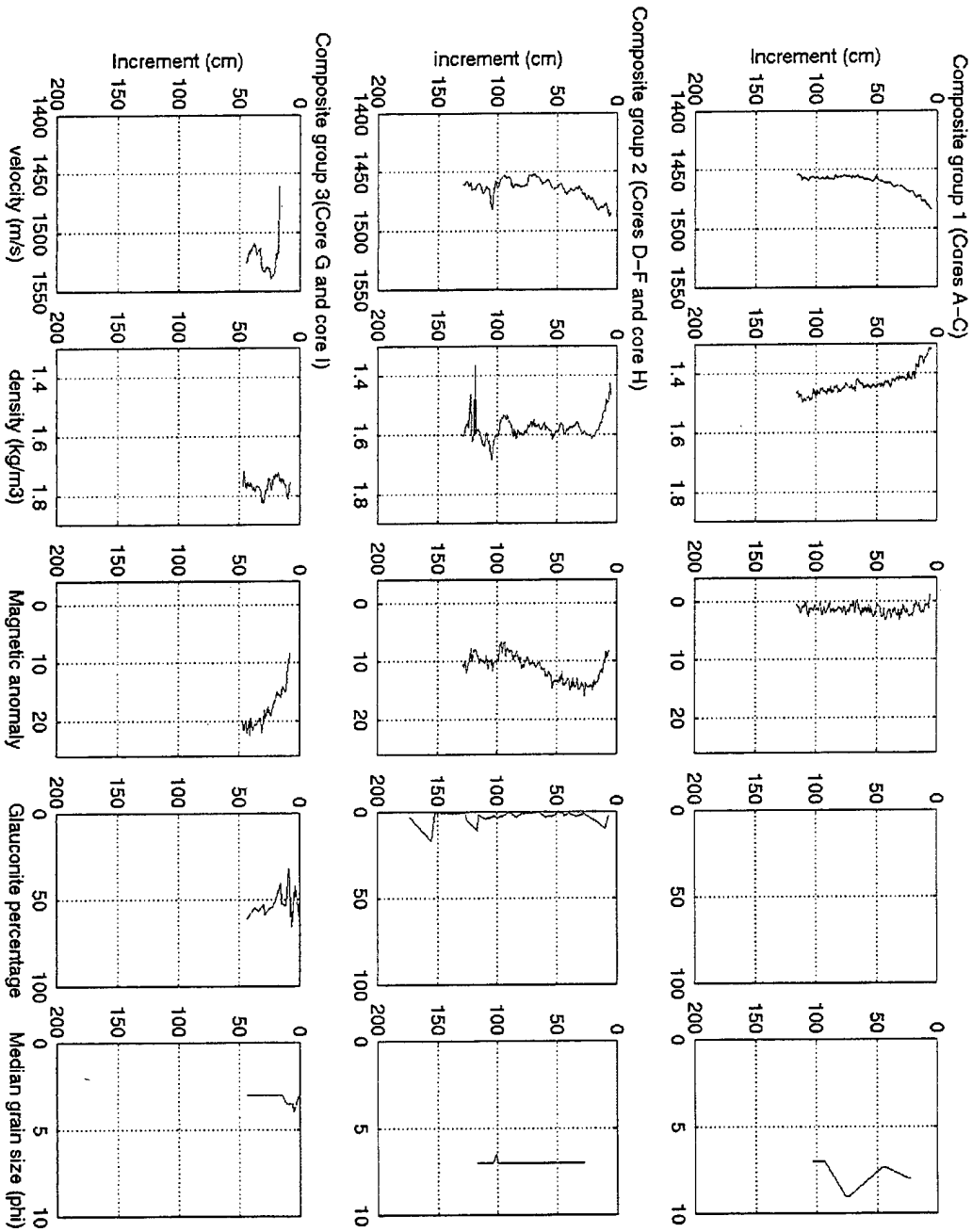

Figure 4.3. Composite profiles of compressional wave velocity, wet bulk density, magnetic susceptibility, glauconite percentage, and median grain size for Cores A-C, D-F and H, and G-I.

be due to localized concentrations of glauconite, which in turn increase the density, but also increase the velocity due to the coarseness of the sediment.

Cores G and I are also very similar in terms of velocity, density, and magnetic susceptibility, and glauconite percentage profiles (Figure 4.3). Both cores show substantially higher densities and velocities than the other cores. This is due to the very high concentration of glauconite in both cores, as well as the coarseness of the sediment. Also of interest is that, in Core G, the velocity decreases with depth, with a corresponding increase in density, however the positive magnetic anomaly is also steadily increasing. This most likely results from the consolidation and dewatering of the sediment with depth.

Based on the relationships seen between the sediment and the profiles obtained from the acoustic analysis (after correcting to *in-situ* values), it can be seen that the velocity and density of all cores is affected by the consolidation of the sediment, as well as the composition. All three groups of cores exhibit faster velocities and lower densities in less-consolidated areas. Moving from the lower part of Sur slope up to the western face of Sur Ridge, the percentage of glauconite within the sediment continually increases (Figure 4.2). This is reflected in the positive magnetic anomaly, as well as in an increase in the compressional wave velocity, most likely due to the coarsening of the sediment. In addition, as glauconite percentages increase, the density will also increase. Thus in some areas both the density and velocity will increase due to the strong presence of glauconite, whereas in other locations where glauconite percentages are low the increase in velocity is countered by an increase in density as the sediment consolidates, reducing pore waters and thus reducing the velocity.

C. RELATIONSHIP OF ACOUSTIC PROPERTIES OF SEDIMENT WITH RESPECT TO LOCATION

From the discussion of acoustic properties of sediment in Chapter III and the discussion above about the acoustic characteristics of the sediment of each core, it is worthwhile to examine the spatial relationships between each core. Figure 4.4 shows the mean values of the compressional wave velocity, wet bulk density, sediment porosity, and glauconite percentage for each core. Shown next to each other, these values provide a useful tool in understanding the acoustic properties of the sediment in each core and how the properties trend with respect to the spatial relationships of the cores.

Comparing the curves in Figure 4.4, it can be seen that the mean compressional wave velocity from the lower Sur slope to the western face of Sur Ridge (from Core A to Core F) shows slight fluctuations, but increases overall. This agrees with the mean wet bulk density, which also increases steadily moving up the slope. The density increase also leads to a corresponding decrease in the mean porosity upslope (from Core A to Core F), due to compression and dewatering of the sediment. In addition, the concentration of glauconite within the cores increases in the upslope direction, which provides additional support for both the compressional wave velocity and density increases upslope. Moving east, from the upper western face of Sur Ridge, over Sur Ridge, and into the trough (from Core F to Cores G and I), the effects of the coarser grain size and high percentage of glauconite are seen. The mean compressional wave velocity shows a rapid increase due to the coarser (7φ) grain-size, while the mean wet bulk density also shows a significant increase due to the coarser grain-size and dominance of glauconite. The mean porosity, corresponding to the increase in density, shows a

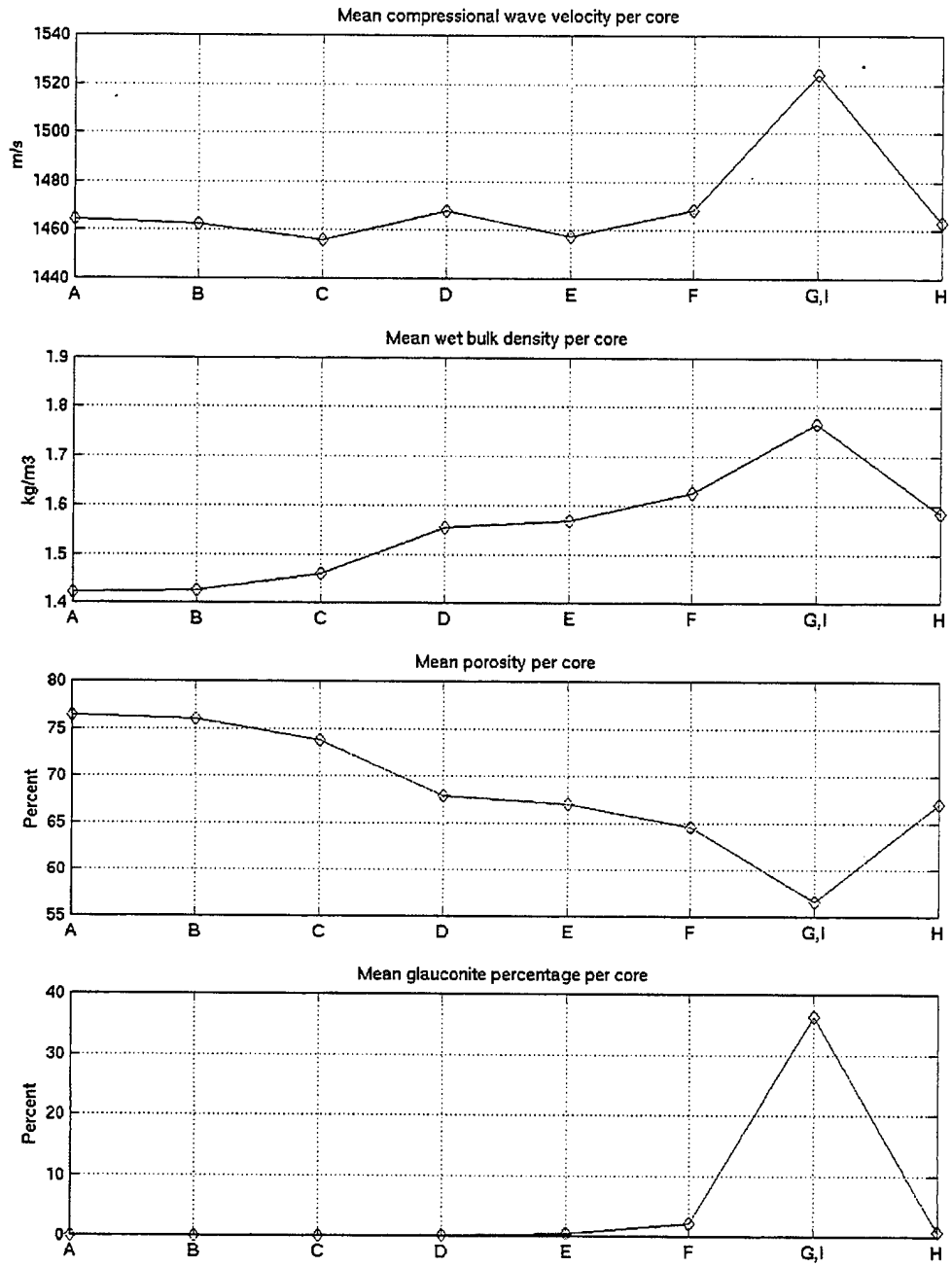

Figure 4.4. Mean values of compressional wave velocity, wet bulk density, porosity, and glauconite percentages for cores A-I.

significant decrease. Finally, proceeding further east, out of the trough and onto the upper part of Sur slope (Core H), the mean compressional wave velocity decreases rapidly due to the sediment resuming the characteristics seen along the western face of Sur Ridge. The much finer sediment produces a slower compressional wave velocity, lower mean wet bulk density, and higher mean porosity. The percentage of glauconite within the core drops as well. Of significance is the closeness in mean values for all curves between the upper western face of Sur Ridge and the upper part of Sur slope (compare Core F and Core H). These two cores appear to be very similar in all respects and could possibly represent what the sediment layer looked like in the vicinity of cores G and I prior to the formation of Sur Ridge and the subsequent erosion that created the trough.

D. *IN-SITU* SEDIMENT VALUES IN THE MODELING OF ACOUSTIC TOMOGRAPHY SIGNALS

The *in-situ* compressional wave velocities for the sediment in all cores were found to be slower than the *in-situ* compressional wave velocity of the bottom water. This is to be expected, based on the dominance of fine-grained sediment within the cores (Hamilton, 1970b). This relationship at the water-sediment interface indicates that a surficial sound channel exists in the sediment sampled for this study. However, the observed signals from Onofre (1999) were coherent, strong signals, indicating that the majority of the energy was reflected and was not attenuated significantly. Onofre (1999) used a frequency of 400 Hz for the transmissions from Davidson Seamount to Sur Ridge. Using an average compressional wave velocity of 1500 m/s, the wavelength would be 3.75 m, and the acoustic energy would nominally penetrate the sediment to this depth. The average penetration of the gravity cores in this study was 1.34 m, only a fraction of

The average penetration of the gravity cores in this study was 1.34 m, only a fraction of the depth that the acoustic energy penetrates. Furthermore, the positive sound speed gradient necessary for the reflection of energy into the ocean was not seen in any of the compressional wave velocity profiles from the cores. The conclusion is that the sediment cores did not penetrate deep enough to obtain an accurate profile of the sediment sound speed gradient. At some point just below the maximum core depth that was sampled, the sound speed gradient increases such that the compressional wave velocity of the sediment is greater than that of the bottom water. This increase in gradient would provide the reflection necessary to produce the strong observed signals that were seen in the work conducted by Onofre (1999).

V. CONCLUSIONS

Several conclusions can be formed based on the sedimentological and acoustic analyses conducted on gravity cores obtained near Sur Ridge, California. From the composition of the sediment and the geomorphology of the area, depositional environments can be determined, as well as possible stratigraphic layers and tectonic effects. From the comparison of the grain-size and acoustic analyses, the mineralogy of the sediment can be used to help better understand the interactions between sediment and acoustic energy. Finally, while an attempt was made to use *in-situ* values of specific sediment parameters in the modeling of acoustic tomography signals, the in-situ values did not provide the necessary data needed to accurately represent the interaction of the acoustic energy with the bottom sediments.

A. GEOMORPHOLOGY AND SEDIMENTATION REGIMES

The moderate to strong percentage of glauconite within the sediment along Sur slope indicates that at some point in geologic history, sea level was such that an environment for the formation of glauconite existed. In addition, either concurrent or shortly after the formation of the glauconite layer, Sur slope underwent a period of deposition of fine-grained, hemipelagic silty clay that exists today.

Two types of depositional environments appear to have been created by the geomorphology and bottom currents. The dominant depositional environment is found along the lower and middle western slope (~1900-2600 m) of Sur slope, as well as the upper continental slope (~700-900 m) to the east of Sur Ridge. It is characterized as a

quiescent, low-energy environment that is relatively undisturbed by recent tectonism or bottom currents. The second depositional environment is found along the upper western slope (800-1900 m) of Sur Ridge and in the trough (1100-1400 m) between Sur Ridge and the upper continental slope. It is characterized as a moderately high-energy erosional environment that shows the effects of relatively strong bottom currents. The dominant grain-size of sediment in this region is typically very high (3φ) compared to the sediment found on the upper and lower continental slope (7φ), as the fine-grained material has been winnowed away, leaving only coarser, glauconite-rich sediment.

Bottom currents flowing along Sur Ridge support the erosional environment in the trough region, but do not necessarily support the erosional environment on the upper western slope of Sur Ridge. Further research in this area would help resolve any ambiguities in terms of bottom currents and their effects on depositional environments. In addition, the higher energy environment in the trough is not favorable for the creation of recent glauconite grains. This leads one to question the origin of the glauconite found in such heavy concentrations in the trough. The vertical uplift involved in the formation of Sur Ridge (due to tectonic activity) probably created a zone of preferential erosion along the fault line. The vertical offset of the ridge could also have caused the focusing of previously existing bottom currents, creating a jet strong enough to winnow the sediment along the zone of preferential erosion, creating the trough. If this is the case, then the glauconite deposits found in the trough represent a lag deposit, since the finer material found on the upper slope and along the western slope of Sur Ridge has long since been winnowed.

B. SEDIMENTARY EFFECTS ON ACOUSTIC PROPERTIES

While in most cases the sediment within the cores behaved in a manner as described in the work of Hamilton (1970a, 1970c, 1971, 1972, 1974, 1976, 1978), it was seen that the compressional wave velocity was controlled by two opposing factors: porosity and density. The highly porous, poorly consolidated sediments at the tops of the deepest cores showed that the compressional wave velocity was controlled by the large percentage of pore water within the sediment. Thus initially a drop is seen in the compressional wave velocity as density increases; however, as the sediment becomes well consolidated deeper into the sediment column, the effects of density take over from that of porosity, and the compressional wave velocity begins to increase with an increase in density. In addition, the variable percentages of glauconite within the sediment added to the complexity of the acoustic characteristics seen. A significant percentage of glauconite in the sediment was seen to lead to increases in density (due to the iron contained in the mineral), compressional wave velocity (due to coarsening of the sediment), strongly positive magnetic anomalies, and an increase (coarsening) in the median grain size. Finally, magnetic susceptibility profiles are particularly useful in determining the concentration of glauconite and its effects on the density and velocity profiles.

C. ACOUSTIC TOMOGRAPHY MODIFICATIONS

The existence of a probable surficial sound channel in the study area, as evidenced by the *in-situ* compressional wave velocity profiles, did not allow for the proper implementation of the modifications intended for the acoustic model. The information obtained from the sediment in this study did not show the compressional

wave velocity gradient within the sediment that would be needed for the acoustic wave to be propagated back into the ocean. Therefore, no comparison could be made between the previous model data (Onofre 1999) and the model data derived from the *in-situ* data. Future work in the validation of bottom-interacting acoustic models should ensure that enough sediment is obtained, based on the frequency of the acoustic energy, such that an adequate profile of the sound speed gradient within the sediment can be obtained.

APPENDIX A –ACOUSTIC ANALYSIS DATA

CORE A

Increment (cm)	Velocity (km/s)	Density (g/m^3)	Magnetic Susceptibility	Temperature (C)
0				23.1
1				23.1
2				23.1
3				23.1
4				23.1
5	1.519238			23.1
6	1.521853	1.270819		23.1
7	1.519238	1.288173	2	23.1
8	1.514036	1.302511	2	23.1
9	1.514036	1.311683	2	23.1
10	1.511447	1.324058	-1	23.1
11	1.511447	1.336808	1	23.1
12	1.511447	1.314525	1	23.1
13	1.508868	1.319619	1	23.1
14	1.508868	1.308975	0	23.1
15	1.506298	1.360367	1	23.1
16	1.503736	1.321474	-1	23.1
17	1.506298	1.339803	0	23.1
18	1.506298	1.35194	2	23.1
19	1.503736	1.37923	0	23.1
20	1.501183	1.335145	1	23.1
21	1.501183	1.332487	1	23.1
22	1.498639	1.346534	2	23.1
23	1.496103	1.3424	2	23.1
24	1.498639	1.312145	1	23.1
25	1.496103	1.371633	0	23.1
26	1.496103	1.370491	0	23.1
27	1.496103	1.37701	0	23.1
28	1.493576	1.362443	0	23.1
29	1.496103	1.374387	0	23.1
30	1.493576	1.386438	0	23.1
31	1.496103	1.3988	2	23.1
32	1.496103	1.398394	1	23.1
33	1.496103	1.373648	0	23.1
34	1.496103	1.385697	-1	23.1
35	1.496103	1.394607	0	23.1
36	1.496103	1.381856	1	23.1
37	1.492689	1.387987	2	23.1

Increment (cm)	Velocity (km/s)	Density (g/m^3)	Magnetic Susceptibility	Temperature (C)
38	1.492689	1.407089	2	23.1
39	1.492689	1.434561	1	23.1
40	1.490168	1.418107	0	23.1
41	1.490168	1.387109	2	23.1
42	1.490168	1.389136	1	23.1
43	1.487655	1.398474	2	23.1
44	1.490168	1.378002	0	23.1
45	1.490168	1.427656	2	23.1
46	1.487655	1.408583	2	23.1
47	1.490168	1.399965	-1	23.1
48	1.487655	1.411166	-1	23.1
49	1.487655	1.403355	-1	23.1
50	1.490168	1.408583	-1	23.1
51	1.487655	1.442644	-1	23.1
52	1.487655	1.415656	0	23.1
53	1.487655	1.403423	1	23.1
54	1.487655	1.403762	-1	23.1
55	1.487655	1.429296	-2	23.1
56	1.490168	1.438326	1	23.1
57	1.490168	1.395562	0	23.1
58	1.490168	1.406002	-1	23.1
59	1.490168	1.433193	0	23.1
60	1.490168	1.427451	1	23.1
61	1.490168	1.397051	2	23.1
62	1.487655	1.375981	1	23.1
63	1.487655	1.393937	2	23.1
64	1.487655	1.384611	0	23.1
65	1.487655	1.398609	0	23.1
66		1.408719	-2	23.1
67	1.487655	1.3778	-2	23.1
68	1.490168	1.417562	-1	23.1
69	1.490168	1.412254	-1	23.1
70	1.487655	1.400914	0	23.1
71	1.490168	1.43545	-1	23.1
72	1.48676	1.418901	-1	23.1
73	1.48676	1.417332	0	23.1
74	1.48676	1.429286	2	23.1
75	1.48676	1.431545	2	23.1
76	1.484253	1.404057	-1	23.1
77	1.484253	1.427097	1	23.1
78	1.48676	1.435587	1	23.1

Increment (cm)	Velocity (km/s)	Density (g/m^3)	Magnetic Susceptibility	Temperature (C)
79	1.489275	1.436341	1	23.1
80	1.489275	1.457654	1	23.1
81	1.489275	1.457654	0	23.1
82	1.489275	1.423543	1	23.1
83	1.489275	1.416923	0	23.1
84	1.48676	1.422792	1	23.1
85	1.489275	1.437369	0	23.1
86	1.489275	1.464763	2	23.1
87	1.489275	1.449527	1	23.1
88	1.489275	1.452349	1	23.1
89	1.489275	1.459379	-1	23.1
90	1.489275	1.451247	2	23.1
91	1.489275	1.484437	1	23.1
92	1.489275	1.461518	2	23.1
93	1.489275	1.456758	2	23.1
94	1.489275	1.439427	1	23.1
95	1.489275	1.455655	2	23.1
96	1.4918	1.438398	0	23.1
97	1.4918		1	23.1
98	1.489275	1.444095	2	23.1
99	1.489275	1.436478	0	23.1
100	1.4918	1.491042	2	23.1
101	1.490907	1.482074	1	23.1
102	1.48838	1.469098	-1	23.1
103	1.493443	1.497119	1	23.1
104	1.48838	1.477767	2	23.1
105	1.490907	1.494328	2	23.1
106	1.48838	1.495863	2	23.1
107	1.490907	1.502916	2	23.1
108	1.490907	1.507533	-1	23.1
109	1.490907	1.492864	-1	23.1
110	1.48838	1.509143	0	23.1
111	1.48838	1.503546	0	23.1
112		1.433953		23.1
113				23.1
114				23.1
115				23.1
116				23.1

Note: The file is created on 10/13/0 at 4:33 PM
The Cruise ID: Gabriel small liner, Core ID: Core A , Scan Increment: 1

Start at: 0, Core Length: 116, at Temperature: 23.1 C
Magnetic Constant: 1
The Last Temperature: 22.6 C

CORE B

Increment (cm)	Velocity (km/s)	Density (g/m^3)	Magnetic Susceptibility	Temperature (C)
0				22.4
1				22.4
2				22.4
3				22.4
4				22.4
5	1.521523	1.305172		22.4
6	1.515433	1.329512	-1	22.4
7	1.512831	1.319312	0	22.4
8	1.510238	1.327876	-1	22.4
9	1.512831	1.332591	-1	22.4
10	1.509363	1.358779	-1	22.4
11	1.506776	1.369105	0	22.4
12	1.506776	1.332632	-1	22.4
13	1.511959	1.310974	1	22.4
14	1.501628	1.322867	0	22.4
15	1.506776	1.338543	-2	22.4
16	1.509363	1.385181	0	22.4
17	1.506776	1.332107	-1	22.4
18	1.509363	1.292232	-2	22.4
19	1.511959	1.391777	-2	22.4
20	1.505895	1.385435	2	22.4
21	1.505895	1.387903	2	22.4
22	1.503314	1.406096	-1	22.4
23	1.505895	1.400133	2	22.4
24	1.503314	1.399464	2	22.4
25	1.503314	1.396854	-1	22.4
26	1.505895	1.389305	-1	22.4
27	1.505895	1.367676	1	22.4
28	1.505895	1.378574	-2	22.4
29	1.505895	1.378974	1	22.4
30	1.505895	1.358796	1	22.4
31	1.505895	1.351125	1	22.4
32	1.503314	1.396587	-1	22.4
33	1.503314	1.36834	2	22.4
34	1.503314	1.396921	2	22.4
35	1.503314	1.399932	-1	22.4
36	1.503314	1.390039	0	22.4
37	1.500742	1.381704	-1	22.4
38	1.500742	1.39652	1	22.4
39	1.498178	1.40945	-2	22.4

Increment (cm)	Velocity (km/s)	Density (g/m^3)	Magnetic Susceptibility	Temperature (C)
40	1.500742	1.427143	0	22.4
41	1.500742	1.417848	-1	22.4
42	1.500742	1.410994	1	22.4
43	1.500742	1.376978	2	22.4
44	1.500742	1.424985	-2	22.4
45	1.500742	1.439504	-1	22.4
46	1.498178	1.430584	-1	22.4
47	1.498178	1.443837	1	22.4
48	1.498178	1.407169	0	22.4
49	1.500742	1.428762	-1	22.4
50	1.493077	1.407772	-1	22.4
51	1.490539	1.420877	2	22.4
52	1.498178	1.421213	1	22.4
53	1.498178	1.423705	1	22.4
54	1.498178	1.425794	1	22.4
55	1.498178	1.451975	1	22.4
56	1.500742	1.392643	-1	22.4
57	1.497286	1.45383	-2	22.4
58	1.492179	1.423819	2	22.4
59	1.495623	1.421348	0	22.4
60	1.495623	1.454488	-1	22.4
61	1.492179	1.45982	0	22.4
62	1.492179	1.446966	-1	22.4
63	1.494728	1.443234	0	22.4
64	1.494728	1.429828	0	22.4
65	1.493077	1.43369	-2	22.4
66	1.490539	1.407102	-2	22.4
67	1.490539	1.432541	-2	22.4
68	1.487107	1.449343	1	22.4
69	1.489639	1.439234	-3	22.4
70	1.487107	1.442962	0	22.4
71	1.493077	1.406096	0	22.4
72	1.493077	1.429774	-2	22.4
73	1.48801	1.404621	1	22.4
74	1.490539	1.41274	-1	22.4
75	1.490539	1.407638	-1	22.4
76	1.493077	1.422021	-2	22.4
77	1.490539	1.418925	-1	22.4
78	1.490539	1.425862	-2	22.4
79	1.489639	1.416068	-2	22.4
80	1.489639	1.419368	-1	22.4

Increment (cm)	Velocity (km/s)	Density (g/m^3)	Magnetic Susceptibility	Temperature (C)
81	1.487107	1.40961	-1	22.4
82	1.489639	1.43091	0	22.4
83	1.489639	1.397532	0	22.4
84	1.489639	1.410887	-1	22.4
85	1.487107	1.409274	0	22.4
86	1.489639	1.417819	-1	22.4
87	1.487107	1.431586	-1	22.4
88	1.487107	1.41203	0	22.4
89	1.487107	1.443437	-2	22.4
90	1.487107	1.432465	-3	22.4
91	1.484584	1.436999	-1	22.4
92	1.487107	1.421323	-2	22.4
93	1.487107	1.415798	-2	22.4
94	1.487107	1.417953	0	22.4
95	1.48801	1.421079	-1	22.4
96	1.48801	1.396052	-3	22.4
97	1.490539	1.435717	-2	22.4
98	1.48801	1.434501	-2	22.4
99	1.48801	1.431259	-1	22.4
100	1.490539	1.45442	-2	22.4
101	1.490539	1.409785	-1	22.4
102	1.48801	1.384036	0	22.4
103	1.48801	1.438489	0	22.4
104	1.490539	1.44587	-3	22.4
105	1.490539	1.457343	-1	22.4
106	1.490539	1.452315	0	22.4
107	1.48801	1.424042	0	22.4
108	1.48801	1.44316	-1	22.4
109	1.48801	1.451568	-1	22.4
110	1.48801	1.429706	-2	22.4
111	1.48801	1.479917	0	22.4
112	1.490539	1.471717	0	22.4
113	1.48801	1.445396	0	22.4
114	1.48801	1.449328	-1	22.4
115	1.48801	1.427412	-2	22.4
116	1.48801	1.436055	-2	22.4
117	1.490539	1.491222	-1	22.4
118	1.490539	1.490193	0	22.4
119	1.490539	1.478959	1	22.4
120	1.48801	1.439301	-3	22.4
121	1.490539	1.46088	0	22.4

Increment (cm)	Velocity (km/s)	Density (g/m^3)	Magnetic Susceptibility	Temperature (C)
122	1.48801	1.425322	-2	22.4
123	1.48801	1.442753	0	22.4
124	1.490539	1.46088	0	22.4
125	1.490539	1.462514	-1	22.4
126	1.490539	1.44079	-2	22.4
127	1.490539	1.4551	0	22.4
128	1.487107	1.438895	0	22.4
129	1.487107	1.446219	0	22.4
130	1.487107	1.438082	0	22.4
131	1.489639	1.41082	0	22.4
132	1.489639	1.440183	1	22.4
133	1.489639	1.435239	0	22.4
134	1.489639	1.413174	0	22.4
135	1.489639	1.450634	1	22.4
136	1.489639	1.473882	0	22.4
137	1.494112	1.437782		22.4
138				22.4
139				22.4
140				22.4
141				22.4
142				22.4

Note: The file is created on 10/17/0 at 4:13 PM
The Cruise ID: Gabriel small liner, Core ID: Core B 7-17 Rot 90 , Scan Increment: 1

Start at: 0, Core Length: 142, at Temperature: 22.4 C
Magnetic Constant: 1
The Last Temperature: 22.0 C

CORE C

Increment (cm)	Velocity (km/s)	Density (g/m^3)	Magnetic Susceptibility	Temperature (C)
0	999.99			22.7
1	999.99			22.7
2	999.99			22.7
3	999.99			22.7
4				22.7
5	1.517547	1.303071		22.7
6	1.51493	1.328381		22.7
7	1.51493	1.303931	2	22.7
8	1.51493	1.339865	1	22.7
9	1.51493	1.351787	1	22.7
10	1.509724	1.319592	4	22.7
11	1.512323	1.362402	5	22.7
12	1.512323	1.369541	5	22.7
13	1.509724	1.366913	4	22.7
14	1.507135	1.351384	5	22.7
15	1.507135	1.349976	2	22.7
16	1.504554	1.394093	4	22.7
17	1.507135	1.413691	2	22.7
18	1.504554	1.423323	2	22.7
19	1.501982	1.451409	4	22.7
20	1.499419	1.420315	5	22.7
21	1.496865	1.457687	3	22.7
22	1.501982	1.475199	6	22.7
23	1.504554	1.467367	4	22.7
24	1.501982	1.434971	4	22.7
25	1.501982	1.473326	5	22.7
26	1.498531	1.47512	7	22.7
27	1.498531	1.469081	4	22.7
28	1.495974	1.459037	4	22.7
29	1.490886	1.451643	6	22.7
30	1.490886	1.474287	4	22.7
31	1.490886	1.437588	7	22.7
32	1.490886	1.43972	5	22.7
33	1.491782	1.458032	6	22.7
34	1.491782	1.435314	5	22.7
35	1.494319	1.452374	5	22.7
36	1.494319	1.46363	3	22.7
37	1.496865	1.449273	6	22.7
38	1.494319	1.478044	6	22.7
39	1.491782	1.473048	6	22.7

Increment (cm)	Velocity (km/s)	Density (g/m^3)	Magnetic Susceptibility	Temperature (C)
40	1.489254	1.430993	5	22.7
41	1.491782	1.434285	5	22.7
42	1.491782	1.464668	6	22.7
43	1.491782	1.460588	6	22.7
44	1.491782	1.45748	6	22.7
45	1.489254	1.449686	7	22.7
46	1.489254	1.423187	7	22.7
47	1.489254	1.463146	4	22.7
48	1.489254	1.448653	4	22.7
49	1.486734	1.455133	4	22.7
50	1.486734	1.461971	4	22.7
51	1.486734	1.445761	4	22.7
52	1.489254	1.460588	7	22.7
53	1.489254	1.453891	6	22.7
54	1.491782	1.448515	7	22.7
55	1.489254	1.450306	4	22.7
56	1.485832	1.462636	6	22.7
57	1.485832	1.463813	4	22.7
58	1.488355	1.446814	5	22.7
59	1.488355	1.45185	4	22.7
60	1.488355	1.41025	3	22.7
61	1.490886	1.463328	4	22.7
62	1.488355	1.44151	4	22.7
63	1.485832	1.432914	6	22.7
64	1.488355	1.456133	4	22.7
65	1.490886	1.427698	6	22.7
66	1.488355	1.406293	3	22.7
67	1.488355	1.429482	5	22.7
68	1.488355	1.474356	6	22.7
69	1.488355	1.453439	4	22.7
70	1.488355	1.485208	3	22.7
71	1.488355	1.440752	3	22.7
72	1.485832	1.462428	5	22.7
73	1.488355	1.478039	5	22.7
74	1.488355	1.449159	4	22.7
75	1.485832	1.428658	6	22.7
76	1.485832	1.436419	7	22.7
77	1.485832	1.467486	3	22.7
78	1.488355	1.46409	7	22.7
79	1.488355	1.468041	5	22.7
80	1.488355	1.471995	4	22.7

Increment (cm)	Velocity (km/s)	Density (g/m^3)	Magnetic Susceptibility	Temperature (C)
81	1.490886	1.458138	4	22.7
82	1.488355	1.500846	3	22.7
83	1.490886	1.469358	5	22.7
84	1.485832	1.466169	5	22.7
85		1.450194	6	22.7
86		1.46416	3	22.7
87		1.481517	5	22.7
88		1.429413	5	22.7
89		1.439858	4	22.7
90	1.495974	1.441578	5	22.7
91	1.490886	1.456133	5	22.7
92	1.495974	1.465684	6	22.7
93	1.495974	1.465684	3	22.7
94	1.495974	1.488344	5	22.7
95	1.490886	1.436694	6	22.7
96	1.490886	1.486462	4	22.7
97	1.490886	1.48284	2	22.7
98	1.493426	1.483606	5	22.7
99	1.488355	1.459037	5	22.7
100	1.485832	1.479082	5	22.7
101	1.490886	1.467833	2	22.7
102	1.490886	1.470121	6	22.7
103	1.485832	1.468665	3	22.7
104	1.488355	1.49742	5	22.7
105	1.485832	1.484372	3	22.7
106	1.496865	1.443422	6	22.7
107	1.496865	1.481657	4	22.7
108	1.491782	1.46993	3	22.7
109	1.489254	1.49663	2	22.7
110	1.491782	1.477142	5	22.7
111	1.491782	1.471315	3	22.7
112	1.496865	1.496281	3	22.7
113	1.490886	1.471024	4	22.7
114	1.490886	1.48946	3	22.7
115	1.488355	1.463121	4	22.7
116	1.490886	1.47387	3	22.7
117	1.493426	1.487856	5	22.7
118	1.490886	1.462221	4	22.7
119	1.480812	1.467486	5	22.7
120	1.480812	1.467001	4	22.7
121	1.485832	1.482144	5	22.7

Increment (cm)	Velocity (km/s)	Density (g/m^3)	Magnetic Susceptibility	Temperature (C)
122	1.484222	1.454719	4	22.7
123		1.480336	5	22.7
124		1.468613	3	22.7
125		1.475893	3	22.7
126		1.47735	1	22.7
127		1.449366	4	22.7
128		1.457447	4	22.7
129		1.471648	4	22.7
130		1.472065	1	22.7
131		1.472481	2	22.7
132		1.470121	4	22.7
133		1.489111	2	22.7
134		1.49721	4	22.7
135		1.479569	3	22.7
136	1.485832	1.446263	3	22.7
137	1.490886	1.475398	4	22.7
138	1.490886	1.426807	2	22.7
139	1.490886	1.463467	4	22.7
140	1.488355	1.483119	2	22.7
141	1.493426	1.442611	4	22.7
142	1.495974	1.48486	1	22.7
143	1.495974	1.481378	4	22.7
144	1.493426	1.465892	1	22.7
145	1.475826	1.453093	3	22.7
146	1.483318	1.458622		22.7
147				22.7
148				22.7
149				22.7
150				22.7
151				22.7

Note: The file is created on 10/13/0 at 2:07 PM
The Cruise ID: Gabriel small liner, Core ID: Core C , Scan Increment: 1

Start at: 0, Core Length: 151, at Temperature: 22.7 C
Magnetic Constant: 1
The Last Temperature: 22.3 C

CORE D

Increment (cm)	Velocity (km/s)	Density (g/m^3)	Magnetic Susceptibility	Temperature (C)
0				23.2
1				23.2
2				23.2
3				23.2
4				23.2
5	1.526889	1.456704		23.2
6	1.529531	1.414056		23.2
7	1.529531	1.465307	3	23.2
8	1.524256	1.446338	4	23.2
9	1.524256	1.427125	3	23.2
10	1.518161	1.43374	5	23.2
11	1.520778	1.47405	6	23.2
12	1.520778	1.495834	6	23.2
13	1.5173	1.481868	5	23.2
14	1.5173	1.477914	5	23.2
15	1.5173	1.524737	5	23.2
16	1.5173	1.525509	7	23.2
17	1.5173	1.52825	6	23.2
18	1.514689	1.547562	7	23.2
19	1.5173	1.534371	5	23.2
20	1.514689	1.536695	6	23.2
21	1.511217	1.572713	5	23.2
22	1.511217	1.548993	5	23.2
23	1.506033	1.551188	5	23.2
24	1.511217	1.545597	6	23.2
25	1.513823	1.571858	7	23.2
26	1.511217	1.544253	5	23.2
27	1.511217	1.554306	8	23.2
28	1.513823	1.585989	6	23.2
29	1.510345	1.570483	5	23.2
30	1.507745	1.58198	7	23.2
31	1.505154	1.567419	7	23.2
32	1.5	1.530137	8	23.2
33	1.502573	1.504836	6	23.2
34	1.5	1.502386	8	23.2
35	1.502573	1.525133	7	23.2
36	1.502573	1.543277	6	23.2
37	1.505154	1.544693	8	23.2
38	1.502573	1.5343	7	23.2
39	1.5	1.511426	7	23.2

Increment (cm)	Velocity (km/s)	Density (g/m^3)	Magnetic Susceptibility	Temperature (C)
40	1.505154	1.524218	5	23.2
41	1.502573	1.54618	5	23.2
42	1.50862	1.529437	8	23.2
43	1.50862	1.578917	8	23.2
44	1.506033	1.568868	7	23.2
45	1.503454	1.539943	6	23.2
46	1.500884	1.538461	6	23.2
47	1.498323	1.52423	5	23.2
48	1.503454	1.534862	6	23.2
49	1.503454	1.552888	6	23.2
50	1.500884	1.541992	7	23.2
51	1.503454	1.552888	7	23.2
52	1.500884	1.54588	6	23.2
53	1.506033	1.563534	6	23.2
54	1.503454	1.586275	7	23.2
55	1.500884	1.552463	4	23.2
56	1.500884	1.594007	4	23.2
57	1.504332	1.554706	5	23.2
58	1.504332	1.569819	7	23.2
59	1.504332	1.560304	4	23.2
60	1.504332	1.593858	6	23.2
61	1.509493	1.559737	5	23.2
62	1.509493	1.573091	6	23.2
63	1.504332	1.55917	5	23.2
64	1.501765	1.537259	5	23.2
65	1.504332	1.578788	4	23.2
66	1.504332	1.561723	6	23.2
67	1.506908	1.585423	4	23.2
68	1.506908	1.577221	4	23.2
69	1.504332	1.581712	5	23.2
70	1.504332	1.568113	5	23.2
71	1.506908	1.577292	4	23.2
72	1.506908	1.558674	5	23.2
73	1.506908	1.602671	7	23.2
74	1.506908	1.588137	6	23.2
75	1.512086	1.596292	6	23.2
76	1.514689	1.626855	6	23.2
77	1.512086	1.59021	5	23.2
78	1.512086	1.596435	6	23.2
79	1.512086	1.630684	5	23.2
80	1.512086	1.594645	6	23.2

Increment (cm)	Velocity (km/s)	Density (g/m^3)	Magnetic Susceptibility	Temperature (C)
81	1.514689	1.615391	3	23.2
82	1.512086	1.600878	6	23.2
83	1.512086	1.592141	3	23.2
84	1.514689	1.644373	2	23.2
85	1.512086	1.63459	3	23.2
86	1.509493	1.600878	4	23.2
87	1.504332	1.581498	3	23.2
88	1.506908	1.596507	6	23.2
89	1.501765	1.577648	6	23.2
90	1.496657	1.544948	6	23.2
91	1.499207	1.55591	4	23.2
92	1.499207	1.503868	3	23.2
93	1.499207	1.534019	4	23.2
94	1.496657	1.491181	5	23.2
95	1.494116	1.510298	5	23.2
96	1.496657	1.518211	5	23.2
97	1.499207	1.53057	4	23.2
98	1.504332	1.581498	4	23.2
99	1.509493	1.608846	5	23.2
100	1.514689	1.602599	5	23.2
101	1.506908	1.556902	5	23.2
102	1.501765	1.548975	2	23.2
103	1.509493	1.595433	2	23.2
104	1.519921	1.656583	6	23.2
105	1.527837	1.739862	2	23.2
106	1.506908	1.58628	5	23.2
107	1.509493	1.613664	4	23.2
108	1.512086	1.635097	4	23.2
109	1.512086	1.625267	2	23.2
110	1.512086	1.612009	5	23.2
111	1.512086	1.635893	5	23.2
112	1.514689	1.674098	2	23.2
113	1.519921	1.660079	3	23.2
114	1.514689	1.637269	4	23.2
115	1.509493	1.601882	4	23.2
116	1.506033	1.582916	2	23.2
117	1.506033	1.601323	2	23.2
118	1.50862	1.579845	1	23.2
119	1.516437	0.633933	2	23.2
120		-0.20483	2	23.2
121	999.99	-0.21868	3	23.2

Increment (cm)	Velocity (km/s)	Density (g/m^3)	Magnetic Susceptibility	Temperature (C)
122		-0.16594	3	23.2
123	1.485646	1.042992	3	23.2
124	1.50862	1.488892		23.2
125		1.462661		23.2
126		1.479506		23.2
127				23.2
128				23.2
129				23.2

Note: The file is created on 10/13/0 at 3:59 PM
The Cruise ID: Gabriel small liner, Core ID: Core D , Scan Increment: 1

Start at: 0, Core Length: 129, at Temperature: 23.2 C
Magnetic Constant: 1
The Last Temperature: 22.3 C

CORE E

Increment (cm)	Velocity (km/s)	Density (g/m^3)	Magnetic Susceptibility	Temperature (C)
0	999.99			20.4
1	999.99			20.4
2	999.99			20.4
3	999.99			20.4
4	999.99			20.4
5	999.99			20.4
6	999.99			20.4
7			11	20.4
8	1.521874	1.484439	12	20.4
9	1.517467	1.481569	10	20.4
10	1.517467	1.502411	10	20.4
11	1.520891	1.50198	10	20.4
12		1.505101	13	20.4
13		1.508226	14	20.4
14	1.526791	1.52821	13	20.4
15	1.528274	1.539014	17	20.4
16	1.531247	1.582468	17	20.4
17	1.525312	1.569817	15	20.4
18	1.517957	1.557874	18	20.4
19	1.515035	1.589725	19	20.4
20	1.516495	1.595374	21	20.4
21	1.516495	1.606778	17	20.4
22	1.513579	1.603848	19	20.4
23	1.510674	1.595782	22	20.4
24	1.506337	1.58589	19	20.4
25	1.506337	1.551986	20	20.4
26	1.505394	1.560393	19	20.4
27	1.502524	1.57812	22	20.4
28	1.499665	1.548738	20	20.4
29	1.499665	1.553472	20	20.4
30	1.495396	1.563203	22	20.4
31	1.493979	1.522924	19	20.4
32	1.491152	1.515177	21	20.4
33	1.491152	1.510029	19	20.4
34	1.491658	1.509319	19	20.4
35	1.491658	1.526313	21	20.4
36	1.489743	1.50718	21	20.4
37	1.492564	1.531662	18	20.4
38	1.491152	1.526809	21	20.4
39	1.492564	1.520507	23	20.4

Increment (cm)	Velocity (km/s)	Density (g/m^3)	Magnetic Susceptibility	Temperature (C)
40	1.492564	1.527091	19	20.4
41	1.492564	1.529629	19	20.4
42	1.495396	1.525288	18	20.4
43	1.493979	1.535563	20	20.4
44	1.489743	1.530532	21	20.4
45	1.486932	1.489566	21	20.4
46	1.48553	1.470842	19	20.4
47	1.486932	1.463183	17	20.4
48	1.486932	1.479466	17	20.4
49	1.486932	1.518373	20	20.4
50	1.489743	1.486083	16	20.4
51	1.486932	1.49383	17	20.4
52	1.488336	1.501551	18	20.4
53	1.488336	1.504057	20	20.4
54	1.488336	1.518261	20	20.4
55	1.488336	1.49106	19	20.4
56	1.489743	1.504447	17	20.4
57	1.491152	1.512993	18	20.4
58	1.491152	1.534941	17	20.4
59	1.493979	1.533018	17	20.4
60	1.493979	1.534149	17	20.4
61	1.493979	1.543219	18	20.4
62	1.495396	1.52788	17	20.4
63	1.498239	1.566132	16	20.4
64	1.495396	1.573385	16	20.4
65	1.489235	1.536803	19	20.4
66	1.486423	1.518193	18	20.4
67	1.485021	1.51494	14	20.4
68	1.486423	1.499309	16	20.4
69	1.487828	1.504877	15	20.4
70	1.487828	1.517239	15	20.4
71	1.489235	1.539354	17	20.4
72	1.489235	1.528266	15	20.4
73	1.489235	1.540659	14	20.4
74	1.489235	1.538843	17	20.4
75	1.490646	1.560509	14	20.4
76	1.492059	1.564296	14	20.4
77	1.493474	1.57045	14	20.4
78	1.500593	1.592518	15	20.4
79	1.502025	1.589317	14	20.4
80	1.500593	1.580093	16	20.4

Increment (cm)	Velocity (km/s)	Density (g/m^3)	Magnetic Susceptibility	Temperature (C)
81	1.497737	1.575815	14	20.4
82	1.496314	1.564526	14	20.4
83	1.497737	1.564239	14	20.4
84	1.497737	1.582178	14	20.4
85	1.494893	1.580383	16	20.4
86	1.497737	1.542249	13	20.4
87	1.502025	1.614829	15	20.4
88	1.503459	1.613358	11	20.4
89	1.497737	1.579225	11	20.4
90	1.494893	1.569874	15	20.4
91	1.492059	1.571084	11	20.4
92	1.493474	1.551073	14	20.4
93	1.493474	1.57143	14	20.4
94	1.493474	1.559019	10	20.4
95	1.493474	1.546855	11	20.4
96	1.494893	1.56487	13	20.4
97	1.493474	1.542647	10	20.4
98	1.492059	1.551473	10	20.4
99	1.494893	1.571257	9	20.4
100	1.496314	1.565905	10	20.4
101	1.496314	1.573333	13	20.4
102	1.494893	1.57045	13	20.4
103	1.493474	1.574544	11	20.4
104	1.496314	1.574602	14	20.4
105	1.506337	1.634237	12	20.4
106	1.504897	1.629308	14	20.4
107	1.502025	1.591761	14	20.4
108	1.502025	1.6076	14	20.4
109	1.503459	1.600395	10	20.4
110	1.503459	1.630079	13	20.4
111	1.506337	1.665089	14	20.4
112	1.50778	1.626996	11	20.4
113	1.504897	1.635069	14	20.4
114	1.500593	1.582294	14	20.4
115	1.499164	1.564009	14	20.4
116	1.504897	1.574833	13	20.4
117	1.503459	1.578184	12	20.4
118	1.504897	1.614829	12	20.4
119	1.506337	1.6318	10	20.4
120	1.50778	1.633939	12	20.4
121	1.50778	1.647359	14	20.4

Increment (cm)	Velocity (km/s)	Density (g/m^3)	Magnetic Susceptibility	Temperature (C)
122	1.506337	1.583685	11	20.4
123	1.506337	1.620136	13	20.4
124	1.504897	1.600746	13	20.4
125	1.506337	1.598525	13	20.4
126	1.509225	1.635902	11	20.4
127	1.515035	1.633167	11	20.4
128	1.516004	1.678935	15	20.4
129	1.512125	1.672953	11	20.4
130	1.510674	1.647239	13	20.4
131	1.510674	1.637569	13	20.4
132	1.50778	1.644787	13	20.4
133	1.503459	1.645265	10	20.4
134	1.503459	1.642279	14	20.4
135	1.502025	1.616774	9	20.4
136	1.502025	1.590481	13	20.4
137	1.500593	1.610183	13	20.4
138	1.497737		10	20.4
139	1.496314	1.60543	8	20.4
140	1.493474	1.574949	12	20.4
141		1.508964	12	20.4
142	999.99			20.4
143	999.99			20.4
144	999.99			20.4
145	999.99			20.4
146	999.99			20.4
147	999.99			20.4

Note: The file is created on 10/10/0 at 1:25 PM
The Cruise ID: Gabriel, Core ID: Core E , Scan Increment: 1

Start at: 0, Core Length: 147, at Temperature: 20.4 C
Magnetic Constant: 1
The Last Temperature: 21.1 C

CORE F (TOP SECTION)

Increment (cm)	Velocity (km/s)	Density (g/m^3)	Magnetic Susceptibility	Temperature (C)
0	999.99			20
1	999.99			20
2	999.99			20
3	999.99			20
4	999.99			20
5	999.99			20
6	999.99			20
7	999.99			20
8	999.99	1.505254		20
9	999.99	1.525947	8	20
10	999.99	1.610318	10	20
11	999.99	1.524088	14	20
12	999.99	1.542815	13	20
13	999.99	1.655783	13	20
14	999.99	1.61638	14	20
15	999.99	1.613082	14	20
16	999.99	1.583869	13	20
17	999.99	1.598832	16	20
18	999.99	1.63022	13	20
19		1.616439	13	20
20	1.502523	1.612846	17	20
21	1.50396	1.586888	16	20
22		1.596262	16	20
23		1.596846	15	20
24	1.507339	1.599051	15	20
25	1.518477	1.594629	13	20
26	1.518477	1.60357	13	20
27	1.506841	1.553643	15	20
28	1.507339	1.555528	13	20
29	1.507339	1.553699	14	20
30	1.50396	1.550731	12	20
31	1.508783	1.547026	15	20
32	1.511679	1.547539	12	20
33	1.516043	1.564296	12	20
34	1.517012	1.559481	11	20
35	1.518477	1.575476	12	20
36	1.522887	1.576458	13	20
37	1.519944	1.559423	12	20
38	1.517012	1.557247	14	20
39	1.514092	1.57409	14	20

Increment (cm)	Velocity (km/s)	Density (g/m^3)	Magnetic Susceptibility	Temperature (C)
40	1.513131	1.54902	13	20
41	1.510229	1.557359	10	20
42	1.511679	1.53669	11	20
43	1.513131	1.55965	11	20
44	1.513131	1.541511	11	20
45	1.507339	1.532332	11	20
46	1.507339	1.530072	10	20
47	1.506841	1.553415	14	20
48	1.506841	1.569823	11	20
49	1.509733	1.59562	14	20
50	1.514092	1.609084	12	20
51	1.518477	1.614553	13	20
52	1.519944	1.634379	15	20
53	1.521414	1.6395	15	20
54	1.517012	1.630398		20
55	1.514092	1.613023	12	20
56	1.507339	1.570566	14	20
57	1.501591	1.577664	12	20
58	1.495887	1.53601	13	20
59	1.497309	1.549476	14	20
60	1.501591	1.552557	13	20
61	1.500161	1.521958	10	20
62	1.50446	1.561599	13	20
63	1.510229	1.586645	11	20
64	1.510229	1.581367	13	20
65	1.505399	1.567865	9	20
66	1.50396	1.590492	9	20
67	1.505399	1.606736	12	20
68	1.502523	1.621396	13	20
69	1.493962	1.564875	11	20
70	1.492544	1.543156	13	20
71	1.493962	1.557991	13	20
72	1.495887	1.545262	12	20
73	1.493051	1.5389	11	20
74	1.494468	1.559936	10	20
75	1.497812	1.557073	9	20
76	1.504958	1.572175	10	20
77	1.503524	1.573039	11	20
78	1.500663	1.564696	12	20
79	1.499236	1.569122	13	20
80	1.502092	1.583504	12	20

Increment (cm)	Velocity (km/s)	Density (g/m^3)	Magnetic Susceptibility	Temperature (C)
81	1.500663	1.578814	11	20
82	1.506396	1.591576	10	20
83	1.499236	1.567742	10	20
84	1.497812	1.576733	9	20
85	1.502092	1.602488	8	20
86	1.501237	1.572407	10	20
87			11	20
88				20
89				20
90				20
91				20

Note: The file is created on 10/10/0 at 1:57 PM
The Cruise ID: Gabriel, Core ID: Core F Top , Scan Increment: 1

Start at: 0, Core Length: 91, at Temperature: 20.0 C
Magnetic Constant: 1
The Last Temperature: 20.5 C

CORE F (BOTTOM SECTION)

Increment (cm)	Velocity (km/s)	Density (g/m^3)	Magnetic Susceptibility	Temperature (C)
0	999.99			21
1	999.99			21
2	999.99			21
3	999.99			21
4	999.99			21
5	999.99			21
6	999.99	1.543668		21
7	999.99	1.578077	13	21
8	999.99	1.580913	14	21
9	999.99	1.580287	10	21
10	999.99	1.597621	12	21
11	999.99	1.623193	15	21
12	999.99	1.60922	15	21
13	999.99	1.585958	13	21
14	999.99	1.608673	12	21
15		1.608614	13	21
16	1.514525	1.648224	15	21
17	1.511116	1.598848	16	21
18	1.511116	1.594994	16	21
19	1.521376	1.690682	13	21
20	1.522853	1.656656	16	21
21	1.51843	1.624613	14	21
22	1.511116	1.639229	14	21
23	1.509662	1.61882	15	21
24	1.50821	1.644184	16	21
25	1.51161	1.614023	15	21
26	1.515987	1.663551	15	21
27	1.52039	1.67523	15	21
28	1.523339	1.660236	15	21
29	1.525816	1.691416	16	21
30	1.527301	1.657799	15	21
31	1.522853	1.671264	15	21
32	1.514033	1.671203	16	21
33	1.512573	1.65293	18	21
34	1.505315	1.626864	19	21
35	1.503872	1.594935	16	21
36	1.50821	1.614868	16	21
37	1.509662	1.61941	15	21
38	1.514033	1.642093	18	21
39	1.515496	1.672173	17	21

Increment (cm)	Velocity (km/s)	Density (g/m^3)	Magnetic Susceptibility	Temperature (C)
40	1.503872	1.615458	19	21
41	1.496697	1.614456	15	21
42	1.491006	1.574676	18	21
43	1.491006	1.559485	15	21
44	1.492425	1.572714	18	21
45	1.49527	1.599315	16	21
46	1.500994	1.621655	16	21
47	1.498127	1.612042	17	21
48	1.496697	1.62071	15	21
49	1.498127	1.618466	15	21
50	1.503872	1.66274	16	21
51	1.515496	1.680736	19	21
52	1.521376	1.747749	16	21
53	1.511116	1.686832	17	21
54	1.503872	1.612572	18	21
55	1.503872	1.663041	17	21
56	1.501931	1.668274	18	21
57	1.504817	1.639497	17	21
58	1.506264	1.618076	16	21
59	1.510621	1.655968	16	21
60	1.516471	1.661508	16	21
61	1.519902	1.660991	17	21
62	1.515004	1.654645	15	21
63	1.51794	1.658796	18	21
64	1.516471	1.691213	16	21
65	1.528307	1.755116	18	21
66	1.528307	1.741897	16	21
67	1.523847	1.716397	19	21
68		1.776639	19	21
69	1.538816	1.756443	17	21
70	1.535798	1.728203	19	21
71	1.543364	1.775299	19	21
72	1.528307	1.751331	19	21
73	1.522853	1.732644	16	21
74	1.524333	1.683233	16	21
75	1.527301	1.712512	14	21
76	1.536277	1.753861	15	21
77	1.511116	1.725662	15	21
78	1.511116	1.654612	15	21
79	1.536277	1.719014	18	21
80	1.539292	1.753104	18	21

Increment (cm)	Velocity (km/s)	Density (g/m^3)	Magnetic Susceptibility	Temperature (C)
81	1.530281	1.716969	14	21
82	1.51843	1.71245	15	21
83	1.51843	1.649032	15	21
84	1.525816	1.687992	17	21
85	1.525816	1.657137	18	21
86	1.533273	1.704367	16	21
87	1.537783	1.699324	15	21
88	1.553008	1.710905	16	21
89	1.548409	1.720193	17	21
90	1.545829	1.710429	17	21
91	1.540068	1.680017	18	21
92		1.605774	18	21
93	999.99	1.605737		21
94	999.99			21
95	999.99			21
96	999.99			21
97	999.99			21

Note: The file is created on 10/10/0 at 2:33 PM
The Cruise ID: Gabriel, Core ID: Core F Bottom , Scan Increment: 1

Start at: 0, Core Length: 97, at Temperature: 21.0 C
Magnetic Constant: 1
The Last Temperature: 21.2 C

CORE G

Increment (cm)	Velocity (km/s)	Density (g/m^3)	Magnetic Susceptibility	Temperature (C)
0	999.99			21.1
1	999.99			21.1
2	999.99			21.1
3	999.99			21.1
4	999.99			21.1
5	999.99			21.1
6	999.99			21.1
7	999.99			21.1
8	999.99	1.748676	8	21.1
9	999.99	1.750755	11	21.1
10	999.99	1.761375	12	21.1
11	999.99	1.739312	15	21.1
12	999.99	1.748172	15	21.1
13	999.99	1.732365	13	21.1
14	999.99	1.724507	13	21.1
15	999.99	1.701114	13	21.1
16	999.99	1.715323	16	21.1
17	999.99	1.757955	14	21.1
18	999.99	1.74729	14	21.1
19	999.99	1.731927	16	21.1
20	999.99	1.685972	15	21.1
21		1.688967	17	21.1
22	1.598558	1.709376	17	21.1
23	1.608446	1.772497	18	21.1
24	1.610106	1.817603	17	21.1
25	1.601841	1.772242	16	21.1
26	1.594098	1.769947	15	21.1
27	1.594098	1.798594	17	21.1
28	1.597358	1.799304	20	21.1
29	1.598993	1.841709	18	21.1
30	1.594098	1.855534	20	21.1
31	1.586006	1.853676	21	21.1
32	1.579592	1.792729	20	21.1
33	1.56378	1.808622	18	21.1
34	1.56849	1.784508	18	21.1
35	1.573229	1.767149	21	21.1
36	1.573229	1.773386	18	21.1
37	1.552899	1.773705	19	21.1
38	1.551357	1.759664	22	21.1
39	1.557544	1.770902	19	21.1

Increment (cm)	Velocity (km/s)	Density (g/m^3)	Magnetic Susceptibility	Temperature (C)
40	1.56378	1.774661	20	21.1
41	1.570067	1.754984	21	21.1
42	1.576404	1.763466	20	21.1
43	1.581191	1.747921	22	21.1
44	1.584572	1.791378	20	21.1
45		1.851046	21	21.1
46	999.99	1.786354	21	21.1
47	999.99	1.760569	20	21.1
48	999.99			21.1
49	999.99			21.1
50	999.99			21.1
51	999.99			21.1

Note: The file is created on 10/10/0 at 3:14 PM
The Cruise ID: Gabriel, Core ID: Core G , Scan Increment: 1

Start at: 0, Core Length: 51, at Temperature: 21.1 C
Magnetic Constant: 1
The Last Temperature: 21.2 C

CORE H (TOP SECTION)

Increment (cm)	Velocity (km/s)	Density (g/m^3)	Magnetic Susceptibility	Temperature (C)
0	999.99			21.2
1	999.99			21.2
2	999.99			21.2
3	999.99			21.2
4	999.99			21.2
5	999.99			21.2
6	999.99	1.425802		21.2
7	999.99	1.48475	11	21.2
8	999.99	1.507058	12	21.2
9	999.99	1.457328	13	21.2
10	999.99	1.502811	16	21.2
11		1.563547	12	21.2
12	1.529357	1.550248	16	21.2
13	1.530858	1.564179	14	21.2
14	1.529357	1.599168	16	21.2
15	1.530858	1.624609	15	21.2
16	1.532362	1.622595	17	21.2
17	1.532843	1.615651	17	21.2
18	1.531341	1.632472	18	21.2
19	1.532843	1.657968	16	21.2
20	1.532843	1.639503	16	21.2
21	1.531341	1.652615	19	21.2
22	1.529841	1.640219	16	21.2
23	1.529357	1.641928	16	21.2
24	1.527859	1.659456	18	21.2
25	1.529357	1.654218	18	21.2
26	1.529841	1.658932	18	21.2
27	1.528344	1.640936	19	21.2
28	1.529841	1.648894	19	21.2
29	1.532843	1.678123	15	21.2
30	1.528344	1.646078	15	21.2
31	1.522385	1.649614	18	21.2
32	1.519424	1.653336	18	21.2
33	1.520903	1.623807	15	21.2
34	1.520903	1.626237	18	21.2
35	1.519424	1.620553	18	21.2
36	1.522385	1.625644	16	21.2
37	1.522385	1.643446	14	21.2
38	1.522385	1.647636	17	21.2
39	1.524872	1.662653	16	21.2

Increment (cm)	Velocity (km/s)	Density (g/m^3)	Magnetic Susceptibility	Temperature (C)
40	1.529357	1.664526	17	21.2
41	1.535378	1.673915	18	21.2
42	1.533868	1.698777	18	21.2
43	1.532362	1.705364	15	21.2
44	1.529357	1.708141	18	21.2
45	1.533868	1.704316	18	21.2
46	1.528344	1.691305		21.2
47	1.520903	1.670292	18	21.2
48	1.516473	1.66237	17	21.2
49	1.517947	1.671019	15	21.2
50	1.523871	1.676543	18	21.2
51	1.517947	1.660017	17	21.2
52	1.519424	1.671565	14	21.2
53	1.519424	1.690387	14	21.2
54	1.517947	1.699525	17	21.2
55	1.520903	1.657306	15	21.2
56	1.517947	1.659113	14	21.2
57	1.509147	1.649794	12	21.2
58	1.506237	1.651474	13	21.2
59	1.505285	1.612913	15	21.2
60	1.506735	1.615506	14	21.2
61	1.503837	1.574124	12	21.2
62	1.500951	1.591706	10	21.2
63	1.500951	1.580953	12	21.2
64	1.500951	1.613325	11	21.2
65	1.498075	1.59258	8	21.2
66	1.493783	1.558125	9	21.2
67	1.490935	1.537423	12	21.2
68	1.493783	1.546351	11	21.2
69	1.493783	1.611382	10	21.2
70	1.495211	1.538955	8	21.2
71	1.492358	1.581127	7	21.2
72	1.495211	1.554746	9	21.2
73	1.493783	1.555375	11	21.2
74	1.492358	1.583737	6	21.2
75	1.495211	1.517491	8	21.2
76				21.2
77	999.99			21.2
78	999.99			21.2
79	999.99			21.2
80	999.99			21.2

Increment (cm)	Velocity (km/s)	Density (g/m^3)	Magnetic Susceptibility	Temperature (C)
81	999.99			21.2

Note: The file is created on 10/10/0 at 3:40 PM
The Cruise ID: Gabriel, Core ID: Core H Top , Scan Increment: 1

Start at: 0, Core Length: 81, at Temperature: 21.2 C
Magnetic Constant: 1
The Last Temperature: 21.3 C

CORE H (BOTTOM SECTION)

Increment (cm)	Velocity (km/s)	Density (g/m^3)	Magnetic Susceptibility	Temperature (C)
0	999.99			21.6
1	999.99			21.6
2	999.99			21.6
3	999.99			21.6
4	999.99			21.6
5	999.99			21.6
6	999.99	1.52786	8	21.6
7	999.99	1.503903	7	21.6
8	999.99	1.524645	5	21.6
9	999.99	1.518569	9	21.6
10	999.99	1.52442	6	21.6
11	999.99	1.513855	9	21.6
12	999.99	1.532041	5	21.6
13	999.99	1.519082	5	21.6
14	999.99	1.527865	8	21.6
15	999.99	1.525215	6	21.6
16	999.99	1.549248	8	21.6
17	999.99	1.623311	13	21.6
18	999.99	1.65155	11	21.6
19	999.99	1.663283	13	21.6
20		1.67187	13	21.6
21	1.522886	1.664248	13	21.6
22	1.52931	1.705064		21.6
23	1.544362	1.750971	12	21.6
24	1.543891	1.749638	9	21.6
25	1.512596	1.63494	10	21.6
26	1.502444	1.600544	12	21.6
27	1.496704	1.525829	8	21.6
28	1.495276	1.533738	7	21.6
29	1.499569	1.530232	9	21.6
30	1.501005	1.552789	11	21.6
31	1.499569	1.568851	9	21.6
32	1.501005	1.541905	6	21.6
33	1.493851	1.532889	8	21.6
34	1.492428	1.497221	5	21.6
35	1.492428	1.500169	7	21.6
36	1.492428	1.49239	4	21.6
37	1.492428	1.484807	5	21.6
38	1.492428	1.479454	3	21.6
39	1.495276	1.510271	7	21.6

Increment (cm)	Velocity (km/s)	Density (g/m^3)	Magnetic Susceptibility	Temperature (C)
40	1.495276	1.506358	2	21.6
41	1.493851	1.494166	5	21.6
42	1.492428	1.510495	3	21.6
43	1.491008	1.492446	2	21.6
44	1.491008	1.481163	6	21.6
45	1.491008	1.487848	3	21.6
46	1.492428	1.497054	2	21.6
47	1.492428	1.502676	6	21.6
48	1.492428	1.509376	7	21.6
49	1.491008	1.509712	7	21.6
50	1.492428	1.493	4	21.6
51	1.496704	1.516604	4	21.6
52	1.495276	1.538839	3	21.6
53	1.496704	1.519243	4	21.6
54	1.498135	1.533964	6	21.6
55	1.498135	1.551932	6	21.6
56	1.493851	1.540428	5	21.6
57	1.495276	1.520986	8	21.6
58	1.498135	1.518681	4	21.6
59	1.502444	1.53623	5	21.6
60	1.498135	1.573002	7	21.6
61	1.493347	1.538328	5	21.6
62	1.491923	1.509255	9	21.6
63	1.494773	1.525092	5	21.6
64	1.494773	1.528986	9	21.6
65	1.493347	1.505958	6	21.6
66	1.493347	1.516148	7	21.6
67	1.494773	1.489438	7	21.6
68	1.494773	1.519069	8	21.6
69	1.494773	1.517327	6	21.6
70	1.494773	1.505399	9	21.6
71	1.494773	1.492487	9	21.6
72	1.497634	1.513624	8	21.6
73	1.497634	1.526164	8	21.6
74		1.484656	12	21.6
75	999.99	1.480396		21.6
76	999.99	1.523283		21.6
77	999.99			21.6
78	999.99			21.6
79	999.99			21.6
80	999.99			21.6

Note: The file is created on 10/10/0 at 4:07 PM
The Cruise ID: Gabriel, Core ID: Core H Bottom , Scan Increment: 1

Start at: 0, Core Length: 80, at Temperature: 21.6 C
Magnetic Constant: 1
The Last Temperature: 21.7 C

CORE I

Increment (cm)	Velocity (km/s)	Density (g/m^3)	Magnetic Susceptibility	Temperature (C)
0	999.99			21.8
1	999.99			21.8
2	999.99			21.8
3	999.99			21.8
4	999.99			21.8
5	999.99			21.8
6	999.99			21.8
7	999.99			21.8
8	999.99		9	21.8
9	999.99	1.774745	9	21.8
10	999.99	1.853001	9	21.8
11	999.99	1.823245	14	21.8
12	999.99	1.771365	15	21.8
13	999.99	1.784212	16	21.8
14		1.747355	15	21.8
15	1.522951	1.770592	17	21.8
16		1.786639	16	21.8
17	1.505775	1.700499	17	21.8
18	1.564736	1.681031	17	21.8
19	1.5616	1.725939	14	21.8
20	1.572631	1.753153	18	21.8
21	1.580605	1.785283	16	21.8
22	1.564736	1.746598	18	21.8
23	1.560037	1.769313	18	21.8
24	1.563166	1.7395	21	21.8
25	1.553815	1.702283	21	21.8
26	1.558477	1.704686	20	21.8
27	1.558477	1.750503	19	21.8
28	1.55692	1.754542	19	21.8
29	1.5616	1.756375	18	21.8
30	1.564736	1.786694	20	21.8
31	1.571045	1.780799	23	21.8
32	1.567884	1.779392	19	21.8
33	1.555366	1.738811	21	21.8
34	1.552735	1.741949	22	21.8
35	1.554281	1.760867	19	21.8
36	1.555831	1.749936	23	21.8
37	1.5616	1.786053	22	21.8
38	1.55692	1.771669	20	21.8
39	1.558477	1.774793	24	21.8

Increment (cm)	Velocity (km/s)	Density (g/m^3)	Magnetic Susceptibility	Temperature (C)
40	1.55692	1.74088	19	21.8
41	1.558477	1.740316	24	21.8
42	1.547643	1.764483	20	21.8
43	1.556455	1.74767	22	21.8
44	1.559575	1.750821	21	21.8
45		1.675785	19	21.8
46	999.99	1.636297	22	21.8
47	999.99			21.8
48	999.99			21.8
49	999.99			21.8
50	999.99			21.8
51	999.99			21.8

Note: The file is created on 10/10/0 at 4:25 PM
The Cruise ID: Gabriel, Core ID: Core I , Scan Increment: 1

Start at: 0, Core Length: 51, at Temperature: 21.8 C
Magnetic Constant: 1
The Last Temperature: 21.8 C

APPENDIX B – DETAILED ACOUSTIC DESCRIPTION OF CORES

CORE A

Figure B.1 contains laboratory profiles of compressional wave velocity, wet bulk density, and magnetic susceptibility for Core A. No velocity data was obtained for the upper 4 cm of Core A. Below 4 cm, a steady decrease in Vp is seen, from approximately 1.49 km/s at 5 cm to approximately 1.46 km/s at 40 cm; the remainder of the core shows a relatively unchanged velocity of approximately 1.46 km/s. No velocity data was obtained at 66 cm and from 112-116 cm.

No wet bulk density (ρ_b) data was obtained for the upper 5 cm of Core A. A steady increase in density is seen from 6 cm (1.29 g/m^3) to 60 cm (1.44 g/m^3). From 60-62 cm, the density drops to 1.39 g/m^3; below 62 cm, the density begins to steadily increase, reaching a density of 1.48 g/m^3 at 99 cm. No density data was obtained for 97 cm. From 99-101 cm, the density experiences a sharp increase from 1.45-1.50 g/m^3, and steadily increases to 1.52 g/m^3 at 112 cm. No density data was obtained from 113-116 cm.

No magnetic susceptibility data was obtained for the upper 6 cm of Core A. From 7-45 cm, a very weak positive magnetic anomaly is seen. From 45-59 cm, a very weak negative anomaly is seen. From 59-65 cm the anomaly is weakly positive; from 65-73 cm the anomaly is weakly negative. From 73-111 cm the anomaly is weakly positive. No magnetic susceptibility data was obtained from 112-116 cm.

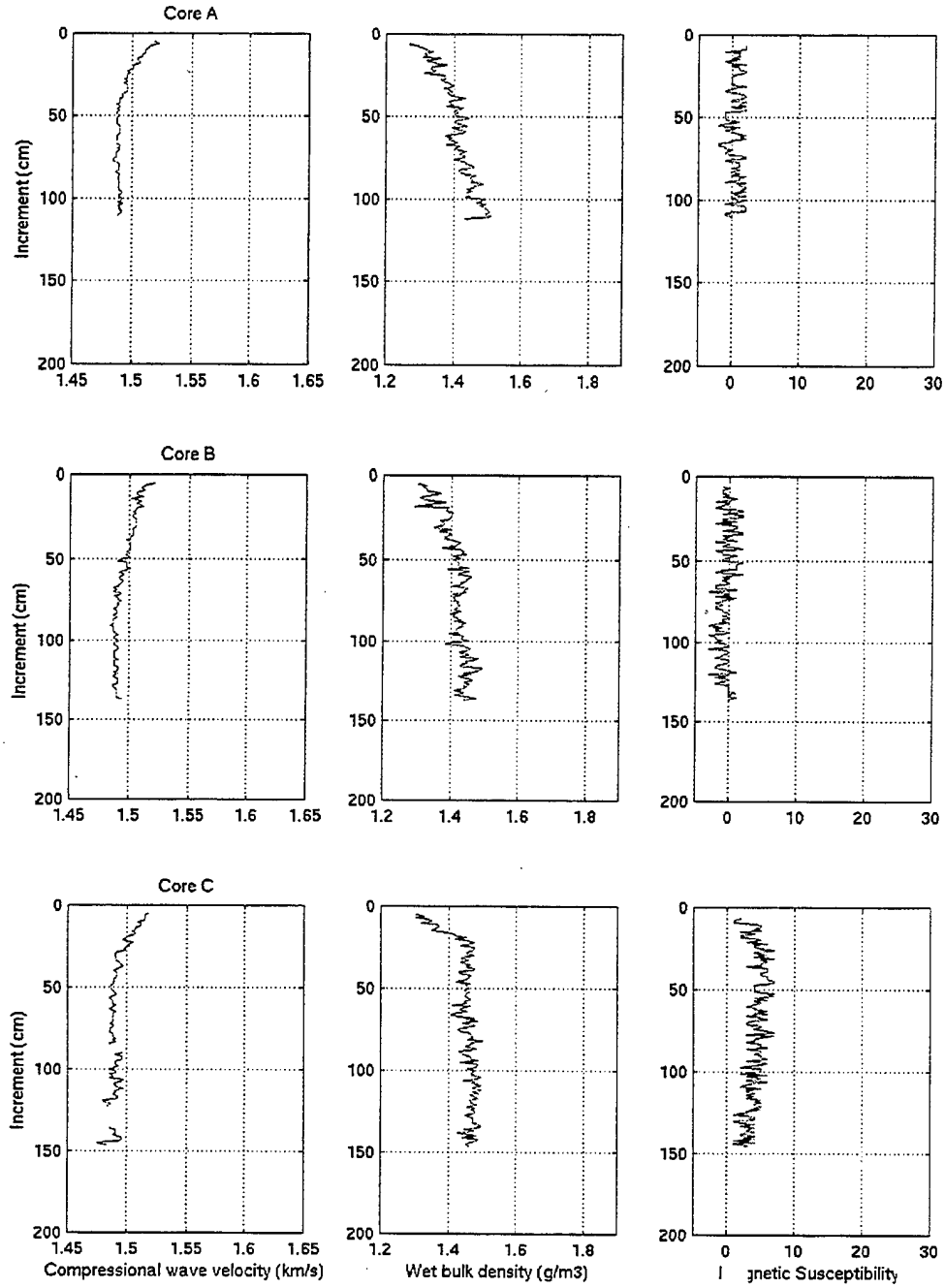

Figure B.1. Laboratory profiles of compressional wave velocity, wet bulk density, and magnetic susceptibility for Cores A-C.

CORE B

Figure B.1 contains laboratory profiles of compressional wave velocity, wet bulk density, and magnetic susceptibility for Core B. No velocity data was obtained for the upper 4 cm of Core B. A steady decrease in Vp is seen from approximately 1.48 km/s at 5 cm to 1.46 km/s at 70 cm. From 70-137 cm, the core shows a relatively unchanged velocity of approximately 1.46 km/s. No velocity data was obtained from 138-142 cm.

No wet bulk density (ρ_b) data was obtained for the upper 4 cm of Core B. A steady increase in the density is seen from 5 cm (1.3 g/m^3) to 61 cm (1.46 g/m^3). From 61-82 cm, the density steadily drops to 1.42 g/m^3; below 82 cm, the density begins to steadily increase, reaching a density of 1.50 g/m^3 at 118 cm. From 118 cm, the density experiences a steady decrease from 1.50-1.43 g/m^3 at the bottom of the core. No density data was obtained from 138-142 cm.

No magnetic susceptibility data was obtained for the upper 5 cm. A very weak negative anomaly is seen from 6-20 cm. From 20-60 cm, the anomaly is weakly positive. From 60-130 cm, the anomaly is weakly negative. From 130-136 cm the anomaly is very weakly positive. No magnetic susceptibility data was obtained from 137-142 cm.

CORE C

Figure B.1 contains laboratory profiles of compressional wave velocity, wet bulk density, and magnetic susceptibility for Core C. No velocity data was obtained for the upper 4 cm of Core C. A steady decrease in Vp is noted from 5 cm (1.48 km/s) to 40 cm (1.45 km/s). From 40-84 cm the velocity remains relatively constant at 1.45 km/s. No velocity data was obtained from 85-89 cm. From 89-104 cm the velocity steadily decreases from 1.46 km/s to 1.45 km/s. At 104 cm the velocity sharply increases to 1.46

km/s, and remains at approximately 1.46 km/s to 1118 cm, where it drops off sharply to 1.45 km/s at 122 cm. No velocity data was obtained from 123-135 cm. From 135-145 cm the velocity steadily increases from 1.45 km/s to 1.46 km/s, then drops off sharply to 1.43 km/s at 146 cm. No velocity data was obtained from 147-151 cm.

No wet bulk density data was obtained for the upper 4 cm of Core C. A steady increase in density is seen from 5 cm (1.31 g/m^3) to 21 cm (1.48 g/m^3). From 21-66 cm the density slowly decreases from 1.48 g/m^3 to 1.47 g/m^3. From 66-95 cm the density repeatedly fluctuates between 1.41 g/m^3 and 1.5 g/m^3. From 95-147 cm the density slowly decreases from 1.5 g/m^3 to 1.48 g/m^3. No density data was obtained from 147-151 cm.

No magnetic susceptibility data was obtained for the upper 6 cm of Core C. From 6-35 cm the anomaly was positive, and increased steadily from +2 to +7. From 35-51 cm the anomaly fluctuated between +3 and +7. From 51-75 cm the anomaly was positive and decreased steadily from +7 to +4. From 75-78 cm the positive anomaly increases rapidly from +4 to +7. From 78-146 cm the positive anomaly slowly decreases from +7 to +3. No magnetic susceptibility data was obtained from 146-151 cm.

CORE D

Figure B.2 contains laboratory profiles of compressional wave velocity, wet bulk density, and magnetic susceptibility for Core D. No velocity data was obtained for the upper 4 cm of Core D. From 4-33 cm the velocity decreases from 1.48 km/s to 1.46 km/s. From 33-84 cm the velocity slowly increases to 1.48 km/s. From 84-95 cm the velocity drops off rapidly to 1.46 km/s. From 95-120 cm the velocity increases to 1.48 km/s. No velocity data was obtained from 120-122 cm. From 122-125 cm the velocity

increases rapidly from 1.44 km/s to 1.47 km/s. No velocity data was obtained from 125-129 cm.

No density data was obtained for the upper 4 cm of Core D. From 4-30 cm the density steadily increases from 1.42 g/m³ to 1.59 g/m³. From 30-33 cm the density drops off rapidly to 1.52 g/m³. From 33-83 cm the density steadily increases to 1.65 g/m³. From 83-95 cm the density drops off sharply to 1.5 g/m³. From 95-113 cm the density increases to 1.67 g/m³. From 113-119 the density drops off sharply to 1.6 g/m³. The density data from 119-120 cm is bad data. No density data was obtained from 120-122 cm. The density data from 122-127 cm is bad data. No density data was obtained from 127-129 cm.

No magnetic susceptibility data was obtained for the upper 6 cm of Core D. From 6-28 cm the anomaly increases from +3 to +7. From 28-44 cm the positive anomaly remains relatively constant at +7. From 44-74 cm the anomaly decreases slowly from +7 to +5. From 74-76 cm the anomaly increases rapidly from +5 to +7. From 76-124 cm the anomaly steadily decreases to +2. No magnetic susceptibility data was obtained from 124-129 cm.

CORE E

Figure B.2 contains laboratory profiles of compressional wave velocity, wet bulk density, and magnetic susceptibility for Core E. No velocity data was obtained for the upper 7 cm of Core E. From 7-12 cm the velocity remains relatively constant at 1.48 km/s. No velocity data was obtained from 12-14 cm. From 14-31 cm the velocity steadily decreases from 1.48 km/s to 1.45 km/s. From 31-42 cm the velocity remains relatively constant at 1.45 km/s. From 42-44 cm the velocity drops sharply to 1.44 km/s.

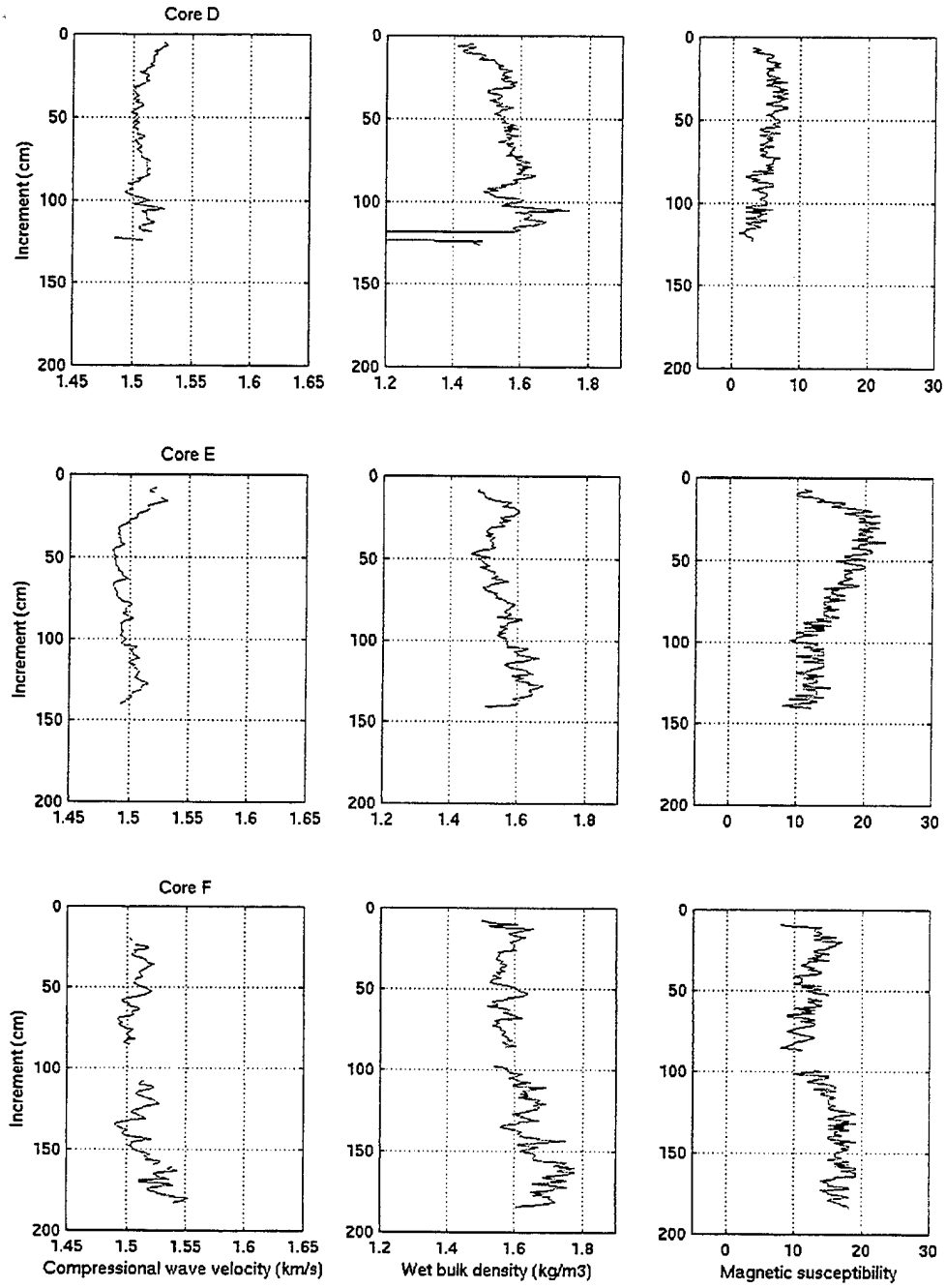

Figure B.2. Laboratory profiles of compressional wave velocity, wet bulk density, and magnetic susceptibility for Cores D-F.

From 44-63 cm the velocity steadily increases to 1.46 km/s. From 63-65 cm the velocity drops sharply to 1.44 km/s. From 65-76 cm the velocity slowly increases to 1.45 km/s. At 76 cm the velocity increases sharply to 1.47 km/s and remains relatively constant at that value until 88 cm. At 88 cm the velocity drops sharply to 1.45 km/s and remains relatively constant until 103 cm. At 103 cm the velocity increases rapidly to 1.47 km/s and increases to 1.48 km/s at 128 cm. From 128-141 cm the velocity steadily decreases to 1.45 km/s. No velocity data was obtained from 141-147 cm.

No density data was obtained for the upper 7 cm of Core E. From 7-21 cm the density steadily increases from 1.49 g/m^3 to 1.61 g/m^3. From 21-55 cm the density decreases to 1.48 g/m^3. From 55-63 cm the density increases to 1.59 g/m^3. From 63-68 cm the density drops rapidly to 1.5 g/m^3. From 68-79 cm the density steadily increases to 1.6 g/m^3. From 79-95 cm the density decreases to 1.57 g/m^3. From 95-112 cm the density increases to 1.63 g/m^3. From 112-114 cm the density drops rapidly to 1.58 g/m^3. From 114-121 cm the density increases to 1.62 g/m^3 before dropping sharply off to 1.6 g/m^3 from 121-124 cm. From 124-128 cm the density increases to 1.68 g/m^3. From 128-138 cm the density decreases to 1.61 g/m^3. No density data was obtained for 138 cm. The data from 139-142 cm is bad data. No density data was obtained from 142-147 cm.

No magnetic susceptibility data was obtained for the upper 6 cm of Core E. From 6-23 cm the anomaly increases from +10 to +22. From 23-99 cm the anomaly slowly decreases to +10. From 99-102 cm the anomaly increases to +12 and remains relatively constant at +12 to 142 cm. No magnetic susceptibility data was obtained from 142-147 cm.

CORE F

Figure B.2 contains laboratory profiles of compressional wave velocity, wet bulk density, and magnetic susceptibility for Core F. No velocity data was obtained for the upper 19 cm of Core F. From 20-22 cm the velocity remains steady at 1.46 km/s. No velocity data was obtained from 22-24 cm. From 24-27 cm the velocity increases to from 1.46 km/s to 1.47 km/s, then drops back down to 1.46 km/s at30 cm. From 30-35 cm the velocity increases to 1.48 km/s, then slowly drops back down to 1.47 km/s at 48 cm. From 48-50 cm the velocity increases to 1.48 km/s, then drops sharply to 1.45 km/s at 58 cm. From 58-63 cm the velocity increases to 1.47 km/s, then drops to 1.45 km/s at 68 cm, and remains near 1.45 km/s until 73 cm. From 73-75 cm the velocity increases to 1.46 km/s and remains near 1.46 km/s until 87 cm. No velocity data was obtained from 87-107 cm. From 107-112 cm the velocity increases from 1.47-1.48 km/s, then drops back down to 1.47 km/s at 115 cm. From 115-122 cm the velocity increases to 1.48 km/s, then drops sharply to 1.46 km/s at 128 cm. From 128-131 cm the velocity increases to 1.47 km/s, then drops sharply to 1.45 km/s at 136 cm. From 136-141 cm the velocity shows a very slight increase in speed, and then spikes to 1.48 km/s from 141-143 cm. From 143-146 cm the velocity decreases to 1.46 km/s. From 146-160 cm the velocity steadily increases to 1.48 km/s. No velocity data was obtained for 160 cm. From 161-163 cm the velocity drops from 1.5 km/s to 1.48 km/s, then increases to 1.49 km/s at 172 cm. From 172-173 cm the velocity drops off sharply to 1.47 km/s, then steadily increases to 1.51 km/s at 180 cm. From 180-184 cm the velocity decreases to 1.49 km/s. No velocity data was obtained from 184-189 cm.

No density data was obtained for the upper 7 cm of Core F. From 7-12 cm, the density increases from 1.5-1.65 g/m³. From 12-44 cm the density decreases to 1.54 g/m³. From 44-54 cm the density steadily increases to 1.63 g/m³, then steadily decreases to 1.57 g/m³ at 61 cm. From 61-67 cm the density increases to 1.62 g/m³, then drops off sharply to 1.56 g/m³ at 69 cm. From 69-87 cm the density steadily increases to 1.61 g/m³. No density data was obtained from 87-97 cm. From 97-125 cm the density increases from 1.55 g/m³ to 1.69 g/m³. From 125-127 cm the density drops off sharply to 1.6 g/m³, then increases rapidly to 1.67 g/m³ at 130 cm. From 130-134 cm the density drops off sharply to 1.58 g/m³, then increases to 1.76 g/m³ at 143 cm, where it again drops off sharply to 1.64 g/m³ at 145 cm. From 145-156 cm the density remains around 1.64 g/m³, and then sharply increases to 1.79 g/m³ at 160 cm. From 160-175 cm the density decreases to 1.69 g/m³. From 175-182 cm the density increases to 1.72 g/m³, and then drops off sharply to 1.61 g/m³ at 185 cm. No density data was obtained from 186-189 cm.

No magnetic susceptibility data was obtained for the upper 8 cm of Core F. From 8-20 cm the anomaly increases from +7 to +17. From 20-44 cm the anomaly decreases to +11. From 44-54 cm the anomaly increases to +15. No magnetic susceptibility was obtained for 54 cm. From 55-88 cm the anomaly slowly decreases to +11. No magnetic susceptibility data was obtained from 88-98 cm. From 98-121 cm the anomaly increases from +13 to +16. From 121-123 cm the anomaly increases sharply to +19, then slowly decreases to +18 at 137 cm, before dropping off sharply to +16 at 142 cm. From 142-144 cm the anomaly increases sharply to +19, then decreases slowly to +17 at 154 cm. From 154-160 cm the anomaly increases to +19 and remains at +19 to 164 cm. From 164-169 cm the anomaly drops off sharply to +14. From 169-171 cm the anomaly increases

sharply to +18, and remains at +18 until 185 cm. No magnetic susceptibility data was obtained from 185-189 cm.

CORE G

Figure B.3 contains laboratory profiles of compressional wave velocity, wet bulk density, and magnetic susceptibility for Core G. No velocity data was obtained for the upper 21 cm of Core G. From 21-38 cm the velocity decreases from 1.56 km/s to 1.51 km/s. From 38-45 cm the velocity increases to 1.54 km/s. No velocity data was obtained from 45-51 cm.

No density data was obtained for the upper 7 cm of Core G. From 7-14 cm the density decreases from 1.76 g/m^3 to 1.71 g/m^3. From 14-17 cm the density increases sharply to 1.76 g/m^3. From 17-20 cm the density decreases sharply to 1.69 g/m^3 before increasing sharply to 1.86 g/m^3 at 30 cm. From 30-34 cm the density decreases sharply to 1.78 g/m^3. From 34-43 cm the density decreases slowly to 1.75 g/m^3. From 43-45 cm the density increases rapidly to 1.87 g/m^3, then drops rapidly to 1.77 g/m^3 at 47 cm. No density data was obtained from 48-51 cm.

No magnetic susceptibility data was obtained for the upper 7 cm of Core G. From 7-23 cm the anomaly increases from +8 to +17. From 23-26 cm the anomaly decreases to +15, then increases to +20 at 27 cm. From 27-37 cm the anomaly increases to +22. From 37-48 cm the anomaly decreases slowly to +20. No magnetic susceptibility data was obtained from 48-51 cm.

CORE H

Figure B.3 contains laboratory profiles of compressional wave velocity, wet bulk density, and magnetic susceptibility for Core H. No velocity data was obtained for the

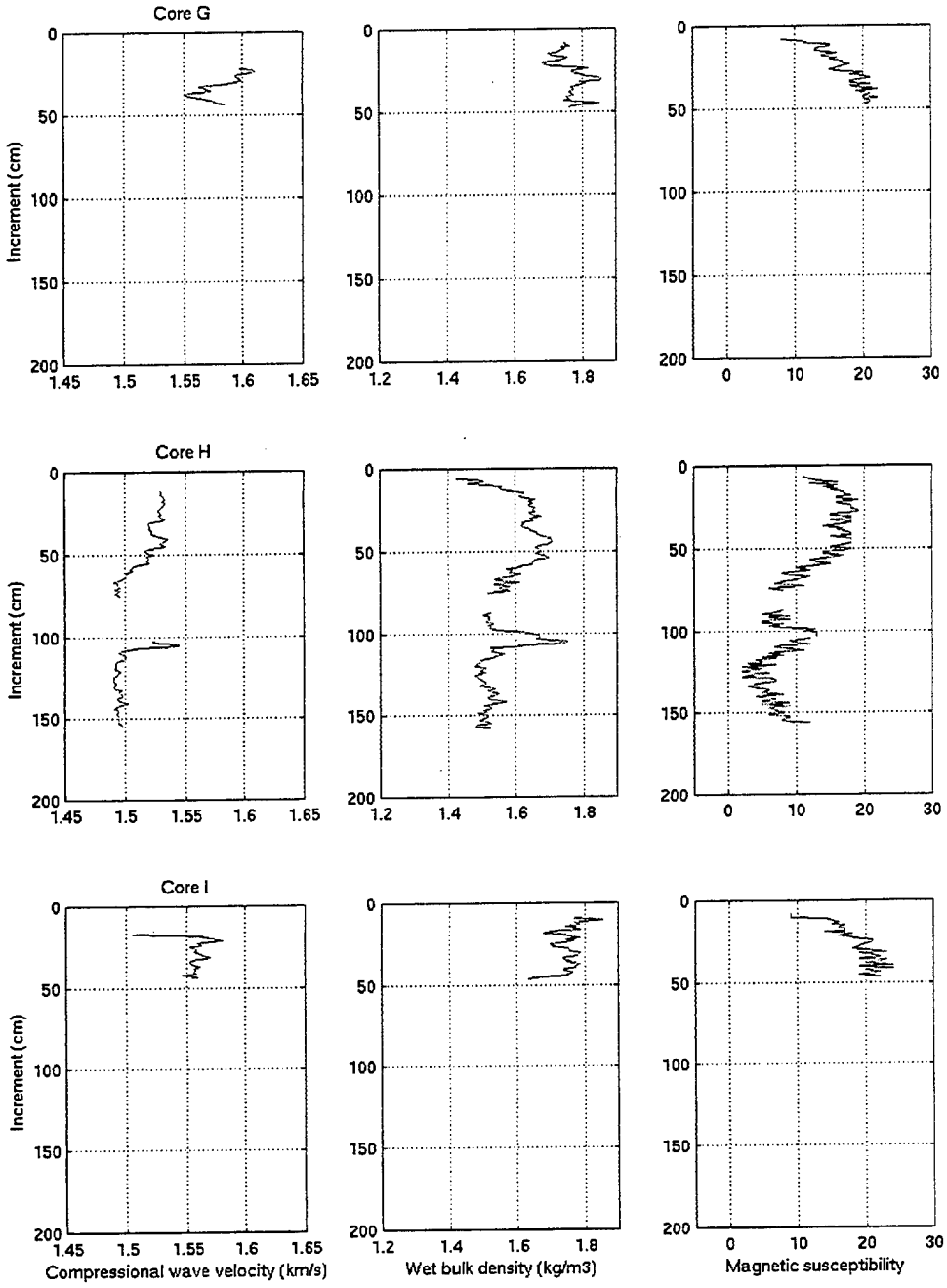

Figure B.3. Laboratory profiles of compressional wave velocity, wet bulk density, and magnetic susceptibility for Cores G-I.

upper 11 cm of Core H. From 11-29 cm the velocity remains relatively constant at 1.48 km/s. From 29-32 cm the velocity drops off sharply to 1.46 km/s, where it remains at 1.46 km/s until 38 cm. From 38-41 cm the velocity increases to 1.48 km/s, then steadily decreases to 1.45 km/s at 65 cm. From 65-76 cm the velocity remains relatively constant at 1.45 km/s. No velocity data was obtained from 76-102 cm. From 102-105 cm the velocity increases rapidly from 1.47 km/s to 1.49 km/s, then decreases rapidly to 1.45 km/s at 110 cm. The velocity increases to 1.46 km/s from 110-114 cm , then decreases to 1.445 km/s at 127 cm and remains relatively constant until 136 cm. At 136 cm the velocity increases slightly to 1.45 km/s and remains constant until 140 cm, where it increases slightly to 1.46 km/s. From 140-142 cm the velocity decreases to 1.45 km/s and remains constant until 156 cm. No velocity data was obtained from 156-162 cm.

No density data was obtained for the upper 5 cm of Core H. From 5-19 cm the density increases steadily from 1.42 g/m^3 to 1.64 g/m^3. From 19-29 cm the density increases slowly to 1.68 g/m^3. From 29-35 cm the density decreases to 1.62 g/m^3 before increasing steadily to 1.69 g/m^3 at 44 cm. From 44-58 cm the density decreases slowly to 1.65 g/m^3. From 58-61 cm the density drops rapidly to 1.58 g/m^3. From 61-76 cm the density slowly decreases to 1.56 g/m^3. No density data was obtained from 76-87 cm. From 88-97 cm the density slowly increases from 1.53 g/m^3 to 1.55 g/m^3. From 97-105 cm the density increases drastically to 1.77 g/m^3, and then decreases drastically to 1.49 g/m^3 at 120 cm. From 120-142 cm the density slowly increases to 1.58 g/m^3, before dropping off sharply to 1.52 g/m^3 at 144 cm. From 144-159 cm the density decreases slowly to 1.51 g/m^3. No density data was obtained from 159-162 cm.

No magnetic susceptibility data was obtained for the upper 6 cm of Core H. From 6-21 cm the anomaly increases from +11 to +19. From 21-53 cm the anomaly decreases slowly to +18. No magnetic susceptibility data was obtained for 46 cm. From 53 to 76 cm the anomaly decreases steadily to +8. No magnetic susceptibility data was obtained from 76-87 cm. From 87-96 cm the anomaly remains relatively constant at +9, then increases sharply to +12 at 99 cm and remains at +12 until 104 cm. No magnetic susceptibility data was obtained for 104 cm. From 105-128 cm the anomaly decreases from +11 to +3. From 128-157 cm the anomaly slowly increases to +11. No magnetic susceptibility data was obtained from 157-162 cm.

CORE I

Figure B.3 contains laboratory profiles of compressional wave velocity, wet bulk density, and magnetic susceptibility for Core I. No velocity data was obtained for the upper 14 cm of Core I. The data at 15 cm is bad data. No velocity data was obtained for 16 cm. The data from 17-19 cm is bad data. From 19-21 cm the velocity increases sharply from 1.52 km/s to 1.54 km/s before dropping off sharply to 1.52 km/s at 23 cm. From 23-27 cm the velocity slowly decreases to 1.51 km/s. From 27-29 cm the velocity increases to 1.53 km/s, then drops off to 1.51 km/s at 33 cm. From 33-36 cm the velocity increases to 1.52 km/s. From 36-41 cm the velocity remains relatively constant at 1.52 km/s. From 41-42 cm the velocity decreases to 1.5 km/s, and then increases to 1.52 km/s at 44 cm. No velocity data was obtained from 45-51 cm.

No density data was obtained for the upper 8 cm of Core I. From 8-18 cm the density decreases rapidly from 1.86 g/m^3 to 1.69 g/m^3. From 19-21 cm the density increases sharply to 1.79 g/m^3, then decreases to 1.71 at 25 cm. From 25-31 cm the

density increases to 1.79 g/m^3 , and then decreases to 1.75 g/m^3 at 36 cm. From 36-38 cm the density increases to 1.79 g/m^3, and then steadily decreases to 1.76 g/m^3 at 45 cm. The data from 45-47 cm is bad data. No density data was obtained from 47-51 cm.

No magnetic susceptibility data was obtained for the upper 7 cm of Core I. From 7-12 cm the anomaly increases moderately from +9 to +15. From 12-23 cm the anomaly increases slowly to +18. From 23-25 cm the anomaly increases to +21, then steadily decreases to +18 at 28 cm. From 28-32 cm the anomaly increases to +22 and remains relatively constant until 44 cm, where it drops off to +20 at 45. From 45-47 cm the anomaly increases to +22. No magnetic susceptibility data was obtained from 47-51 cm.

CORE J

Core J was not analyzed for acoustic information due to the extensive deformation that occurred during recovery of the core.

CORE K

Core K was not analyzed for acoustic information due to the extensive deformation that occurred during recovery of the core.

APPENDIX C – CONVERSION OF ACOUSTIC PARAMETERS OF SEDIMENT FROM LABORATORY VALUES TO *IN-SITU* VALUES

A. COMPRESSIONAL WAVE VELOCITY

From the physical analysis and description of the sediment, all cores were determined to be from the continental terrace/continental slope, in accordance with Hamilton (1971). The first value to be determined is the velocity ratio. It is assumed that the water salinity and temperature immediately adjacent to the top of the sediment is the same as the pore water within the sediment. Salinities and temperatures for this study were taken from the NAVO cruise in July, 1998, to maintain continuity with work done by Onofre (1999). The velocity ratio is the same for laboratory values (1 atmosphere, 23° C) as for *in-situ* values (Hamilton, 1971). Equation (1) is used to obtain the V_{si}, the velocity of the sediment *in-situ*:

$$V_{si} = \frac{V_{sl}}{V_{wl}} * V_{wi} \qquad (1)$$

Where V_{sl} is the velocity of the sediment in the laboratory, V_{wi} is the velocity of the water *in-situ*, and V_{wl} is the velocity of the sediment in the water. Using the profiles obtained from the multi-sensor sediment core acoustic analysis equipment at the USGS, and the calculations made for velocity in seawater at laboratory values (salinity from July 1998), *in-situ* sediment velocities were obtained for the entire length of the core. Overburden of the sediment was assumed to be negligible (Hamilton, 1976).

B. WET BULK DENSITY

To determine the *in-situ* density of the sediment, the porosity must be determined first. Porosity can be calculated using equation (2), from Hamilton, 1971:

$$P = \frac{(\rho_{sbl} - \rho_{sg})}{(\rho_{wl} - \rho_{sg})} \quad (2)$$

Where P is the porosity, ρ_{sbl} is the wet bulk density of the sediment in the laboratory, ρ_{sg} is the grain density of the sediment, and ρ_{wl} is the density of the seawater in the laboratory. Grain density of the sediment was obtained from table 1 in Hamilton, 1970a. Since porosity does not change from lab values to *in-situ* values (Hamilton, 1971), it can be used in calculations for *in-situ* density. *In-situ* density can be calculated using equation (3), from Hamilton, 1971:

$$\rho_{sbi} = P * \rho_{wi} + (1 - P) * \rho_{sg} \quad (3)$$

Where P is porosity, ρ_{sbi} is sediment *in-situ* wet bulk density, ρ_{wi} is *in-situ* seawater density, and ρ_{sg} is the grain density of the sediment. Since overburden was negligible, the equation was used for the entire sediment profile.

APPENDIX D – DETAILED PHYSICAL DESCRIPTION OF CORES

CORE A

Core A had a total length of 116 cm. Figure D.1 shows the sediment in Core A from 0-60 cm. Figure D.2 shows the sediment in Core A from 60-116 cm. From 0-7 cm, the sediment is composed of poorly consolidated, homogeneous, olive-green fine-grained mud. From 7-17 cm, the sediment maintains its color, homogeneity, and grain size, but is moderately consolidated. The remainder of the core (17-116 cm) is composed of well-consolidated, homogeneous, fine-grained olive-green mud. Grain-size analysis samples were taken from 23-25 cm, 43-47 cm, 73-77 cm, 93-97 cm, and 100-104 cm. Carbon-14 samples were taken from 15-19 cm and 80-85 cm. A sample of sediment from 5-8 cm was taken for DDT analysis.

CORE B

Core B had a total length of 141 cm. Figure D.3 shows the sediment in Core B from 0-60 cm. Figure D.4 shows the sediment in Core B from 60-120 cm. Figure D.5 shows the sediment in Core B from 110-141 cm. From 0-4 cm, the sediment is composed of poorly consolidated, homogeneous, fine-grained olive-green mud. From 4-8 cm, the sediment maintains its color, grain size, and homogeneity, but is moderately consolidated. The remainder of the core (8-141 cm) is composed of well-consolidated, homogeneous, fine-grained olive-green mud, with some variations. A possible worm burrow is located at 18 cm. Bands of sediment that exhibit a darker color of green than typically found but maintain the same grain size exist from 25-55 cm, 60-69 cm, and 72-77 cm. From 78-135 cm, the olive-green mud is interspersed with darker splotches but shows no change in grain size, which may indicate bioturbation. Grain-size analysis

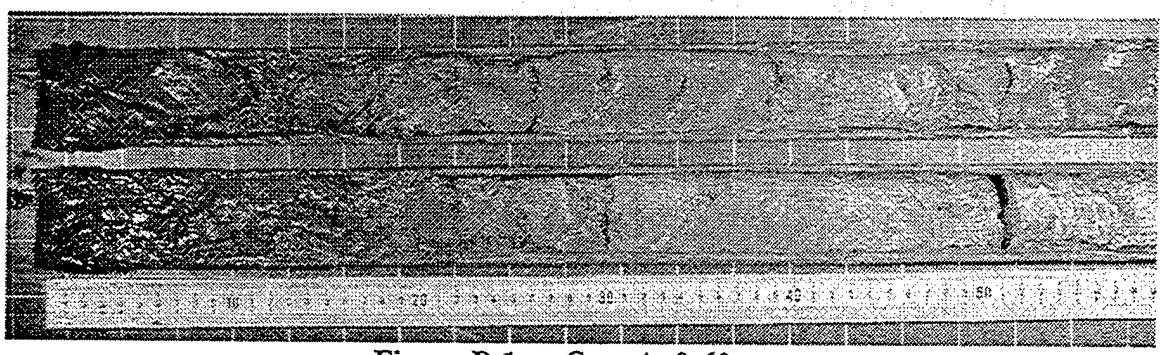

Figure D.1. Core A, 0-60 cm.

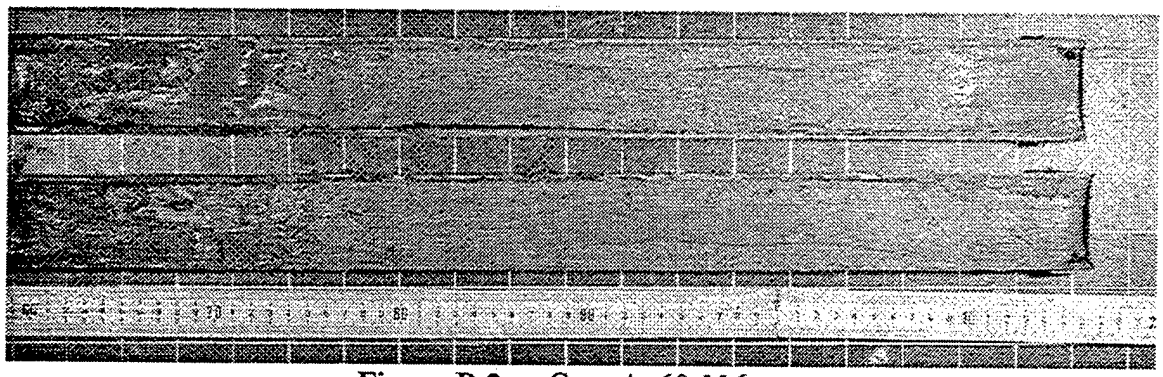

Figure D.2. Core A, 60-116 cm.

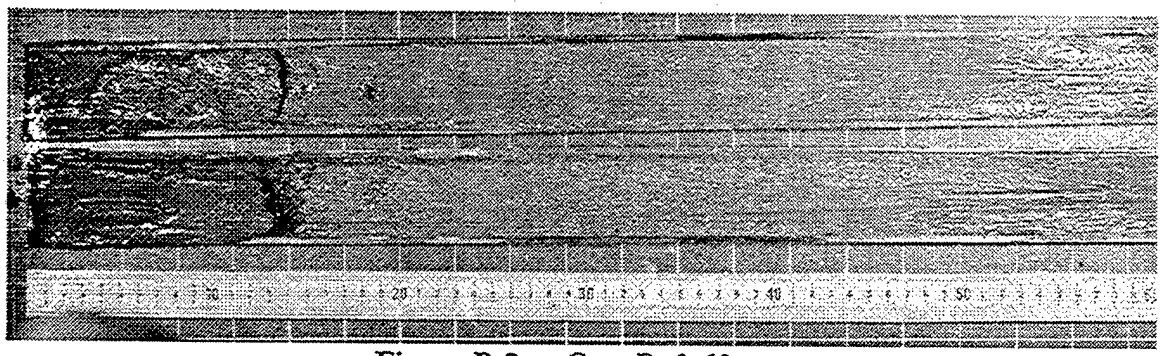

Figure D.3. Core B, 0-60 cm.

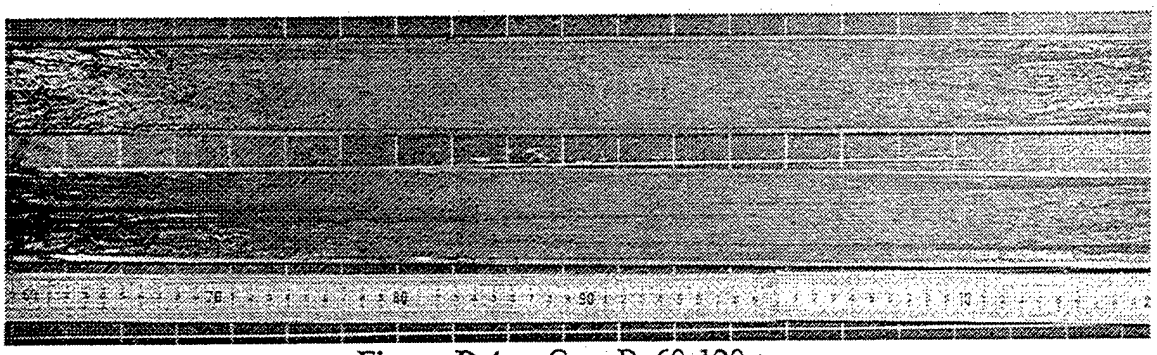

Figure D.4. Core B, 60-120 cm.

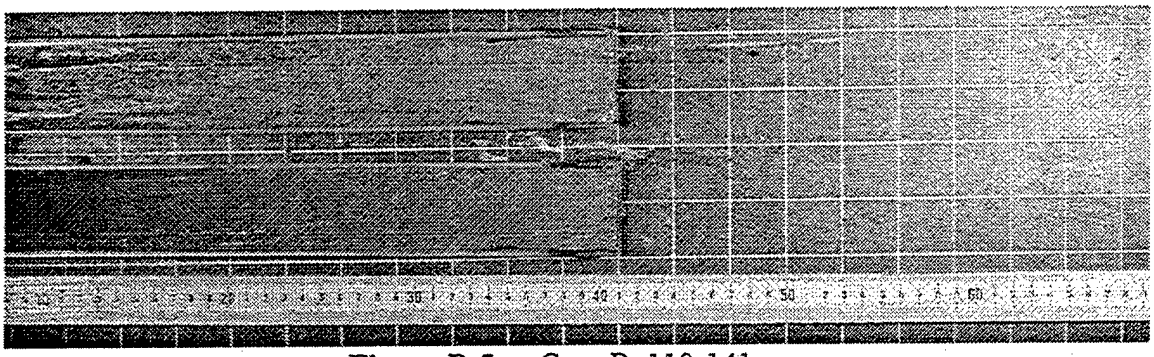

Figure D.5. Core B, 110-141 cm.

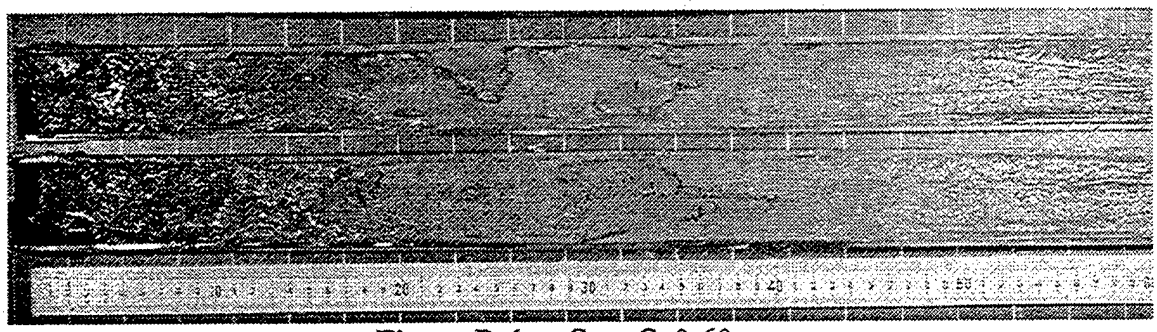

Figure D.6. Core C, 0-60 cm.

samples were taken from 18-22 cm, 43-47 cm, 78-82 cm, and 108-112 cm. Carbon-14 samples were taken from 27-32 cm and from 110-5 cm. A sample of sediment from 5-10 cm was taken for DDT analysis.

CORE C

Core C had a total length of 148 cm. Figure D.6 shows the sediment in Core C from 0-60 cm. Figure D.7 shows the sediment in Core C from 60-120 cm. Figure D.8 shows the sediment in Core C from 110-148 cm. From 0-3 cm, the sediment is composed of poorly consolidated, homogeneous, fine-grained dark-green mud. From 3-9 cm, the sediment maintains its color, grain size, and homogeneity, but is moderately consolidated. From 9-18 cm core is composed of well-consolidated, homogeneous, fine-grained dark-green mud. From 18-24 cm, the sediment is well-consolidated, homogeneous, fine-grained olive-green mud with dark-green splotches interspersed. The remainder of the core (24-148 cm) is composed of well-consolidated, homogeneous, fine-grained olive-green mud. Small shell fragments were found at 98 cm, 111 cm, and 120 cm. Grain-size analysis samples were taken from 10-14 cm, 43-47 cm, 78-82 cm, and 123-127 cm. A sample of sediment from 2-11 cm was taken for DDT analysis.

CORE D

Core D had a total length of 128 cm. Figure D.9 shows the sediment in Core D from 0-60 cm. Figure D.10 shows the sediment in Core D from 60-120 cm. Figure D.11 shows the sediment in Core D from 110-128 cm. From 0-91 cm, the sediment is composed of well-consolidated, homogeneous, fine-grained olive-green mud. From 91-104 cm, the sediment is well consolidated, homogeneous, fine-grained mud, with a mottled dark-green color found around lighter green striations, which may indicate

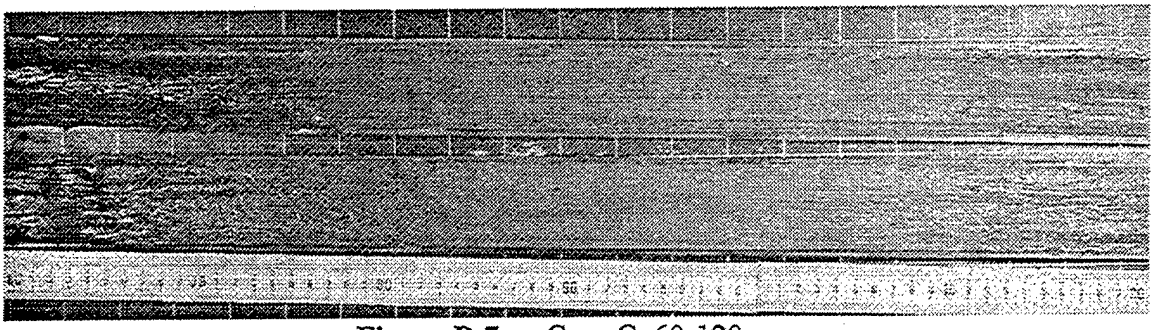

Figure D.7. Core C, 60-120 cm.

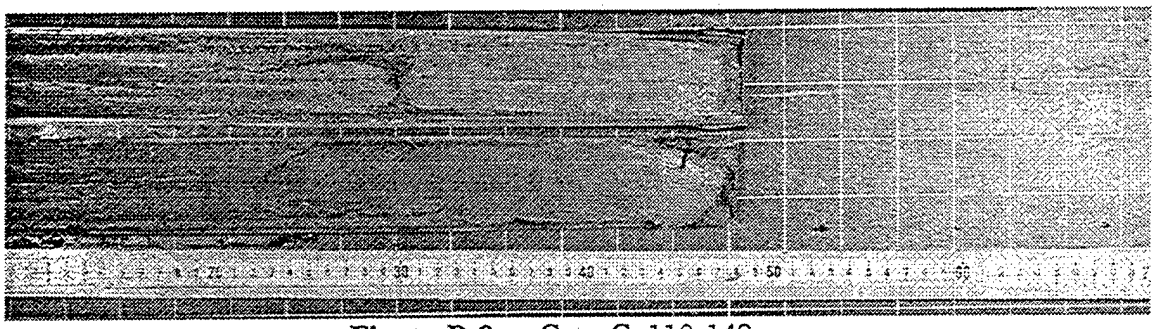

Figure D.8. Core C, 110-148 cm.

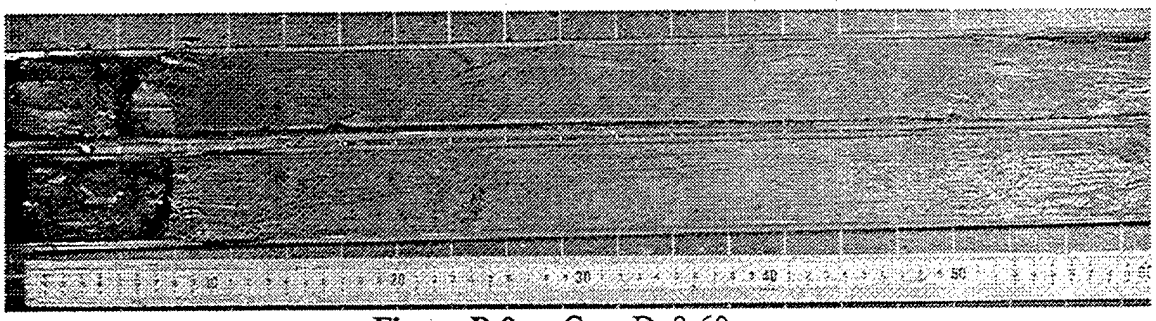

Figure D.9. Core D, 0-60 cm.

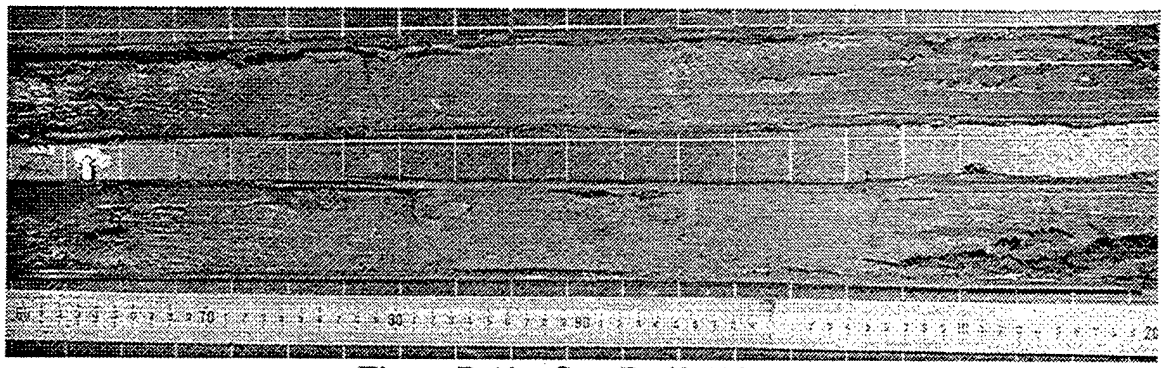

Figure D.10. Core D, 60-120 cm.

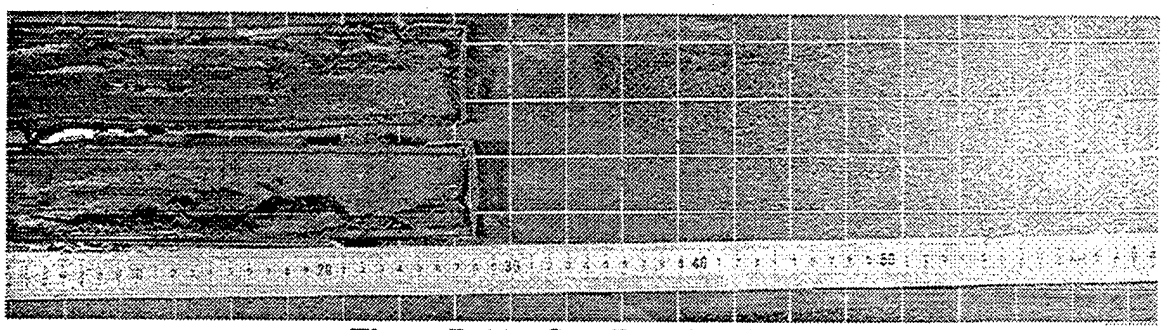

Figure D.11. Core D, 110-128 cm.

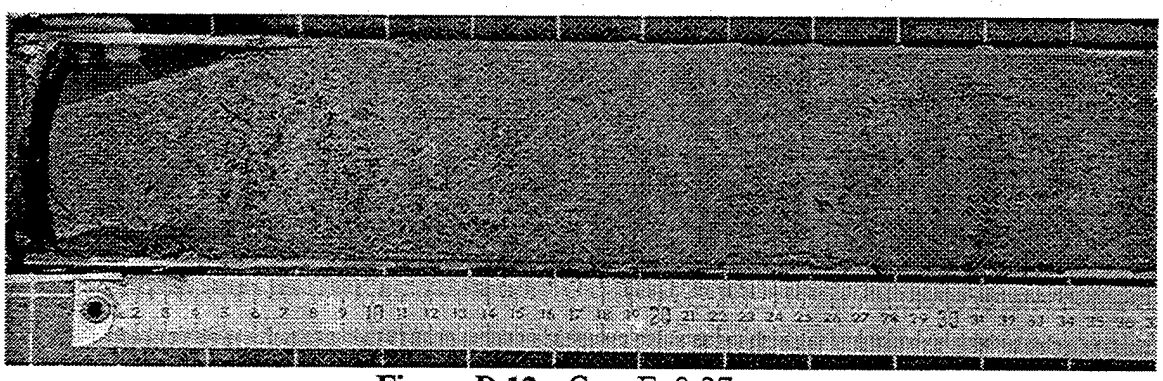

Figure D.12. Core E, 0-37 cm.

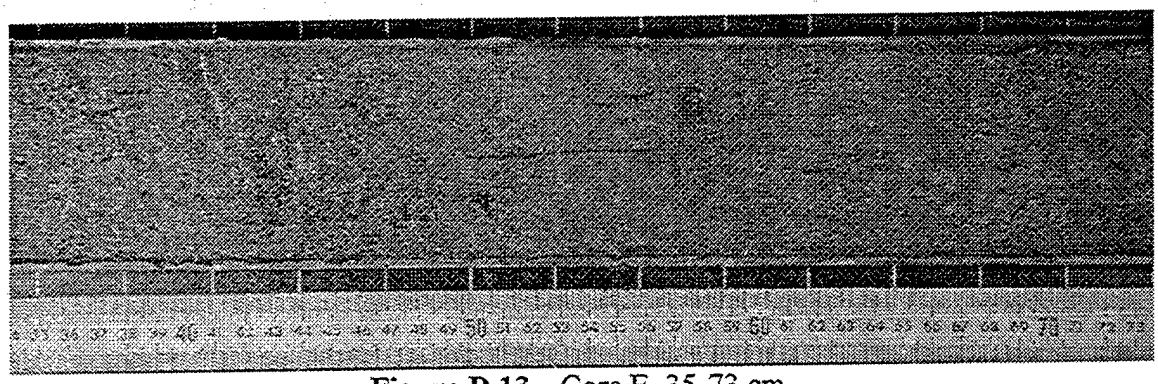

Figure D.13. Core E, 35-73 cm.

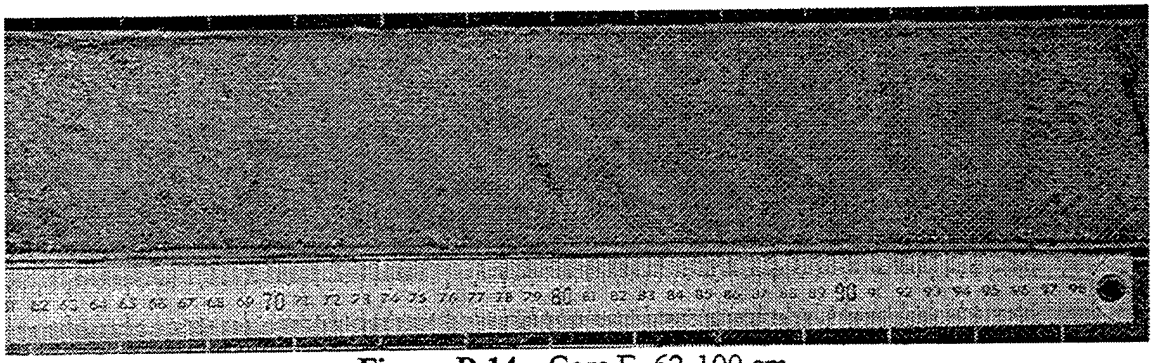

Figure D.14. Core E, 62-100 cm.

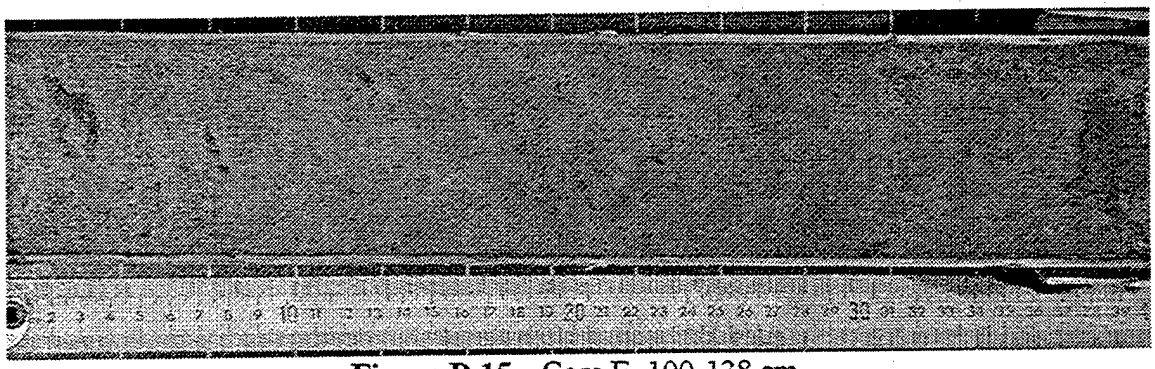

Figure D.15. Core E, 100-138 cm.

bioturbation. From 104 cm to 106 cm, the sediment is well-consolidated, homogeneous, fine-grained dark-green mud that shows evidence of bioturbation. From 106-120 cm, the sediment is well-consolidated, homogenous, fine-grained dark-green mud. Possible bioturbation may have occurred at 114 cm. Grain-size analysis samples were taken from 28-31 cm, 58-62 cm, 82-86 cm, 92-95 cm, 98-102 cm, 104-106 cm, and 114-118 cm.

CORE E

Core E had a total length of 146 cm. Figure D.12 shows the sediment in Core E from 0-37 cm. Figure D.13 shows the sediment in Core E from 35-73 cm. Figure D.14 shows the sediment in Core E from 62-100 cm. Figure D.15 shows the sediment in Core E from 100-146 cm. From 0-18 cm the sediment is composed of well-consolidated, homogeneous, dark-green fine-grained mud. From 18-34 cm the sediment is composed of well-consolidated, homogenous, olive-green fine-grained mud with dark-green splotches interspersed. From 34-120 cm the sediment is composed of well-consolidated, homogeneous, olive-green fine-grained mud with possible bioturbation occurring at 41 cm, 51 cm, 59 cm, 83 cm, 86 cm, 103 cm, 109-111 cm, 114 cm, and 120 cm. From 120-135 cm the sediment is composed of well-consolidated, homogeneous, dark-green fine-grained mud with small olive-green splotches interspersed. From 135-146 cm the sediment is composed of well-consolidated homogenous, olive-green fine-grained mud with small dark-green splotches interspersed. Grain-size analysis samples were taken from 14-16 cm, 38-42 cm, 48-52 cm, 68-72 cm, 78-82 cm, 108-112 cm, and 125-127 cm. A sample from 2-5 cm was taken for DDT analysis.

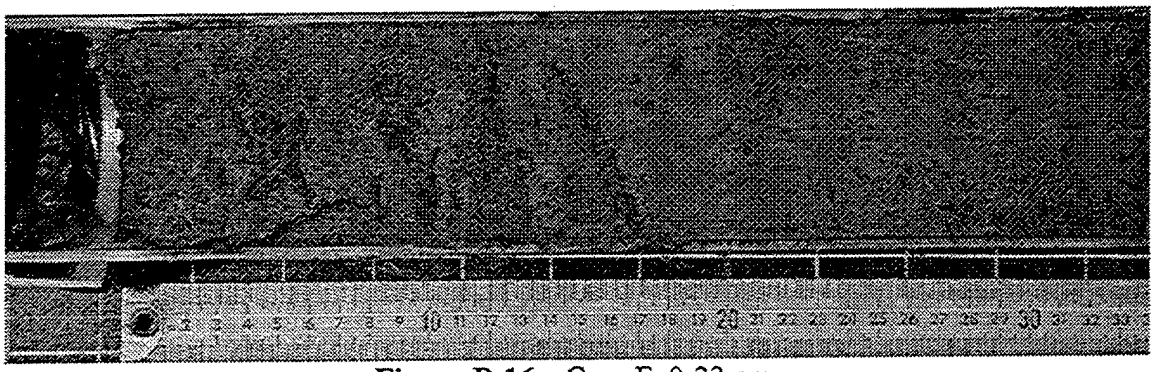

Figure D.16. Core F, 0-33 cm.

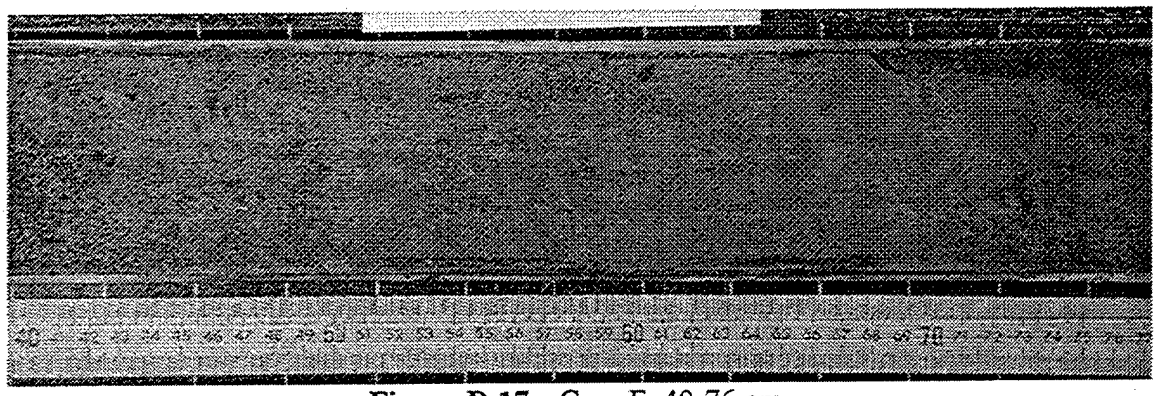

Figure D.17. Core F, 40-76 cm.

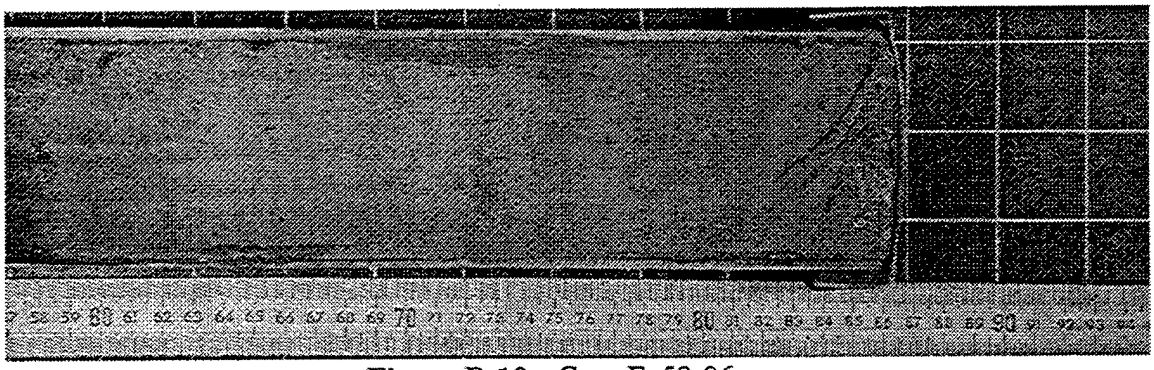

Figure D.18. Core F, 58-86 cm.

CORE F

Core F had a total length of 187 cm. Figure D.16 shows the sediment in Core F from 0-33 cm. Figure D.17 shows the sediment in Core F from 40-76 cm. Figure D.18 shows the sediment in Core F from 58-86 cm. Figure D.19 shows the sediment in Core F from 86-146 cm. Figure D.20 shows the sediment in Core F from 146-187 cm. From 0-22 cm the sediment is composed of moderately consolidated olive-green fine-grained mud, with large lens-shaped glauconite concentrations interspersed at 5 cm, 10 cm, 12 cm, 15-17 cm, and a large round glauconite concentration at 20-22 cm. From 22-146 cm, the sediment is composed of well-consolidated, homogeneous, olive-green fine-grained mud, with one small circular glauconite concentration at 61 cm and a small splotchy glauconite concentration at 120 cm. From 146-187 cm, the sediment is composed of well-consolidated, homogeneous, dark-green fine-grained mud with a numerous glauconite concentrations: a small, splotchy concentration at 147 cm, a moderate lens-shaped concentration at 154 cm, a small circular concentration at 155 cm, a large lens-shaped concentration at 157 cm, a large splotchy concentration at 162-163 cm, a small concentration at 166 cm, and a large circular concentration at 168-170 cm. Grain-size analysis samples were taken from 10-14 cm, 24-28 cm, 43-47 cm, 63-67 cm, 70-74 cm, 115-119 cm, 133-137 cm, 153-157 cm, and 171-175 cm. A sample from 3-7 cm was taken for DDT analysis.

CORE G

Core G had a total length of 46 cm. Figure D.21 shows the sediment in Core G from 0-46 cm. Figures D.22 and D.23 are closer views of the sediment, that show the coarser texture and glauconite concentrations. From 0-4 cm the sediment was composed

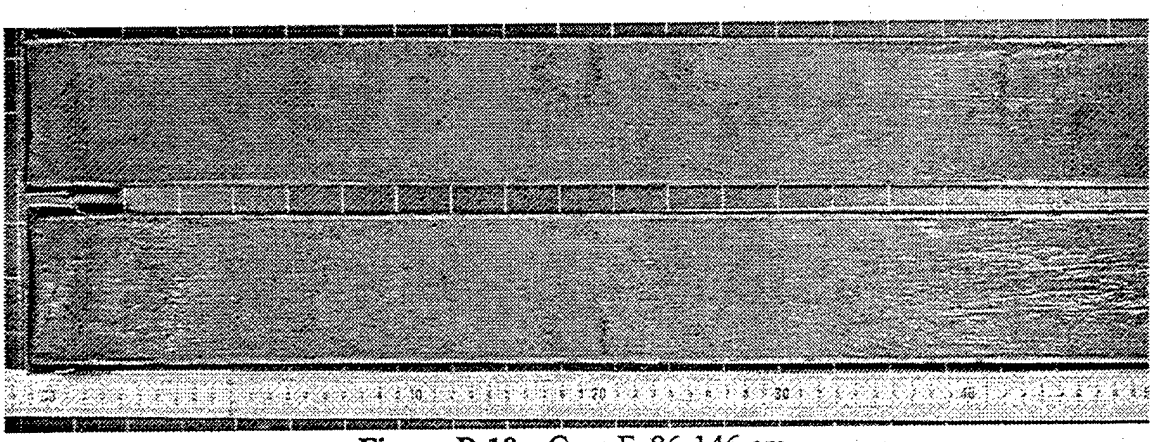

Figure D.19. Core F, 86-146 cm.

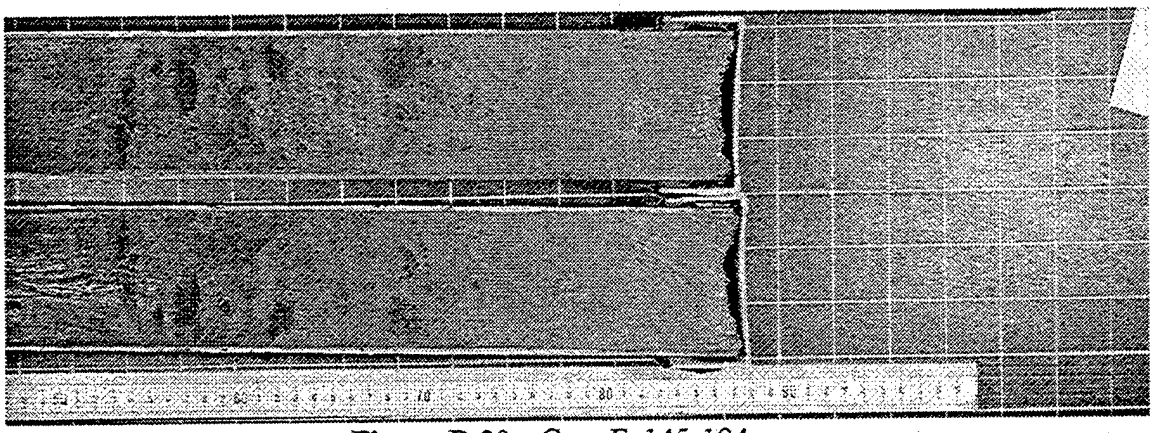

Figure D.20. Core F, 145-184 cm.

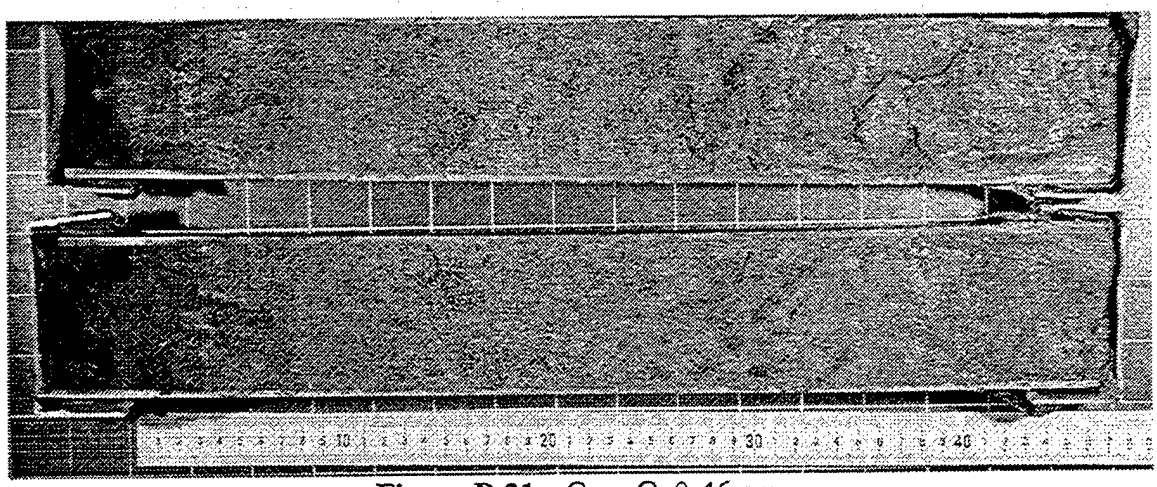

Figure D.21. Core G, 0-46 cm.

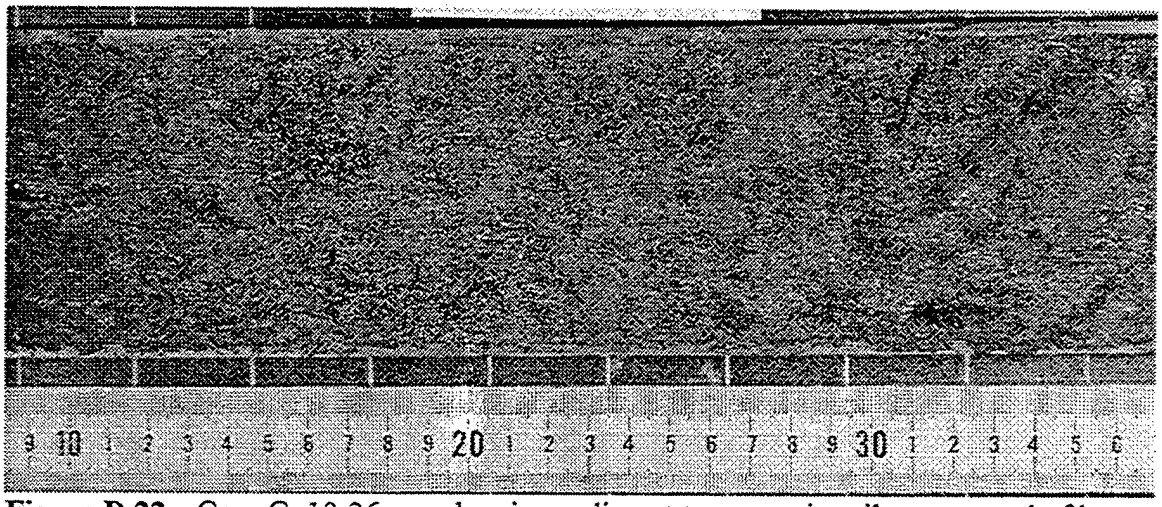

Figure D.22. Core G, 10-36 cm, showing sediment texture primarily composed of heavy concentrations of glauconite sands and foraminifera.

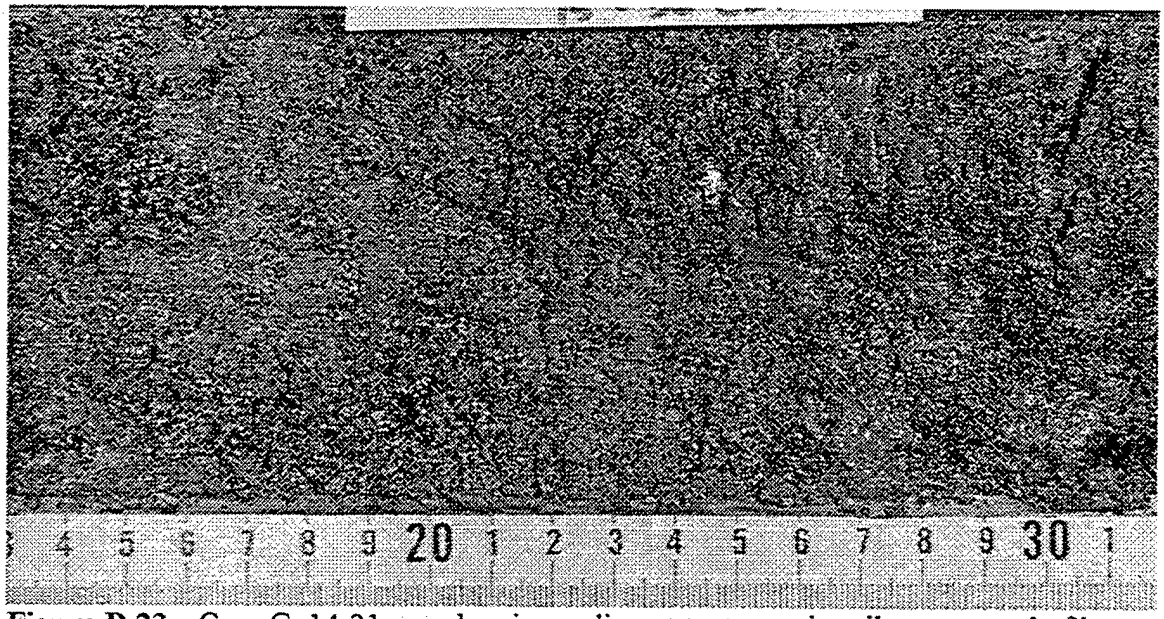

Figure D.23. Core G, 14-31 cm, showing sediment texture primarily composed of heavy concentrations of glauconite sands and foraminifera.

almost entirely of sand/silt-sized glauconite grains. From 4-14 cm the sediment was composed of olive-green fine-grained mud with a conical glauconite concentration extending from 4-7 cm through the middle of the corD. Glauconite concentrations were also found at 11 cm, and from 13-14 cm. The section also contained some evidence of bioturbation and a moderate concentration of foraminifera tests. From 14-26 cm the sediment was composed of olive-green fine-grained mud with a significant amount of glauconite grains and a dense population of foraminifera tests within the matrix, as well as numerous small splotchy glauconite concentrations interspersed within the core. From 26-32 cm the sediment was composed of olive-green fine-grained mud with a significant amount of glauconite grains and a moderate population of foraminifera tests within the matrix, as well as numerous large splotchy glauconite concentrations interspersed within the core. Several pieces of organic material, 1 cm long, 0.5 cm wide (probably wood), were found at 29 cm and 31 cm. From 32-46 cm the sediment is composed of olive-green fine-grained mud with a significant amount of glauconite grains and a moderate population of foraminifera tests within the matrix, as well as numerous small splotchy glauconite concentrations interspersed within the core. Grain-size analysis samples were taken from 0-2 cm, 5-7 cm, 10-12 cm, 15-17 cm, 22-24 cm, 28-30 cm, 36-38 cm, and 42-44 cm. A Carbon-14 sample was taken from 8-10 cm. A sample from 2-4 cm was taken for DDT analysis.

CORE H

Core H had a total length of 160 cm. Figure D.24 shows the sediment in Core H from 0-61 cm. Figure D.25 shows the sediment in Core H from 45-81 cm. Figure D.26 shows the sediment in Core H from 81-140 cm. Figure D.27 shows the sediment in Core

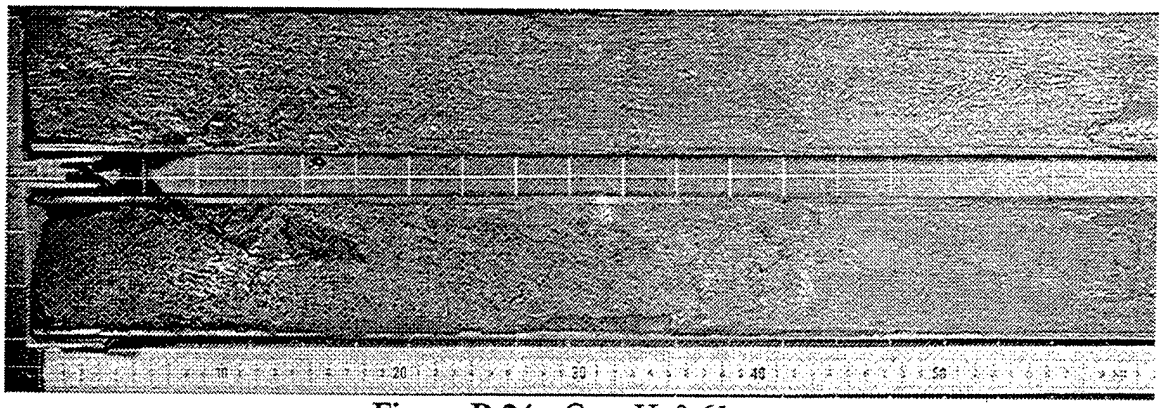

Figure D.24. Core H, 0-61 cm.

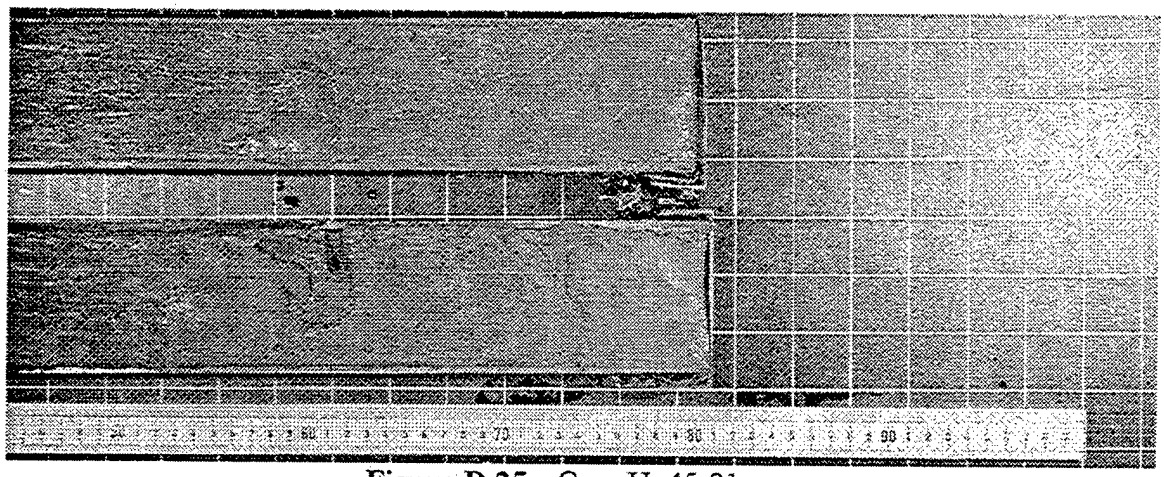

Figure D.25. Core H, 45-81 cm.

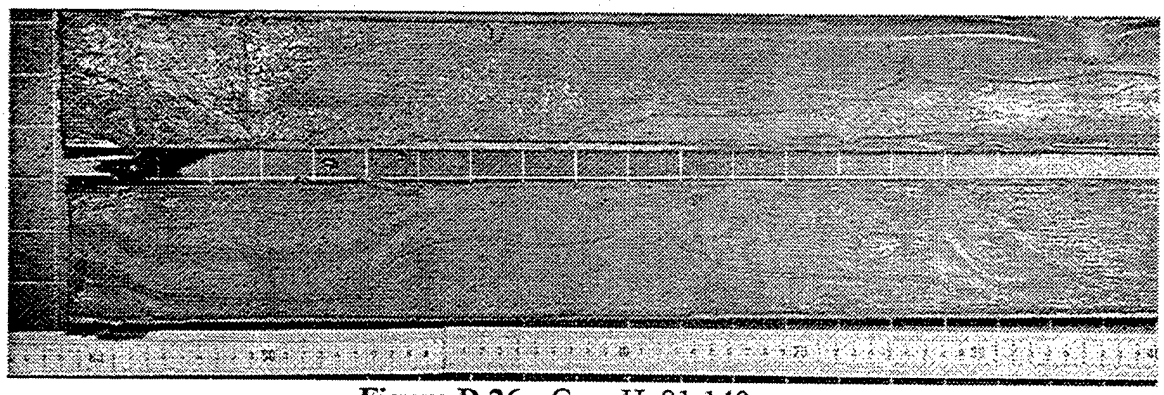

Figure D.26. Core H, 81-140 cm.

H from 130-160 cm. From 0-68 cm the sediment is composed of well-consolidated, homogeneous, olive-green fine-grained mud. From 68-116 cm the sediment is well-consolidated, homogeneous, olive-green fine-grained mud with dark-green lenses occurring from 68-69 cm, 70-71 cm, 73-74 cm, 82-83 cm, 96-98 cm, and 104-106 cm. From 116-125 cm the sediment is composed of well-consolidated, homogeneous, olive-green fine-grained mud, with thin bands of darker mud that indicate possible bioturbation. From 125-134 cm the sediment is well-consolidated, homogeneous, olive-green fine-grained mud. From 134-140 cm, the sediment is well-consolidated, homogeneous, olive-green fine-grained mud with small lenses of dark-green mud interspersed at 135 cm, 137 cm, 138 cm, and 139 cm. The remainder of the core (140-160 cm) is well-consolidated, homogeneous, olive-green fine-grained mud. Grain-size analysis samples were taken from 6-8 cm, 23-25 cm, 33-35 cm, 43-45 cm, 51-53 cm, 64-66 cm, 71-73 cm, 89-91 cm, 101-103 cm, 126-128 cm, 134-136 cm, and 151-153 cm. A sample was taken from 5-7 cm for DDT analysis.

CORE I

Core I had a total length of 45 cm. Figure D.28 shows the sediment in Core I from 0-45 cm. From 0-5 cm the sediment is composed almost entirely of sand/silt-sized glauconite grains. From 5-10 cm, the sediment is composed of mostly sand/silt-sized glauconite grains, with a moderate population of foraminifera tests and some olive-green fine-grained mud matrix. From 10-14 cm, the sediment is composed of well-consolidated olive-green fine-grained mud with a dense population of foraminifera tests and a large glauconite concentration at 12 cm. From 14-29 cm the sediment is composed of well-consolidated dark-green fine-grained mud with numerous large lens-shaped glauconite

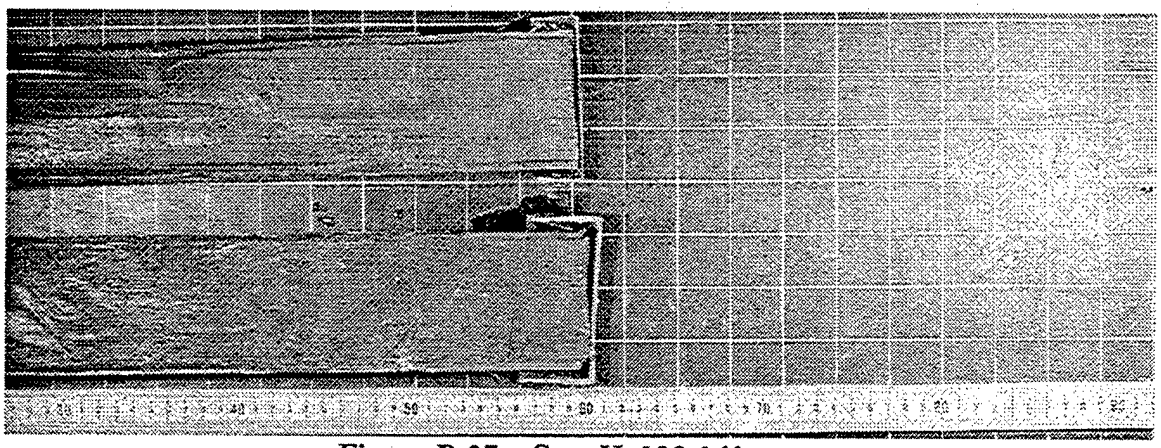

Figure D.27. Core H, 128-160 cm.

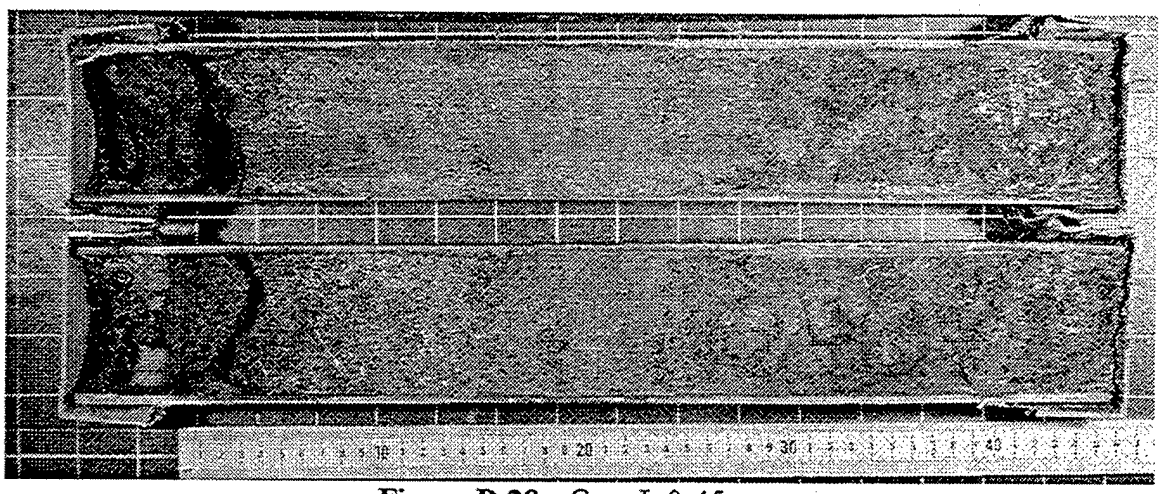

Figure D.28. Core I, 0-45 cm.

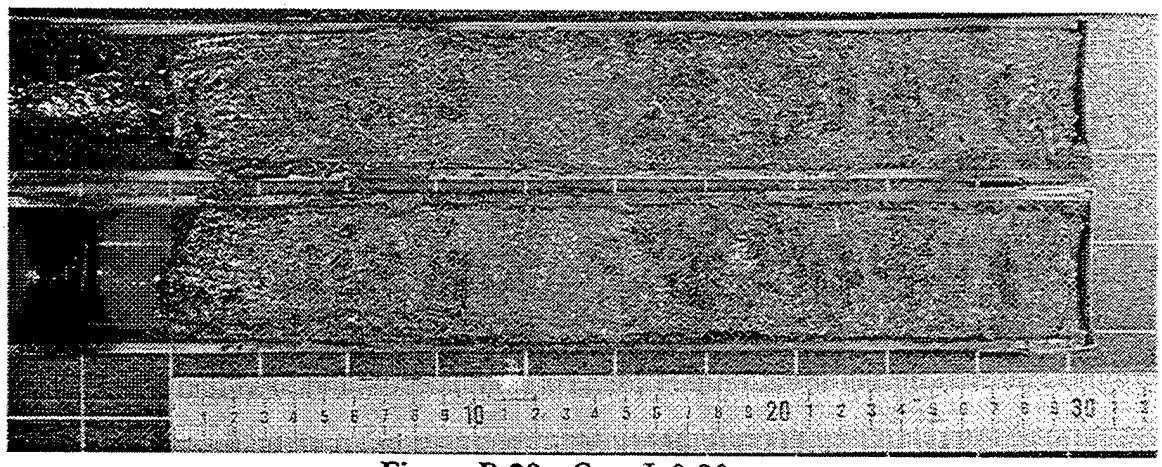

Figure D.29. Core J, 0-30 cm.

concentrations and a moderate population of foraminifera tests. From 29-45 cm the sediment is composed of well-consolidated, dark-green fine-grained mud with large lens-shaped glauconite concentrations interspersed throughout the core. Grain-size analysis samples were taken from 6-8 cm, 10-12 cm, 14-16 cm, 20-22 cm, 24-26 cm, 29-1 cm, 33-35 cm, and 41-43 cm. A sample from 2-5 cm was taken for DDT analysis.

CORE J

Core J had a total length of 30 cm. Figure D.29 shows the sediment in Core J from 0-30 cm. From 0-3 cm, the sediment is composed almost entirely of sand/silt-sized glauconite grains. From 3-10 cm, the sediment is composed of sand/silt-sized grains of glauconite, with a surrounding matrix of olive-green, fine-grained mud. Three distinct patches of concentrated glauconite grains exist from 4-5 cm, 6-7 cm, and 8-10 cm. All are approximately 2 cm in width. From 10-16 cm, the sediment is mostly composed of olive-green, fine-grained mud with a significant amount of glauconite grains within the matrix. From 16-30 cm the sediment is composed of sand/silt-sized grains of glauconite, with a surrounding matrix of olive-green, fine-grained mud. Large patches of concentrated glauconite exist throughout this section of the core, including a large lens-shaped concentration from 27-28 cm. Grain-size analysis samples were taken from 2-5 cm, 5-7 cm, 7-10 cm, 12-14 cm, 16-18 cm, 20-22 cm, 24-26 cm, and 26-28 cm.

CORE K

Core K had a total length of 8 cm. No pictures were taken of Core K. From 0-2 cm the sediment is composed of moderately consolidated, homogeneous, fine-grained dark-green mud with a significant amount of glauconite grains within the matrix. The remainder of the core consists of sand/silt-sized glauconite grains with some dark-green,

fine-grained mud matrix and a relatively sparse population of foraminifera tests. Grain-size analysis samples were taken from 1-3 cm and 4-7 cm.

APPENDIX E - SUBSAMPLING DATA FOR EACH CORE

CORE	DEPTH (cm)	WEIGHT (g)
A	23-25	11.9103
	43-47	15.4890
	73-77	19.6661
	93-97	27.3967
	100-104	23.8448
B	18-22	20.8428
	43-47	20.1072
	78-82	17.4102
	108-112	20.7093
C	10-14	16.6922
	43-47	21.9065
	78-82	24.3134
	123-127	17.1678
D	28-31	18.7080
	58-62	30.5482
	82-86	23.1712
	92-95	18.1748
	98-102	20.5194
	104-106	17.6086
	114-118	28.5890
E	14-16	45.8627
	38-42	29.2851
	48-52	29.9591
	68-72	26.5805
	78-82	32.3437
	108-112	35.6810
	125-127	28.3314
F	10-14	29.5180
	24-28	20.8601
	43-47	31.4982
	63-67	26.8175
	70-74	24.7176
	115-119	41.1152
	133-137	23.4143
	153-157	50.6544
	171-175	45.0653

CORE	DEPTH (cm)	WEIGHT (g)
G	0-2	31.9400
	5-7	32.2790
	10-12	27.5628
	15-17	31.1189
	22-24	31.1570
	28-30	35.1448
	36-38	37.3276
	42-44	33.5786
H	6-8	29.1312
	23-25	20.1840
	33-35	18.0271
	43-45	24.7359
	51-53	17.8062
	64-66	18.6355
	71-73	15.3371
	89-91	15.6565
	101-103	27.0129
	126-128	12.7804
	134-136	19.5408
	151-153	16.4430
I	6-8	35.6941
	10-12	30.4172
	14-16	43.0051
	20-22	31.2914
	24-26	39.0912
	29-31	37.4624
	33-35	33.0894
	41-43	35.7448
J	2-5	18.5150
	5-7	14.3950
	7-10	17.5113
	12-14	15.4115
	16-18	18.4450
	20-22	15.0414
	24-26	17.6943
	26-28	15.7208
K	1-3	9.4008
	4-7	13.0278

APPENDIX F - DRY-SIEVE RESULTS BY WEIGHT (GRAMS)

Sample	MIN 1	0	1	2	3	4	6
A23	0.0000	0.0022	0.0484	0.0446	0.1365	0.3052	0.4691
A43	0.0000	0.0000	0.0061	0.0126	0.0274	0.1578	0.5105
A73	0.0038	0.0027	0.0077	0.0263	0.0528	0.1399	0.3911
A93	0.0000	0.0015	0.0061	0.0994	0.1306	0.4279	0.8238
A100	0.0000	0.0075	0.0258	0.0836	0.1196	0.5502	1.0870
B18	0.0000	0.0033	0.0079	0.0810	0.1535	0.5804	1.3499
B43	0.0000	0.0000	0.0059	0.1399	0.1085	0.5599	1.3503
B78	0.0000	0.0016	0.0041	0.0147	0.0346	0.1101	0.4066
B108	0.0000	0.0017	0.0208	0.0791	0.1344	0.3124	0.6515
C10	0.0000	0.0439	0.0008	0.4616	0.7056	1.1551	1.1915
C43	0.0000	0.0041	0.0100	0.0589	0.1621	0.5664	0.8588
C78	0.0000	0.0000	0.0000	0.0431	0.1861	0.6738	1.0458
C123	0.0000	0.0049	0.0082	0.0259	0.0564	0.3294	0.6639
D28	0.0000	0.0269	0.0605	0.2813	0.5413	1.7151	2.1552
D58	0.0036	0.0039	0.0274	0.5010	1.0093	2.3848	2.5397
D82	0.0000	0.0025	0.0102	0.2084	0.7098	2.8709	2.8999
D92	0.0000	0.0018	0.0036	0.0285	0.1417	1.2642	1.4234
D98	0.0000	0.0055	0.0087	0.1213	0.5809	2.8729	2.4641
D104	0.0000	0.0018	0.0081	0.0635	0.3494	2.6394	2.3462
D114	0.0000	0.0030	0.0111	0.0547	0.2544	3.3176	3.6105
E14	0.0000	0.0055	0.0407	0.9169	2.6684	8.3151	5.7413
E38	0.0000	0.0065	0.0319	0.1550	0.4968	2.8815	3.6922
E48	0.0000	0.0084	0.0215	0.0926	0.2898	2.1470	3.5290
E68	0.0000	0.0000	0.0128	0.0331	0.0944	1.0458	2.4648
E78	0.0000	0.0169	0.0632	0.1347	0.2784	1.9718	3.9203
E108	0.0000	0.0115	0.0803	0.3897	1.1525	5.2753	5.0540
E125	0.0000	0.0141	0.0435	0.3424	1.1471	4.4842	3.7983
F10	0.0000	0.0105	0.0629	0.6662	2.5664	6.6443	3.4190
F24	0.0121	0.0000	0.0168	0.4305	0.9118	2.8958	2.0870
F43	0.0000	0.0000	0.0279	0.9887	1.3279	4.1506	2.8501
F63	0.0000	0.0000	0.0829	0.2151	0.2756	1.2365	1.9072
F70	0.0000	0.0019	0.0827	0.3287	0.4841	1.9336	2.3916
F115	0.0000	0.0022	0.1767	1.5604	3.9770	8.7800	4.2508
F133	0.0000	0.0040	0.1252	0.1827	0.3996	2.2628	2.3865
F153	0.0000	0.0037	0.4163	1.7449	6.0086	13.5943	5.1875
F171	0.0000	0.0087	0.3324	1.6458	3.7901	9.6006	5.2718

Sample	MIN 1	0	1	2	3	4	6
G0	0.0838	0.1312	1.0117	9.9698	8.3909	6.0198	0.8191
G5	0.0365	0.0277	0.6355	7.4011	6.6855	6.0700	1.5412
G10	0.0020	0.0178	0.5579	5.9843	5.1853	4.6975	1.4478
G15	0.0167	0.0235	3.6677	10.4143	5.3103	2.2849	0.9971
G22	0.0038	0.0302	3.2150	11.0346	5.4233	3.0040	0.8567
G28	0.3817	0.2200	3.1647	12.7853	6.3824	3.3489	0.9696
G36	0.0000	0.0567	2.5447	12.7636	5.8653	3.8983	1.2305
G42	0.0087	0.0451	2.2347	12.5474	5.6280	3.2810	1.0365
H6	0.0000	0.0127	0.0835	0.0955	0.4231	7.1613	5.5480
H23	0.0000	0.0065	0.0265	0.0453	0.2402	5.4447	4.3344
H33	0.0000	0.0000	0.0171	0.0708	0.2359	4.3289	3.5502
H43	0.0000	0.0000	0.0417	0.0819	0.4157	5.7726	5.5780
H51	0.0000	0.0008	0.0023	0.0406	0.1820	2.8094	3.1013
H64	0.0000	0.0068	0.0051	0.0176	0.1148	1.5209	2.2904
H71	0.0000	0.0000	0.0036	0.0203	0.1854	1.5714	1.6284
H89	0.0604	0.0086	0.0104	0.0365	0.1368	0.6347	0.8349
H101	0.0000	0.0000	0.0029	0.0301	0.7751	5.8076	5.1423
H126	0.0000	0.0000	0.0037	0.0248	0.1317	0.4335	0.5654
H134	0.0000	0.0000	0.0000	0.0202	0.1893	0.8104	1.1907
H151	0.0000	0.0000	0.0034	0.0521	0.2363	0.7189	0.7218
I6	0.0305	0.0451	3.2889	12.9935	9.3535	3.5898	0.9428
I10	0.0303	0.0749	3.4588	8.7321	6.6215	3.1124	1.0668
I14	0.0043	0.0559	5.1397	11.9295	8.7868	4.0993	1.7640
I20	0.0071	0.0603	2.5394	8.9403	6.7237	2.7763	1.1704
I24	0.0000	0.0542	4.1075	11.8541	8.1809	3.3232	1.4083
I29	0.0000	0.0125	3.0157	9.7916	7.7708	3.0386	1.3452
I33	0.0000	0.0085	2.5332	9.3464	7.1870	3.2108	1.2464
I41	0.0000	0.0204	2.6435	10.5798	7.8616	3.8971	1.2991
J2	0.0009	0.0000	1.3123	6.3256	3.0272	1.8152	0.7921
J5	0.0000	0.0028	0.8224	4.4945	2.1553	1.4967	0.6943
J7	0.0000	0.0157	1.0912	5.4516	2.6995	1.9585	0.8563
J12	0.0000	0.0022	0.6306	4.1345	2.1849	1.6584	0.8852
J16	0.0015	0.0066	1.2433	7.1794	3.0946	1.6646	0.7403
J20	0.0143	0.0258	0.9371	5.7100	2.6208	1.5049	0.6220
J24	0.0000	0.0180	0.9629	6.6387	3.0018	1.8415	0.6957
J26	0.0000	0.0173	0.5241	5.2153	2.5453	1.6699	0.7635
K1	0.0000	0.0018	0.0254	0.5654	2.6396	1.7900	0.4387
K4	0.4281	0.8188	2.0608	6.5692	1.8777	0.3538	0.0916

DRY-SIEVE RESULTS BY PERCENT

Sample	MIN 1	0	1	2	3	4	6
A23	0.0000	0.0185	0.4064	0.3745	1.1461	2.5625	3.9386
A43	0.0000	0.0000	0.0394	0.0813	0.1769	1.0188	3.2959
A73	0.0204	0.0145	0.0413	0.1409	0.2829	0.7495	2.0952
A93	0.0000	0.0055	0.0223	0.3628	0.4767	1.5619	3.0069
A100	0.0000	0.0315	0.1082	0.3506	0.5016	2.3074	4.5586
B18	0.0000	0.0158	0.0379	0.3886	0.7365	2.7847	6.4766
B43	0.0000	0.0000	0.0293	0.6958	0.5396	2.7846	6.7155
B78	0.0000	0.0092	0.0235	0.0844	0.1987	0.6324	2.3354
B108	0.0000	0.0082	0.1004	0.3820	0.6490	1.5085	3.1459
C10	0.0000	0.2630	0.0048	2.7654	4.2271	6.9200	7.1381
C43	0.0000	0.0187	0.0456	0.2689	0.7400	2.5855	3.9203
C78	0.0000	0.0000	0.0000	0.1773	0.7654	2.7713	4.3013
C123	0.0000	0.0285	0.0478	0.1509	0.3285	1.9187	3.8671
D28	0.0000	0.1438	0.3234	1.5036	2.8934	9.1677	11.5202
D58	0.0118	0.0128	0.0897	1.6400	3.3040	7.8067	8.3137
D82	0.0000	0.0108	0.0440	0.8994	3.0633	12.3899	12.5151
D92	0.0000	0.0099	0.0198	0.1568	0.7797	6.9558	7.8317
D98	0.0000	0.0268	0.0424	0.5911	2.8310	14.0009	12.0086
D104	0.0000	0.0102	0.0460	0.3606	1.9843	14.9893	13.3242
D114	0.0000	0.0105	0.0388	0.1913	0.8899	11.6045	12.6290
E14	0.0000	0.0120	0.0887	1.9992	5.8182	18.1304	12.5185
E38	0.0000	0.0222	0.1089	0.5293	1.6964	9.8395	12.6078
E48	0.0000	0.0280	0.0718	0.3091	0.9673	7.1664	11.7794
E68	0.0000	0.0000	0.0482	0.1245	0.3551	3.9345	9.2730
E78	0.0000	0.0523	0.1954	0.4165	0.8608	6.0964	12.1208
E108	0.0000	0.0322	0.2250	1.0922	3.2300	14.7846	14.1644
E125	0.0000	0.0498	0.1535	1.2086	4.0489	15.8277	13.4067
F10	0.0000	0.0356	0.2131	2.2569	8.6944	22.5093	11.5828
F24	0.0580	0.0000	0.0805	2.0637	4.3710	13.8820	10.0047
F43	0.0000	0.0000	0.0886	3.1389	4.2158	13.1773	9.0485
F63	0.0000	0.0000	0.3091	0.8021	1.0277	4.6108	7.1118
F70	0.0000	0.0077	0.3346	1.3298	1.9585	7.8228	9.6757
F115	0.0000	0.0054	0.4298	3.7952	9.6728	21.3546	10.3388
F133	0.0000	0.0171	0.5347	0.7803	1.7066	9.6642	10.1925
F153	0.0000	0.0073	0.8218	3.4447	11.8620	26.8374	10.2410
F171	0.0000	0.0193	0.7376	3.6520	8.4102	21.3038	11.6981

Sample	MIN 1	0	1	2	3	4	6
G0	0.2624	0.4108	3.1675	31.2142	26.2708	18.8472	2.5645
G5	0.1131	0.0858	1.9688	22.9285	20.7116	18.8048	4.7746
G10	0.0073	0.0646	2.0241	21.7115	18.8127	17.0429	5.2527
G15	0.0537	0.0755	11.7861	33.4662	17.0645	7.3425	3.2042
G22	0.0122	0.0969	10.3187	35.4161	17.4064	9.6415	2.7496
G28	1.0861	0.6260	9.0047	36.3789	18.1603	9.5289	2.7589
G36	0.0000	0.1519	6.8172	34.1935	15.7130	10.4435	3.2965
G42	0.0259	0.1343	6.6551	37.3673	16.7607	9.7711	3.0868
H6	0.0000	0.0436	0.2866	0.3278	1.4524	24.5829	19.0449
H23	0.0000	0.0322	0.1313	0.2244	1.1901	26.9753	21.4744
H33	0.0000	0.0000	0.0949	0.3927	1.3086	24.0133	19.6937
H43	0.0000	0.0000	0.1686	0.3311	1.6806	23.3369	22.5502
H51	0.0000	0.0047	0.0135	0.2379	1.0664	16.4610	18.1713
H64	0.0000	0.0365	0.0274	0.0946	0.6168	8.1712	12.3054
H71	0.0000	0.0000	0.0235	0.1324	1.2088	10.2457	10.6174
H89	0.3858	0.0549	0.0664	0.2331	0.8738	4.0539	5.3326
H101	0.0000	0.0000	0.0107	0.1114	2.8694	21.4994	19.0365
H126	0.0000	0.0000	0.0290	0.1940	1.0305	3.3919	4.4240
H134	0.0000	0.0000	0.0000	0.1034	0.9687	4.1472	6.0934
H151	0.0000	0.0000	0.0207	0.3169	1.4371	4.3721	4.3897
I6	0.0854	0.1264	9.2141	36.4024	26.2046	10.0571	2.6413
I10	0.0996	0.2462	11.3712	28.7078	21.7689	10.2324	3.5072
I14	0.0100	0.1300	11.9514	27.7397	20.4320	9.5321	4.1018
I20	0.0227	0.1927	8.1153	28.5711	21.4874	8.8724	3.7403
I24	0.0000	0.1387	10.5075	30.3242	20.9277	8.5011	3.6026
I29	0.0000	0.0334	8.0499	26.1371	20.7429	8.1111	3.5908
I33	0.0000	0.0257	7.6556	28.2459	21.7199	9.7034	3.7668
I41	0.0000	0.0571	7.3955	29.5982	21.9937	10.9026	3.6344
J2	0.0049	0.0000	7.0878	34.1647	16.3500	9.8039	4.2782
J5	0.0000	0.0195	5.7133	31.2237	14.9731	10.3977	4.8234
J7	0.0000	0.0897	6.2314	31.1319	15.4158	11.1842	4.8900
J12	0.0000	0.0143	4.0917	26.8274	14.1771	10.7608	5.7438
J16	0.0081	0.0358	6.7406	38.9233	16.7774	9.0247	4.0136
J20	0.0951	0.1715	6.2301	37.9619	17.4239	10.0051	4.1353
J24	0.0000	0.1017	5.4419	37.5189	16.9648	10.4073	3.9318
J26	0.0000	0.1100	3.3338	33.1745	16.1907	10.6222	4.8566
K1	0.0000	0.0191	0.2702	6.0144	28.0785	19.0409	4.6666
K4	3.2860	6.2850	15.8185	50.4245	14.4130	2.7157	0.7031

APPENDIX G - PIPETTE RESULTS BY WEIGHT (GRAMS)

Sample	7	8	9	10	>10
A23	4.7847	1.8485	1.3124	0.8477*	2.1549
A43	7.5772	1.3601	1.1419	1.0912	2.8928
A73	5.8946	1.5130	1.4521	1.2084	3.2087
A93	13.0683	1.2009	1.1705	1.5303	3.2633
A100	11.1430	1.8777	2.6575	1.4057	1.9649
B18	9.5803	1.7625	1.0513	1.0668	3.3188
B43	7.2264	1.5560	0.9137	0.8720	2.3288
B78	8.8950	1.5870	1.1826	1.1826	3.4620
B108	8.9930	1.4675	0.8379	1.3812	3.4073
C10	8.6289	1.0469	0.6685	0.4042	1.6636
C43	12.5452	1.6341	1.6544	1.5123	3.2226
C78	11.6424	1.6375	2.7720	0.7443	1.4117
C123	6.2146	1.6424	1.6576	1.2064	2.8944
D28	8.5581	1.0226	0.9953	1.2687	2.4225
D58	9.8440	2.0166	3.9694	2.3031	2.8656
D82	8.3140	1.6468	1.5398	2.0959	3.1812
D92	6.4362	1.3306	1.3718	1.5317	3.3470
D98	8.0071	1.3983	1.2282	1.6961	3.0465
D104	6.3121	1.2153	1.0529	1.1681	2.6296
D114	13.2342	1.9794	1.8593	2.1570	2.5695
E14	13.3851	3.3773	2.3777	2.7073	4.4851
E38	13.1938	3.0688	4.1466	0.5734	1.4229
E48	16.8031	4.2678	2.1125	0.3056	1.0401
E68	14.6368	2.4324	4.2168	1.0038	1.4711
E78	11.7609	2.8588	5.3755	1.5508	2.2573
E108	11.2248	1.4687	5.7872	3.1122	2.9140
E125	9.0834	1.7662	1.8375	2.0021	4.1906
F10	8.2666	1.7180	1.7124	1.5730	3.1850
F24	6.6582	1.8375	1.6632	1.5048	3.0889
F43	9.3777	2.4341	3.4828	2.2961	2.3844
F63	10.3585	1.7429	2.2597	3.4473	4.2171
F70	9.0790	1.3360	1.7368	2.7533	3.8279
F115	10.5783	2.2703	4.1208	2.9995	2.9553
F133	7.7574	1.3939	1.6253	2.1928	4.8153
F153	10.4812	2.4969	6.8891	1.7308	2.2075
F171	15.1410	3.8551	4.2709	0.3980	1.5860

Sample	7	8	9	10	>10
G0	1.9131	0.8325	0.7652	0.5377	1.0445
G5	4.1529	3.4944	1.3791	0.1348	0.6533
G10	3.9474	1.3245	2.0963	0.7353	1.1316
G15	4.3327	2.6719	0.5658	0.1677	0.5763
G22	3.3568	0.9422	1.1842	0.7671	1.0812
G28	3.5198	1.0601	0.8799	0.5506	1.0549
G36	3.7848	2.2957	1.7993	0.4136	0.5222
G42	4.0951	1.3226	1.8822	0.7275	0.7325
H6	7.2974	1.7769	1.3706	1.2406	2.7142
H23	5.0477	1.1145	0.8007	0.7466	1.7799
H33	5.4093	0.9241	0.8970	0.5782	1.9670
H43	6.9428	0.6444	0.8882	0.9346	2.4149
H51	5.1004	0.8165	0.8112	1.0551	2.2533
H64	5.8587	1.5010	1.2051	1.6409	3.3033
H71	7.6468	0.6126	0.9448	1.3446	2.3672
H89	6.3047	1.1486	1.5162	1.4651	2.7975
H101	8.1774	1.1049	1.2864	1.4145	3.1866
H126	4.7399	0.8479	1.2871	1.2871	2.6304
H134	6.7539	0.9701	1.6481	2.0757	3.5673
H151	5.6069	1.2255	1.6647	1.7260	2.8749
I6	3.1337	0.6993	0.6730	0.4890	1.1357
I10	4.6332	1.9296	0.2876	0.3399	0.8158
I14	6.4859	3.3136	1.1359	0.0785	0.8166
I20	4.3525	1.5902	2.0343	0.6970	1.0636
I24	5.1833	3.6153	1.5003	0.0781	0.9168
I29	5.8992	5.8421	1.4735	0.1401	0.7108
I33	4.5179	1.9779	2.3631	0.3071	0.7599
I41	4.1559	0.9160	0.9526	1.1881	2.4338
J2	3.2237	0.6353	0.5670	0.4463	0.9713
J5	2.9236	0.4573	0.4727	0.5498	0.8273
J7	3.8897	0.5491	0.4157	0.5439	0.9545
J12	3.5474	0.3982	0.6050	0.7136	0.9773
J16	2.1489	0.5716	0.3546	0.8045	0.9315
J20	2.0959	0.2435	0.4552	0.4287	0.6722
J24	2.4745	0.4763	0.4970	0.5591	1.0198
J26	2.3605	0.5591	0.3468	0.9059	1.0923
K1	1.6229	0.4173	0.6389	1.2262	0.0000
K4	0.2669	0.1832	0.2408	0.3507	0.0000

PIPETTE RESULTS BY PERCENT

Sample	7	8	9	10	>10
A23	40.1731	15.5204	11.0186	7.1171	18.0929
A43	48.9197	8.7813	7.3724	7.0447	18.6767
A73	31.5789	8.1055	7.7791	6.4735	17.1902
A93	47.7002	4.3835	4.2725	5.5857	11.9112
A100	46.7314	7.8746	11.1450	5.8952	8.2404
B18	45.9646	8.4561	5.0440	5.1182	15.9232
B43	35.9396	7.7384	4.5444	4.3366	11.5817
B78	51.0908	9.1151	6.7928	6.7928	19.8848
B108	43.4251	7.0863	4.0458	6.6695	16.4530
C10	51.6940	6.2716	4.0051	2.4217	9.9662
C43	57.2672	7.4596	7.5522	6.9036	14.7106
C78	47.8849	6.7351	11.4012	3.0614	5.8061
C123	36.1993	9.5665	9.6551	7.0273	16.8595
D28	45.7458	5.4661	5.3200	6.7815	12.9491
D58	32.2245	6.6013	12.9940	7.5393	9.3807
D82	35.8807	7.1069	6.6454	9.0452	13.7293
D92	35.4128	7.3209	7.5479	8.4276	18.4158
D98	39.0221	6.8146	5.9855	8.2656	14.8471
D104	35.8467	6.9016	5.9794	6.6339	14.9336
D114	46.2911	6.9236	6.5034	7.5447	8.9879
E14	29.1852	7.3640	5.1843	5.9030	9.7794
E38	45.0528	10.4791	14.1595	1.9580	4.8588
E48	56.0868	14.2454	7.0511	1.0201	3.4719
E68	55.0659	9.1510	15.8644	3.7763	5.5346
E78	36.3623	8.8389	16.6198	4.7948	6.9790
E108	31.4586	4.1161	16.2193	8.7222	8.1668
E125	32.0611	6.2341	6.4858	7.0666	14.7915
F10	28.0053	5.8203	5.8014	5.3289	10.7902
F24	31.9184	8.8086	7.9733	7.2139	14.8075
F43	29.7721	7.7278	11.0572	7.2897	7.5701
F63	38.6260	6.4992	8.4264	12.8548	15.7251
F70	36.7310	5.4051	7.0266	11.1391	15.4867
F115	25.7284	5.5219	10.0226	7.2953	7.1878
F133	33.1310	5.9532	6.9415	9.3652	20.5657
F153	20.6916	4.9292	13.6002	3.4169	4.3579
F171	33.5980	8.5544	9.4770	0.8831	3.5193

Sample	7	8	9	10	>10
G0	5.9897	2.6063	2.3959	1.6836	3.2700
G5	12.8656	10.8257	4.2725	0.4176	2.0238
G10	14.3216	4.8054	7.6054	2.6676	4.1054
G15	13.9231	8.5862	1.8182	0.5387	1.8519
G22	10.7739	3.0240	3.8006	2.4621	3.4701
G28	10.0151	3.0162	2.5038	1.5667	3.0016
G36	10.1394	6.1501	4.8204	1.1081	1.3990
G42	12.1956	3.9390	5.6054	2.1664	2.1816
H6	25.0500	6.0998	4.7050	4.2587	9.3170
H23	25.0083	5.5217	3.9670	3.6990	8.8186
H33	30.0063	5.1260	4.9761	3.2075	10.9114
H43	28.0677	2.6049	3.5906	3.7783	9.7627
H51	29.8847	4.7840	4.7530	6.1820	13.2027
H64	31.4764	8.0642	6.4745	8.8157	17.7470
H71	49.8583	3.9941	6.1604	8.7667	15.4347
H89	40.2689	7.3364	9.6841	9.3580	17.8683
H101	30.2724	4.0903	4.7622	5.2364	11.7967
H126	37.0870	6.6341	10.0710	10.0710	20.5817
H134	34.5632	4.9643	8.4340	10.6225	18.2558
H151	34.0988	7.4533	10.1240	10.4967	17.4842
I6	8.7793	1.9591	1.8855	1.3699	3.1818
I10	15.2323	6.3439	0.9456	1.1175	2.6820
I14	15.0817	7.7052	2.6414	0.1826	1.8989
I20	13.9095	5.0820	6.5010	2.2275	3.3990
I24	13.2595	9.2484	3.8379	0.1999	2.3454
I29	15.7470	15.5946	3.9333	0.3739	1.8974
I33	13.6537	5.9774	7.1414	0.9281	2.2966
I41	11.6265	2.5625	2.6650	3.3239	6.8089
J2	17.4113	3.4312	3.0626	2.4104	5.2461
J5	20.3108	3.1769	3.2840	3.8194	5.7470
J7	22.2124	3.1355	2.3736	3.1062	5.4505
J12	23.0176	2.5836	3.9258	4.6304	6.3416
J16	11.6501	3.0990	1.9225	4.3616	5.0503
J20	13.9342	1.6186	3.0261	2.8502	4.4688
J24	13.9846	2.6916	2.8086	3.1597	5.7635
J26	15.0153	3.5563	2.2062	5.7625	6.9479
K1	17.2636	4.4392	6.7958	13.0436	0.0000
K4	2.0490	1.4062	1.8481	2.6919	0.0000

LIST OF REFERENCES

Atwater, T., 1970, Implications of plate tectonics for the Cenozoic tectonic evolution of western North America: Geological Society of America Bulletin, v.81, p.3513-3536.

Boggs, S. Jr., 1987, Principles of Sedimentology and Stratigraphy, MacMillan Publishing Company.

Clark, D.G., Slemmons, D.B, and Caskey, S.J., 1994, Seismotectonic framework of coastal central California, in, Seismotectonics of the central coast ranges, Special Paper-Geological Society of America, v.292, p. 9-30.

Collins, C.A., Garfield, N., Rago, T.A., Rischmiller, F.W., and Carter, E., 1997, Mean structure of the inshore countercurrent and California undercurrent off Point Sur, California, Deep-Sea Research II, vol. 47, p. 765-782.

Deer, W.A., Howie, R.A., and Zussman, J., 1992, The Rock-Forming Minerals, Longman Scientific and Technical.

Folk, R.L., 1980, Petrology of Sedimentary Rocks, Hemphill Publishing Company.

Greene, H.G., 1977, Geology of the Monterey Bay Region: U.S. Geological Survey Open-File Report 77-718, 347 p., 9 plates.

Greene, H.G., Stubblefield, W.L., and Theberge, A.E. Jr, 1989, Geology of the Monterey Submarine Canyon System and Adjacent Areas, Offshore Central California, Results of NOAA SeaBeam Survey: U.S.Geological Survey Open-File Report 89-221, 33 p., 4 map sheets.

Greene, H.G., Maher, N.M., Paull, C.K., 2001, Physiography of the Monterey Bay National Marine Sanctuary and implications about continental margin development, Marine Geology, in press.

Hamilton, E.L., 1970a, Sound Velocity and Related Properties of Marine Sediment, North Pacific, Journal of Geophysical Research, vol. 75, p. 4423-4446.

-----, 1970b, Sound Channels in Surficial Marine Sediment, Journal of the Acoustical Society of America, vol. 48, p. 1296-1298.

-----, 1970c, Reflection Coefficients and Bottom Losses at Normal Incidence Computed from Pacific Sediment Properties, Geophysics, vol. 35, p. 995-1004.

-----, 1971, Prediction of *In-situ* Acoustic and Elastic Properties of Marine Sediment, Geophysics, vol. 36, p. 266-284.

-----, 1972, Compressional-wave Attenuation in Marine Sediment, Geophysics, vol. 37, p. 620-646.

-----, 1974, Prediction of Deep-sea Sediment Properties: State-of-the-art, Deep-Sea Sediment, Plenum Press.

-----, 1976, Variations of Density and Porosity with Depth in Deep-sea Sediment, Journal of Sedimentary Petrology, vol. 46, p. 280-300.

-----, 1978, Sound velocity-density Relations in Sea-floor sediment and Rocks, Journal of the Acoustic Society of America, vol. 63, p. 366-377.

Hamilton, E.L., and Bachman, R.T., 1982, Sound velocity and related properties of marine sediment, Journal of the Acoustic Society of America, vol. 72, p. 1891-1904.

Kayen, R.E., Edwards, B.D., Lee, H.J., 1999, Nondestructive Laboratory Measurement of Geotechnical and Geoacoustic Properties Through Intact Core-liner, in Nondestructive and Automated Testing for Soil and Rock Properties ASTM STP 1350, W.A. Marr and C.E. Fairhurst, Eds., American Society for Testing and Materials, West Conshohocken, PA, 1999.

Lim, D.I., Park, Y.A., Choi, J.Y., Cho, J.W., Khim, B.K., 2000, Glauconite Grains in Continental Shelf Sediment Around the Korean Peninsula and Their Depositional Implications, Geo-Marine Letters, vol. 20, p. 80-86.

Onofre, J., Analysis and Modeling of the Acoustic Tomography Signal Transmission from Davidson Seamount to Sur Ridge: The Forward Problem, Master's Thesis, Naval Postgraduate School, 1999.

Vercoutere, T.L., Mullins, H.T., McDougall, K., Thopmson, J.B., 1987, Sedimentation Across the Central California Oxygen Minimum Zone: An Alternative Coastal Upwelling Sequence, Journal of Sedimentary Petrology, vol. 57, no. 4, p. 709-722.

THIS PAGE INTENTIONALLY LEFT BLANK

INITIAL DISTRIBUTION LIST

1. Defense Technical Information Center 2
   8725 John J. Kingman Road, Suite 0944
   Ft. Belvoir, VA 22060-6218

2. Dudley Knox Library 2
   Naval Postgraduate School
   411 Dyer Road
   Monterey, CA 93943-5101

3. Maury Oceanographic Library 1
   1002 Balch Boulevard, Building 1003
   Stennis Space Center, MS 39522-5001

4. The MLML/MBARI Research Library 1
   8272 Moss Landing Road
   Moss Landing, CA 95039

5. Dr. Roland W. Garwood Jr., OC/Co 1
   Oceanography Department
   Naval Postgraduate School
   883 Dyer Road, RM 324
   Monterey, CA 93943-5122

6. Dr. Curtis A. Collins, OC/Co 1
   Oceanography Department
   Naval Postgraduate School
   883 Dyer Road, RM 324
   Monterey, CA 93943-5122

7. Dr. H. Gary Greene 1
   Moss Landing Marine Laboratories
   8272 Moss Landing Road
   Moss Landing, CA 95039

8. Dr. Ching-Sang Chiu, OC/Ci 1
   Oceanography Department
   Naval Postgraduate School
   883 Dyer Road, RM 324
   Monterey, CA 93943-5122

9. Dr. Charles K. Paull 1
Monterey Bay Aquarium Research Institute
7700 Sandholdt Road, P.O. Box 628
Moss Landing, CA 95039-0628

10. Dr. Homa Lee 1
U.S. Geological Survey Mail stop # 999
345 Middlefield Road
Menlo Park, CA 94025

11. Dr. Larry E. Davis 1
15 Fairfield Lane
St. Cloud, MN 56303

12. A. Lyndon and Carol Gabriel 1
12300 SE 13th St.
Vancouver, WA 98683

13. LT Christopher L. Gabriel, USN 1
PSC 819, Box 31
FPO, AE 09645-3200